Evidence for a Possible Supervolcano on Mars at Siloe Patera

by

Cheryl Wilkes Coker

A thesis submitted to the Graduate Faculty of
Auburn University
in partial fulfillment of the
requirements for the Degree of
Master of Science

Auburn, Alabama
May 4, 2014

Approved by

Shawn P. Wright, Co-Chair, Postdoctoral Fellow in Geology
David T. King Jr., Co-Chair, Professor of Geology
Luke J. Marzen, Professor of Geography
Clinton I. Barineau, Professor of Geology (Columbus State University)

Abstract

Highlands on Mars interpreted as impact craters may instead be supervolcanoes within an ancient volcanic province in Arabia Terra, Mars. These volcanoes are characterized by lower than normal topographic relief, collapse features, layered deposits, as well as effusive volcanism and explosive eruptions. Seven features are to be considered part of the new volcanic field, which includes Siloe Patera. Although an alternative hypothesis for Siloe Patera's origin is nested impact craters, evidence points more towards multiple caldera collapses or a combination of impact and caldera collapse events. Regions of interest in and around Siloe Patera include: (1) possible volcanic-doming along the bench; (2) possible ring faulting on the eastern portion of the bench; (3) a spire located on the floor of Siloe Patera; and (4) flow features around Siloe Patera. Data from various Martian orbiters was used to analyze Siloe Patera, Ascraues Mons, a nested crater and three random craters roughly the size of Siloe Patera. Data collection included gathering raw Mars Orbital Laser Altimeter (MOLA) tracks over Siloe Patera, Thermal Emission Imaging System (THEMIS) Night Infrared, Context Camera (CTX), and Mars Orbiter Camera (MOC) images. Utilizing data currently available, characteristics of Siloe Patera resemble that of a volcano more than that of an impact crater based on topographic profiles, depth diameter ratios, slope angles, and comparison of regions of interest.

Acknowledgments

I would like to express a special appreciation and thanks to my advisors, Dr. Shawn Wright and Dr. David King, you have been tremendous mentors for me. I would like to thank you for encouraging my research and for allowing me to grow as a research scientist. I would also like to thank my thesis committee members, Dr. Luke Marzen, and Dr. Clinton Barineau for serving as my committee members even at hardship. I also want to thank Dr. Jacob Bleacher and Dr. Joseph Michalski for allowing me the opportunity to work with you on your exciting finding. It has been an exhilarating challenge that would not have been possible without your generosity.

I want to acknowledge the extensive use of multiple publicly accessible imagery databases which includes Arizona State University <http://themis.asu.edu/>, U.S.G.S Planetary GIS Web Server <http://webgis.wr.usgs.gov/>, MOLA Pedr Query < http://ode.rsl.wustl.edu/mars/dataPointSearch.aspx >, HiWish: Public suggestion Page <http://www.uahirise.org/hiwish/>, Google Earth 7.1, and JMARS.

I would like to dedicate this thesis to my wonderful family and husband for their overwhelming support and advice to always go after your dream. I would also like to give a special thanks to my husband Zachary for his unconditional support, love, and especially patience over the past two years.

Table of Contents

List of Tables

List of Figures

CHAPTER 1

Recent work by Michalski and Bleacher (2013) suggest a possible volcanic field located in northern Arabia Terra, Mars, along the Martian global dichotomy boundary (Figure 1). The field contains seven possible volcanic calderas and associated features that have been named Eden Patera, Euphrates Patera, Semeykin Crater, Ismenia Patera, Oxus Patera, Oxus cavus, and Siloe Patera (Michalski and Bleacher, 2013; Figure 1). A volcanic field associated with Siloe Patera is discussed here. These features are proposed as volcanic in origin due to the presence of complex collapse features, faulting, ridged plains likely to be volcanic in nature, and friable layered deposits, as well as a significant lack of central peaks, uplifted rim, and ejecta typical of impact craters. These supervolcanoes are defined as "plains style caldera complexes" and are characterized by lower than normal topographic relief, collapse features, and friable and layered deposits (Michalski and Bleacher, 2013). Friable layered deposits and fretted terrain are characterized by broad flat-floored, steep-walled valleys that are located along the dichotomy boundary (Carr, 2001). Many fretted terrain regions are thought to form from windblown volcanic ash or eolian sedimentary deposits of sand due to their morphology and erosional characteristics (Irwin and Watters, 2004; Hynek et al., 2003; Michalski and Bleacher, 2013). Sulfates have been detected in a nearby region known as fretted terrain (Gendrin et al., 2005) and ash deposition is interpreted to be one possible reason for the texture of the fretted terrain(Kerber et al., 2012). The sulfates

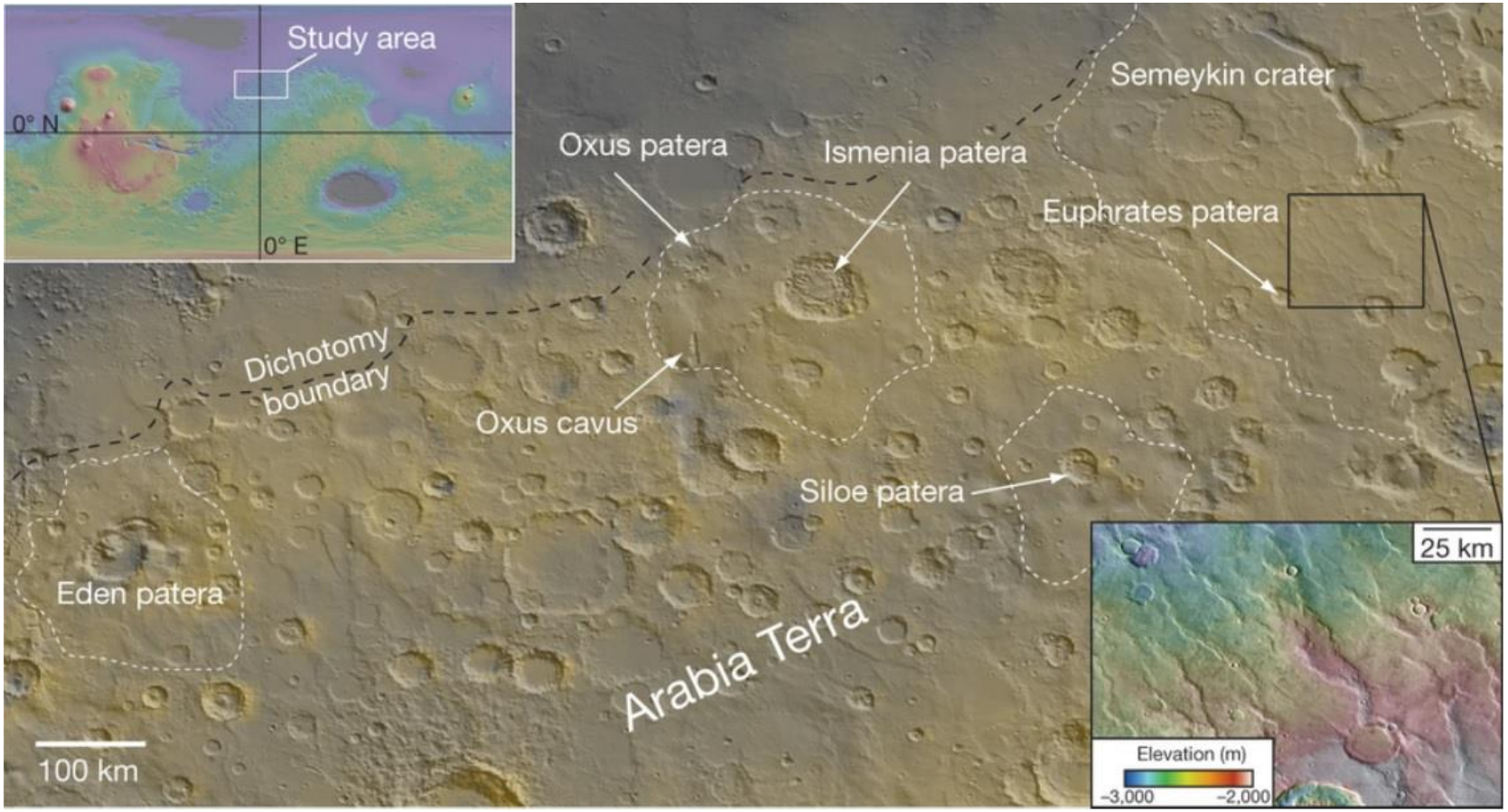
Study area
0° N
0° E
Semeykin crater
Oxus patera
Ismenia patera
Euphrates patera
Dichotomy boundary
Oxus cavus
Siloe patera
Eden patera
Arabia Terra
100 km
25 km
Elevation (m)
−3,000
−2,000

Figure 1: Im

likely formed in a volcanic outgassing environment where materials were altered under water-limited, acidic conditions (Michalski and Bleacher, 2013).

The type volcano for this new category is Eden Patera (Figure 2), which contains evidence for complex and irregularly shaped collapse events with arcuate scarps lining the depressions (Michalski and Bleacher, 2013). Eden Patera has a depth of ~ 700 m and displays many features interpreted as former lava lakes, vents, and cracks related to lava lake drainage. Euphrates Patera also displays irregularly shaped depressions with a similar depth of 700 m (Michalski and Bleacher, 2013). Eden Patera is interpreted to be

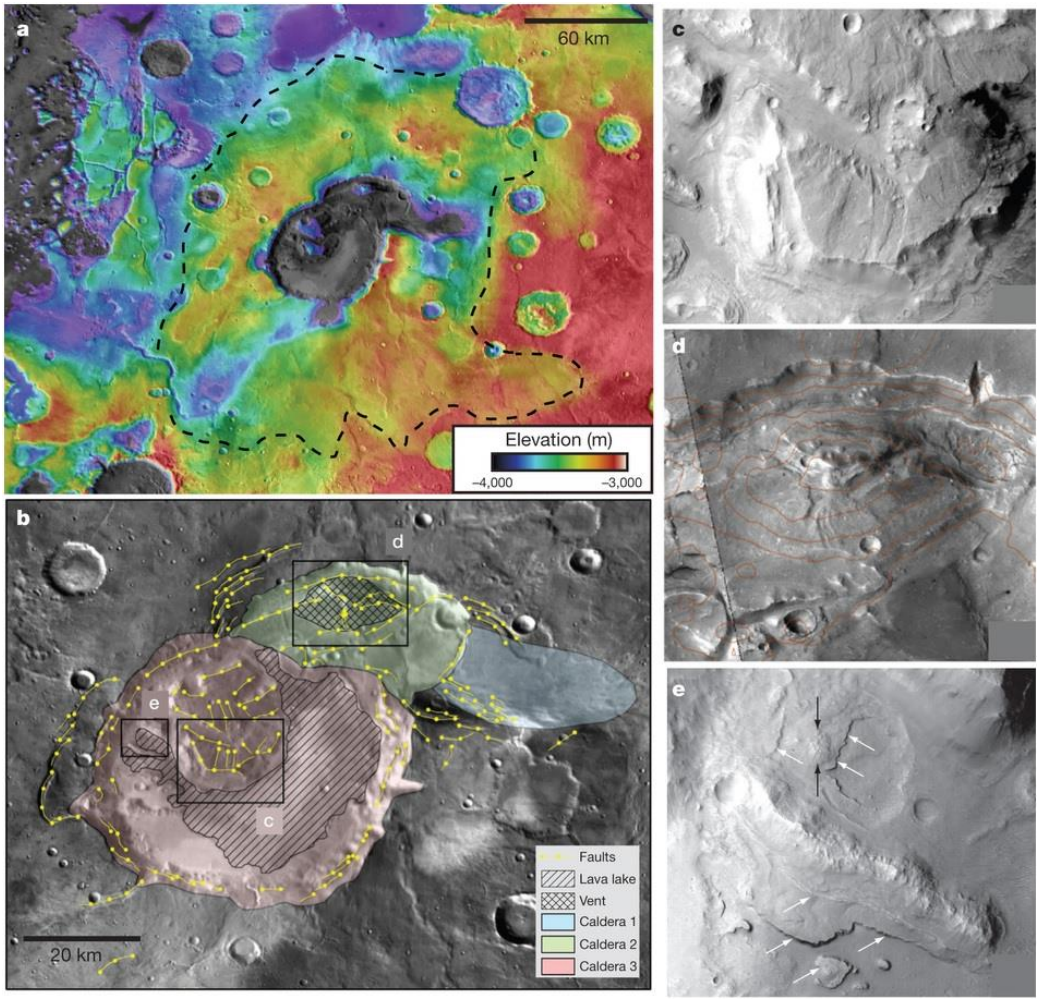

Figure 2: Eden Patera shown here displaying multiple collapse events, as well as volcanic vents and lava lakes (Michalski and Bleacher, 2013).

a caldera complex due to its similarity to terrestrial calderas and a lack of identifiable

impact crater characteristics. This includes a surrounding terrain with ridged plains of Hesperian basaltic volcanism and fault-bounded blocks with surfaces similar to adjacent ridged plain lavas. Other caldera/volcanic characteristics include blocks tilted toward the center of the depression, a mound interpreted as a graben-related vent, and continuous terraces 100 and 150 meters above the floor, interpreted to be high stands of lava lake drainage. The presence of apparent volcanic geomorphic features and faulting consistent with caldera collapse are consistent with interpretations of Eden Patera as volcanic in origin

Although multiple lines of evidence suggest a volcanic origin for Siloe Patera, it is also possible that it originated as the result of multiple impact craters or a combination of an overlapping impact crater and volcano. Comparison of Martian volcanoes and impact craters are explored herein and will aid in the interpretation of Siloe Patera's origin.

Similar to Eden Patera, Siloe Patera contains quasi-circular nested depressions and arcuate scarps, although it is almost 1 km deeper than Eden Patera (Figure 2),with a total depth of ~1700 m. Herein, the overlapping depressions of Siloe Patera are referred to as Crater A the largest and older depression and, Crater B the second and younger in the southern half of Crater A (Figure 3A).Crater A is roughly 37 x 33km in diameter (NS-EW) with an average depth of 1000m, ±100 m, while Crater B is ~28 x 24km with a depth of 700m, ±100 m. Siloe Patera contains a number of notable features (Figure 3B), including parallel mounds as a result of possible ring faulting, on the floor of Crater A. A

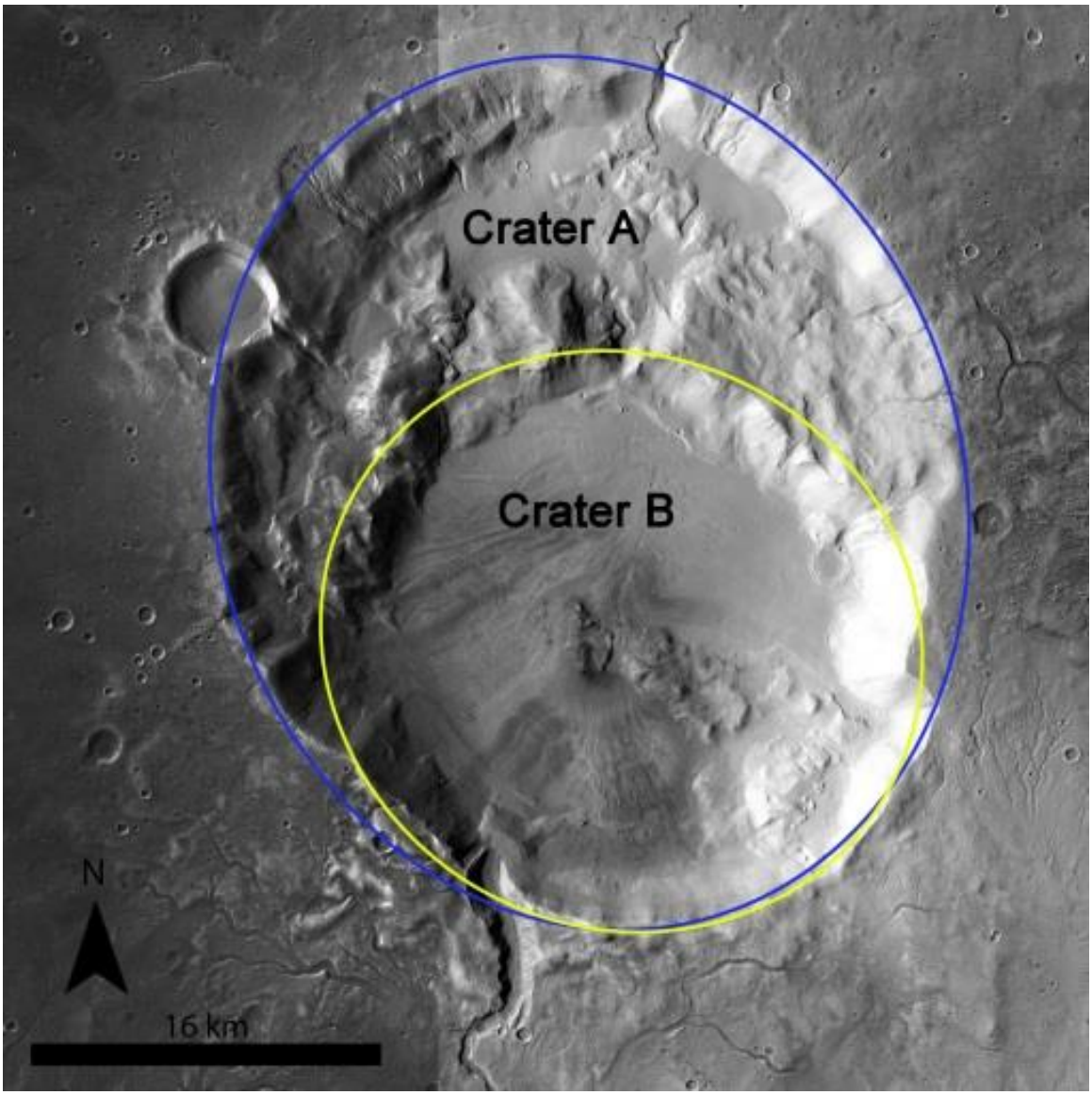

Figure 3A: Siloe Patera divided into two craters. Crater A circled in blue and Crater B circled in yellow.

large mound on the floor of Crater B connects with the southeast rim of Siloe Patera and is referred to as a spire for the purposes of this paper. The spire rises up in elevation from the center of Crater B to the rim of Siloe Patera and is discussed in more detail herein. Apparent flows lacking a definable source are found to the north, southeast, and southwest of Siloe Patera's rim with varying degrees of erosion, length and appearance (Grant and Schultz, 1993). Five mounds found lining the fault scarp of Crater A and

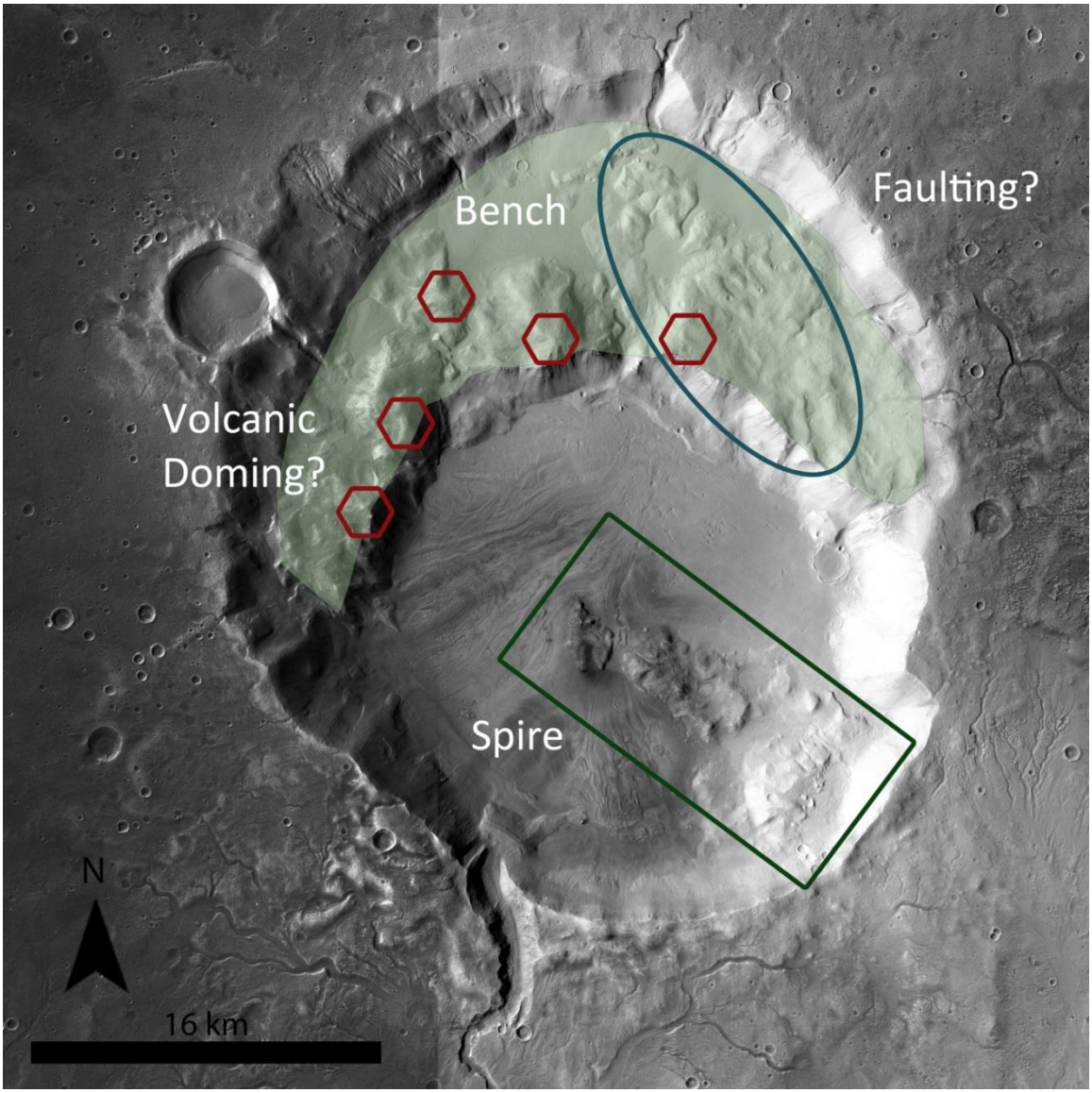

Figure 3B: Regions of interest: (1) volcanic-doming shown in red hexagons; (2) faulting circled in a blue ellipse; (3) a spire encompassed by a green rectangle. The Bench (Crater A's floor) is highlighted in green.

Crater B are uncharacteristic of impact craters and will be discussed in more detail below. Immediately south of Siloe Patera is a large, irregularly shaped depression that links to Crater B at its southern flank. The significance of these regions is discussed below and is critical for understanding the nature of Siloe Patera's origin.

CHAPTER 2

Mars is a dynamic planet with a complex history of geologic processes that have shaped its surface through time. Volcanic features make up more than 35 percent of the Martian surface and cover much of the planet with volcanic fields and plains, including large shield volcanoes such as Olympus Mons (Greeley, 1985). Although volcanism is widespread on Mars, impact craters are the more dominate feature and cover the entire planet. Impact craters and volcanoes can be differentiated from one another other in most cases; however, impact and volcanic processes can result in non-unique geomorphic features that make unequivocal interpretations difficult. In these cases, remote sensing is a very helpful tool as it provides methods that can help to identify rock types by spectrographic signatures and provides insight into the process that may have formed a particular feature.

Three main intervals (Figure 4) in Martian geologic history have been defined based on impact crater size and frequency: Noachian (4.6 to 3.5 Ga); Hesperian (3.5 to 1.8 Ga); and Amazonian (1.8 to present; Scott and Carr, 1978; Figure 4). Tanaka (1986) modified the original time-stratigraphic classification of Scott and Carr (1978) and subdivided the three periods into series referred to as “Upper,” “Middle,” and “Lower” based on research in the western hemisphere of Mars, where detailed imagery suggested stratigraphy in remotely observed outcrops. A second time scale was derived from data gathered by the OMEGA Visible and Infrared Mineralogical Mapping Spectrometer on board the Mars Express orbiter (Bibring et al., 2006). In this new time scale there are three periods: Phyllocian (4.5 to 4.0 Ga); Theiikian (4.0 to 3.5); and

Siderikan (3.5 to present). These chemical periods are determined by the abundance of specific minerals associated with water availability (Bibring, et al., 2006).

Physical History:

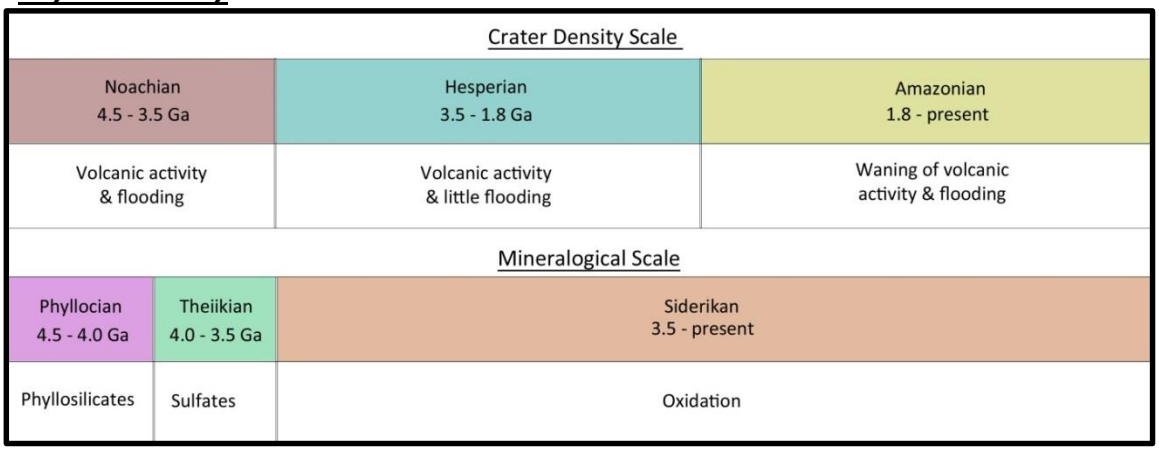

Figure 4: Depiction of the physical and chemical history of Mars.

Noachian Period (4.5 to 3.5 Ga) - Noachian rocks are the oldest, generally the most densely cratered by impacts, and are mainly found in the southern highlands (Scott and Tanaka, 1986; Figure 5).Rocks which formed during this age developed during the final stages of planetary accretion and subsidence associated with the heavy bombardment period. Extensive flood lavas and surface modifications formed from eolian, fluvial, and other surface processes after the heavy bombardment. It is thought that the Tharsis bulge (Figure 5) formed during this time, as well as major flooding by liquid water (Bibring, et al., 2006).

Lower Noachian Series - Recent mapping has distinguished stratigraphically lower "basement material" from cratered terrain material that is scattered over many areas on Mars (Scott and Tanaka, 1986). "Basin rim material" and "mountain material" units

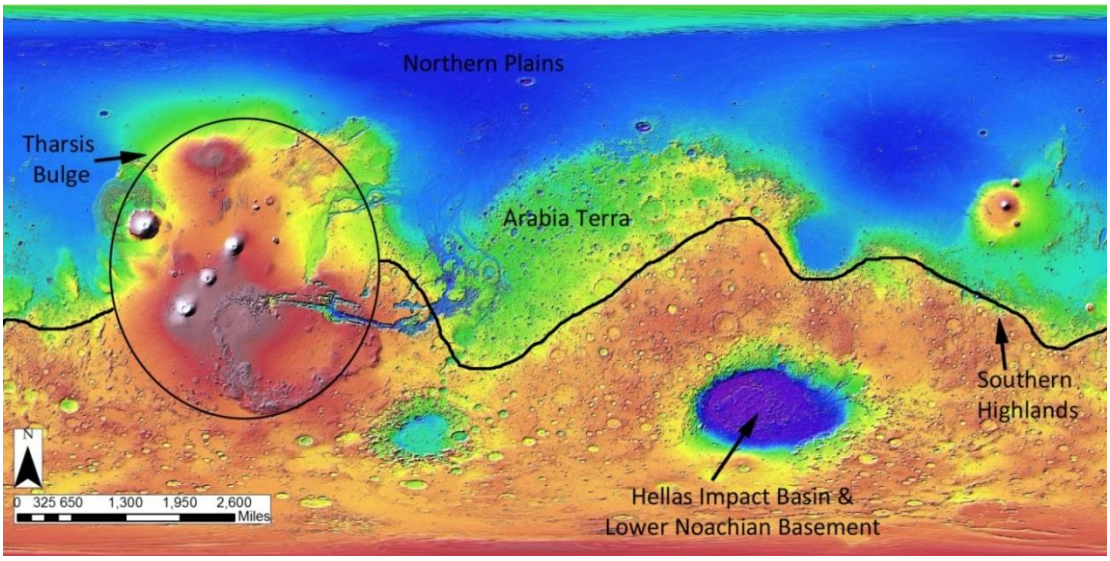

Figure 5: Global Mars map displaying various regions and features.

have been reclassified as basement material within the Lower Noachian Series and are best observed in the uplifted rim of Charitum Montes (Figure 6) surrounding Argyre Planitia. These rims are rugged, heavily cratered from impacts, and faulted with hills and ridges that appear to be concentrically aligned with Argyre Planitia. Middle Noachian cratered terrain material embays much of the Lower Noachian basement and can be found around Hellas Basin (Tanaka, 1986; Figure 5). The Lower Noachian Series represents the most primitive crust of Mars and formed by solidification of the molten surface when the planet was forming (Tanaka, 1986).

Middle Noachian Series - The Middle Noachian Series contains rugged and scattered cratered terrain with remnants in the northern plains. This unit has been mapped as "cratered unit of the plateau sequence" (Tanaka, 1986) and is the most widespread of all of the Noachian Systems. The Middle Noachian Series type region is west of Hellas

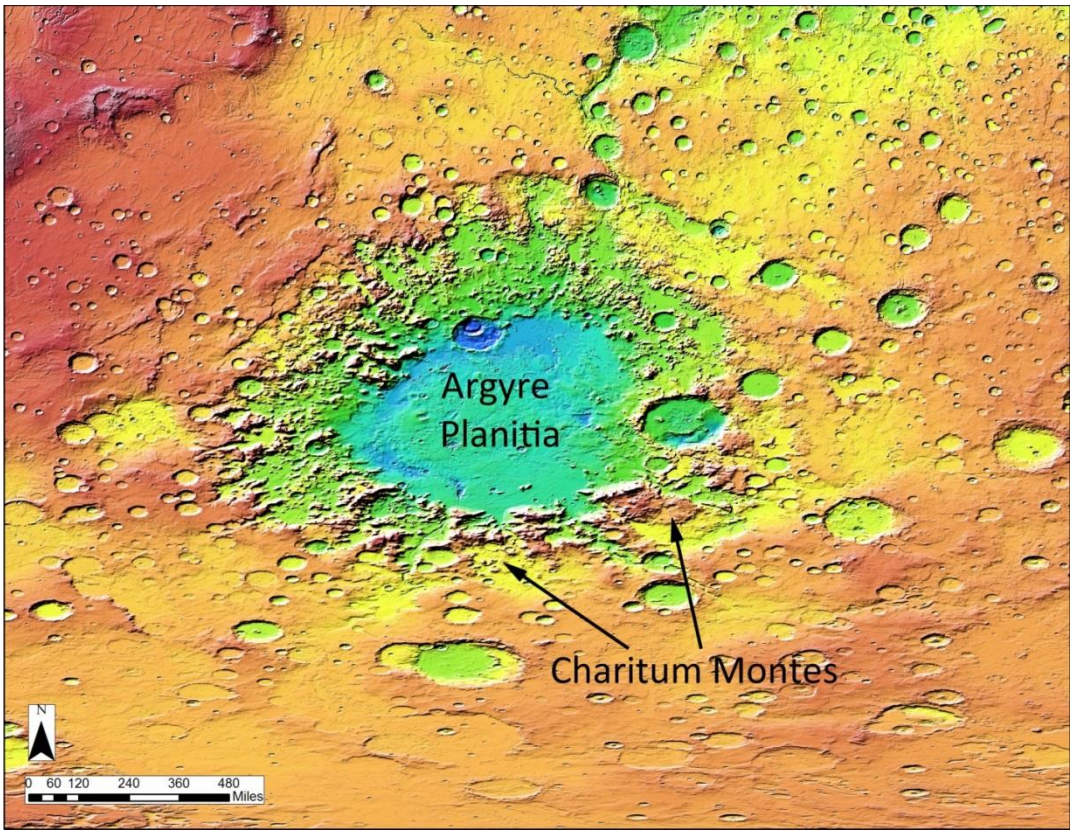

Figure 6: Charitum Montes surrounding Argyre Planitia.

impact basin (Figure 5) and characterized by rugged cratered terrain with moderate high relief, secondary impact craters, wrinkle ridges, scarps, and channels (Tanaka, 1986).

Upper Noachian Series - Defined as "cratered plateau material," the Upper Noachian Series was originally classified as densely cratered with smooth and flat intercrater areas, but recent mapping shows that both units are separate. The smooth, flat portions over the cratered terrains embay the Middle Noachian Series (Tanaka, 1986).

Hesperian Period (3.5 to 1.8 Ga) **-** Hesperian formations and features display extensive volcanism, tectonism, and canyon and channel formation as well as significant

impact cratering (Scott and Tanaka, 1986). Hesperian material appears as thick sheets that cover the highland terrain and partially cover the northern plains. The Tharsis Montes, Alba Patera, and Syria Planum (Figure 7) formed from extensive lava flows during this period which are estimated to have resurfaced more than half of Mars (Scott and Tanaka, 1986).

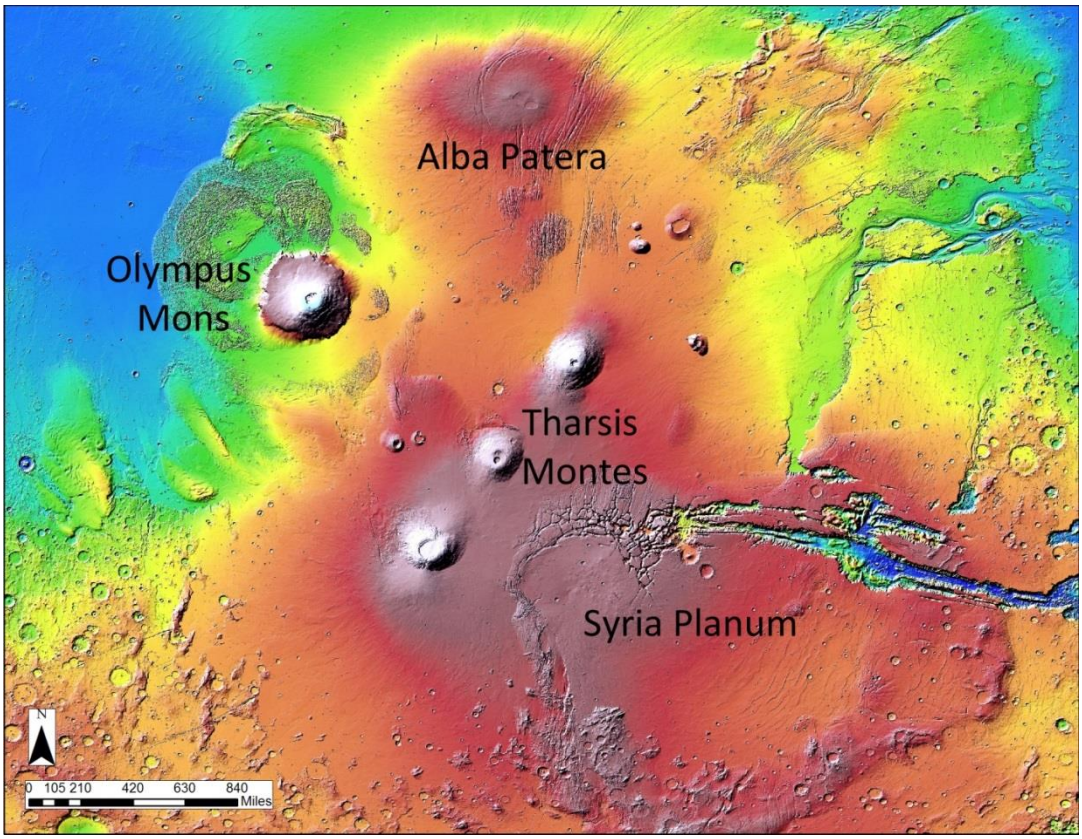

Figure 7: Alba Patera and the Tharsis Bulge

Amazonian Period (1.8 to present) –Materials from the Amazonian Period are usually surrounded by Hesperian-aged materials (Scott and Tanaka, 1986). Amazonian material is interpreted as youngest due to featureless characteristics and presence of eolian material (Scott and Tanaka, 1986).

Chemical History:

Phyllocian (4.5 to 4.0 Ga) - The Phyllocian Period is characterized by phyllosilicates that formed in an alkaline water environment which would match the Noachian Period with its extensive flooding. This time period is thought to be the most likely for hosting life (Bibring, et al., 2006).

Theiikian (4.0 to 3.5 Ga) - The Theiikian Period was dominated by acidic conditions as sulfates from widespread volcanic outgassing and processes mixed with liquid water present at that time (Bibring, et al., 2006).

Siderikan (3.5 to present)–During the Siderikan Period volcanism ceased and liquid water appears to have been largely absent from the Martian surface. The physical processes that dominate during this interval are largely limited to oxidation of pre-existing rock. Iron-rich rocks reacting with atmospheric peroxides would have oxidized the Martian surface, giving Mars its distinct red color (Bibring et al., 2006).

Arabia Terra (Figure 5) has a complex history of erosion, deposition and processes resulting in varying topographic features, impact structures (McGill, 2000) and layered deposits of fine-grained material (Fergason and Christianson, 2008). Supervolcanoes mentioned above (e.g. Siloe Patera, Eden Patera) are found in Arabia Terra and along the global dichotomy boundary separating the Northern Lowlands from the Southern Highlands along a topographic break of 1-3 km (Irwin and Watters, 2004; Watters and McGovern, 2006). Along this boundary are fretted terrain and fretted channels characterized by smooth, flat, lowland areas separated by scarps and complex channels

(Carr, 2001). Fretted terrain is only found in northern Arabia Terra 40° N and between 280° W and 350° W and has been modified by water and ground ice (Sharp, 1973).Fine-grained materialscould be linked to the formation of the fretted terrains and were likely deposited in the early Noachian-Early Hesperian (Irwin and Watters, 2004). These fine-grained materials may source from the proposed volcanic region of Arabia Terra, suggesting the material may be volcanic ash.

The presence of supervolcanoes ultimately changes interpretation of Martian history as magmatism plays a critical role in the formation of Martian crust and habitability and atmospheric chemistry of the planet (Tian et al., 2010). Sulphur cycles, driven by volcanism, control the habitability of soils and rocks on the Martian surface (Halevy et al., 2007) and strongly affect the climate of the planet in a manner similar to volcanic eruptions, here on Earth. Global cooling and warming are possible due to volcanic eruptions as greenhouse gasses emitted can slow the escape of terrestrial radiation, while volcanic aerosols erupted high into the atmosphere can either reflect or absorb solar radiation, preventing it from influencing surface temperatures (Robrock and Mao, 1992). Elucidating the volcanic history of Mars in general, and Arabia Terra specifically, may provide profound insight into many unanswered question about the planet.

Martian volcanism (Figure 8) is primarily analyzed through spectroscopy and photographic data, and is classified based on general morphology. Unfortunately, Siloe Patera falls within the dusty region of the Arabia Terra, rendering spectroscopy useless, although thermal inertia can still be used for insight into the nature of the upper ~1 m

(Fergason and Christensen, 2008). Determination of volcanic constructs on Mars is difficult to establish in detail, and are therefore categorized into two classes: central volcanoes and volcanic plains (Figure 9). Central volcanoes are features that contain 'point source' vents that have accumulated volcanic material. This includes shield volcanoes, domes and other similar features (Greeley and Spudis, 1981). Volcanic plains are identified as broad, generally flat-lying units potentially exhibiting flow fronts and other volcanic features associated with effusive eruptions (Greeley and Spudis, 1981).

Central volcanoes are subdivided into five categories that display point vent features: Alba Patera, highland patera, shield volcanoes, dome volcanoes, and miscellaneous central vent volcanoes (Greeley and Spudis, 1981). Alba Patera is a unique feature that is similar to shield volcanoes with low relief, but also contains sheet and tube-fed flows. The type volcano for Highland Patera is Tyrrhena Patera which is characterized by low relief, complex calderas and radially textured channels. Shield volcanoes on Mars are best typified by Olympus Mons, which contain tube-fed flows, have moderate relief and broad slopes. Finally, domes are characterized as volcanoes with steeper sides and are best represented by Tharsis Tholus. Although Siloe Patera does not completely fit into any of the above categories, it does have some characteristics typical of Highland Patera. Highland Patera is characterized by low profiles, complex calderas and channels that radiate out from the caldera (Greeley and Spudis, 1981). Siloe Patera does not include radial channels, but instead has a low profile, a complex caldera and is situated in the northern hemisphere where Highland Patera is generally found (Greeley and Spudis, 1981).

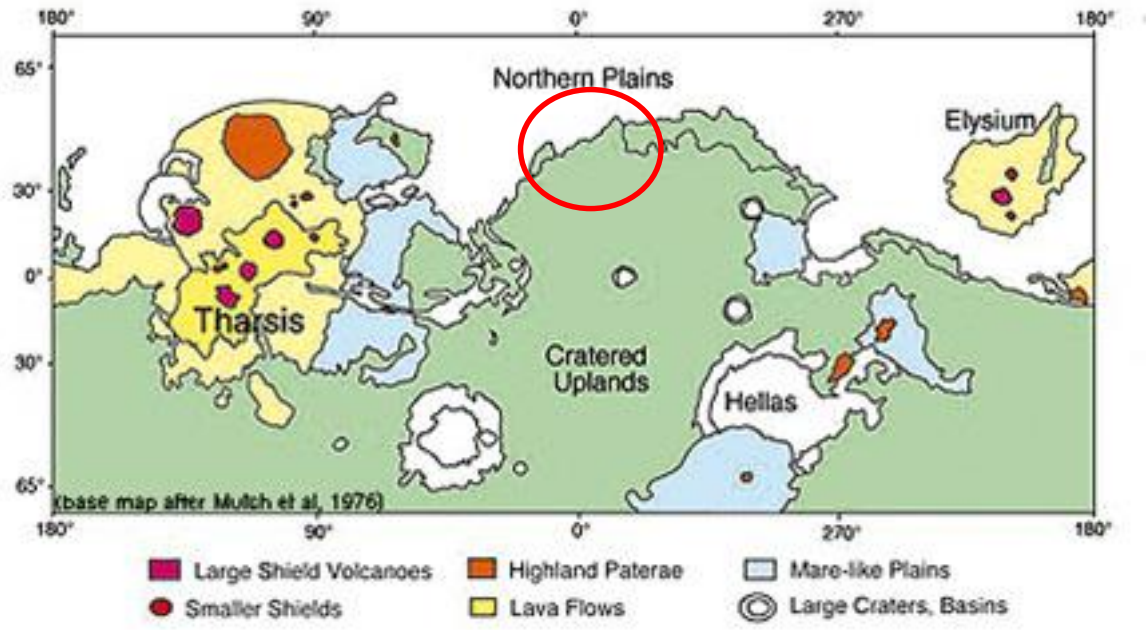

Figure 8: Volcanism on Mars Multch et al., 1976. Circle indicates general area of Siloe Patera and other supervolcanoes proposed.

Volcanic plains are categorized into four types: simple flows, complex flows, undifferentiated flows and questionable flows (Greeley and Spudis, 1981). Simple flows, similar to those observed in Hesperia Planum (Figure 10), are regional and contain wrinkle ridges without flow lobes. Complex flows have an abundance of flow lobes, are complex and unlike simple flows, rarely have wrinkle ridges. These flows are best seen in the Tharsis Plains near Olympus Mons (Figure 11). Undifferentiated flows, common in the northern plains (Figure 5), rarely have flow lobes and provide very little insight into their origins, but are likely volcanic. Lastly, questionable flows are heavily modified by erosion, fracturing, and mass wasting. Like the central volcanoes, Siloe Patera does not fully fit into any of the volcanic plain categories, but instead has a combination of features typical of Martian volcanic regions. To the southwest of Siloe Patera (Figure 43), a possible lobe flow emanates out of Siloe Patera's rim and extends for ~ 45 km.

VOLCANIC PLAINS
Simple flows
s_3 upper Hesperian
s_2 lower Hesperian
s_1 plateau plains
Complex flows
c_2 Tharsis age
c_1 Elysium age
Undifferential flows
CENTRAL VOLCANOES
sh shields
d domes
AP Alba Patera
hp highland patera
QUESTIONABLE
v volcanic materials?

One area of overlap indicates multiple lobe flow events (Figure 43), while regions to the northwest and southeast look very similar to mare-type wrinkle ridges. These flows are thought to be the result of fissure eruptions that rapidly expel large amounts of lava and are common as basin fill and resurfacing of highland terrain (Greeley et al., 2005).

Although calderas are generally similar in origin and geomorphic character, independent of the planet they form on, the specific processes by which they develop vary slightly and they range from complex features that form by collapse, explosive eruptions and erosion (Greeley, 1994), to depressions formed in response to depletion of a shallow magma chamber (Cattermole, 1989; Frankel, 1996).

Martian calderas are categorized into two main types: Olympus-type and Arsia-type (Crumpler et al., 1994). Olympus-type caldera (Figure 12A) are characterized by faulting that defines depression boundaries with arcuate scarps or nested depressions, inward facing faults, and a scalloped appearance that adds to the chaotic nature of this type of caldera. The Arsia-type caldera (Figure 12B) is defined by having a caldera that is larger diameter in relation to its host volcano, a sag-like profile, gently sloping walls, and multiple boundary faults. Of these two Siloe Patera is more typical of Olympus-type caldera as they both display sharp arcuate faults, nested depressions, and a chaotic and scalloped appearance (Crumpler et al., 1994).

All of the features described above can be identified due to their geologically young age and the lack of time for erosion to modify the feature. Very little is known about ancient Martian volcanism as older volcanic features on Mars are highly modified

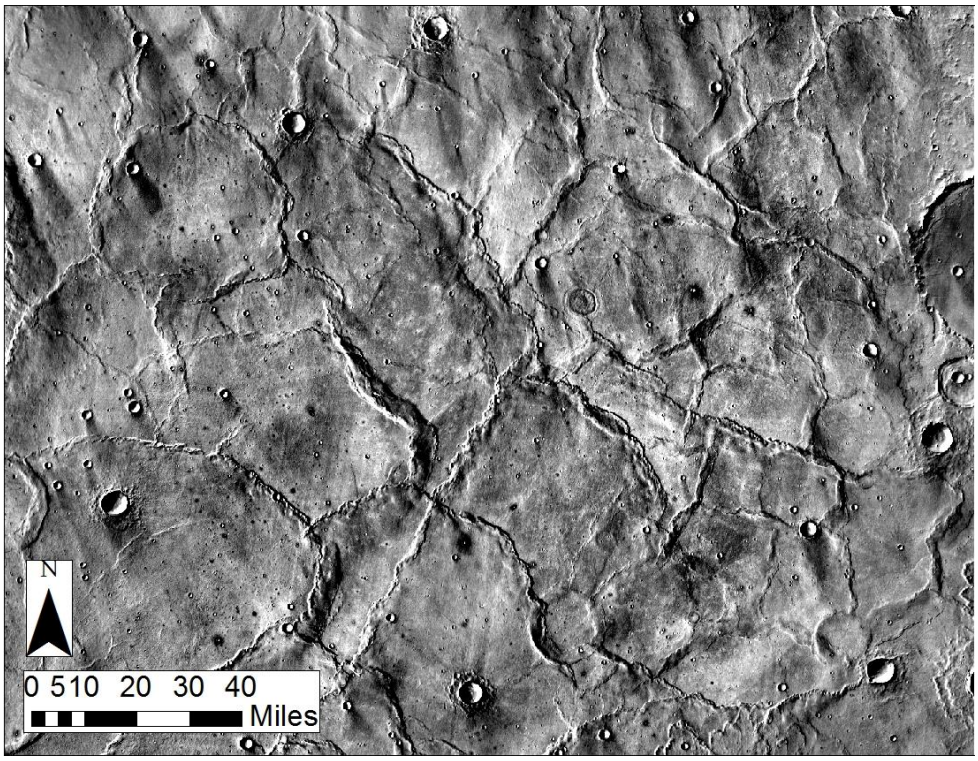

Figure 10: Simple flows near Hesperia Planum.

or have been completely removed by erosion, or have been potentially misidentified as impact features.

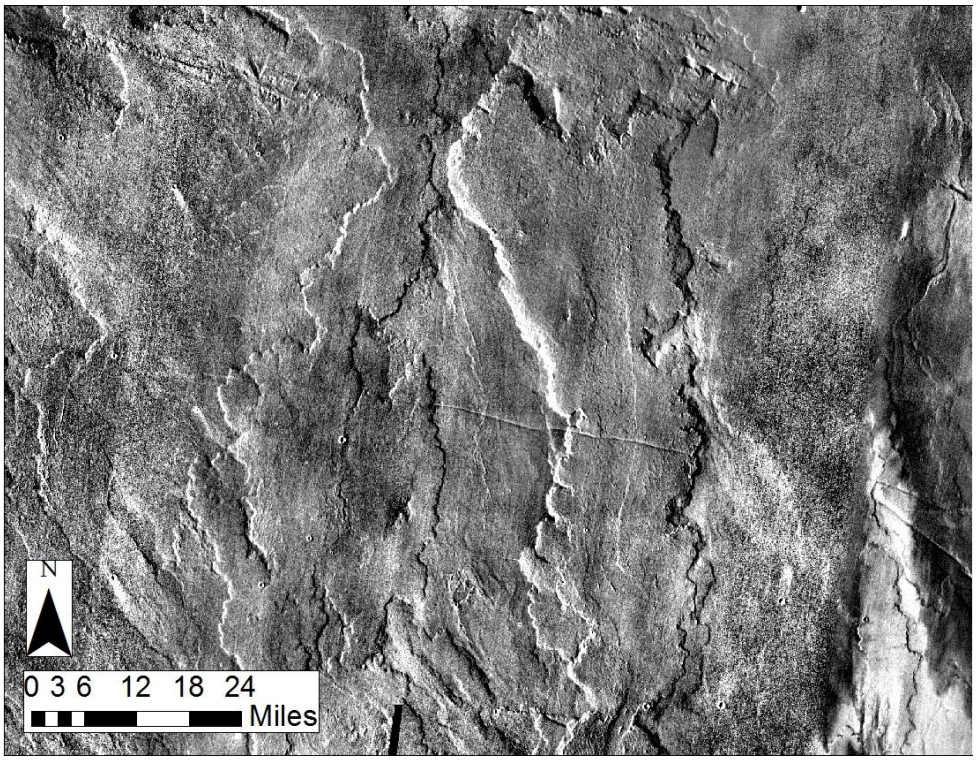

Figure 11: Complex flows on the plains near Olympus Mons.

Previous studies detailing the caldera collapse process can be used to compare structures in and surrounding the area of Siloe Patera to those of caldera. Acocella (2006) sorted caldera collapses into four stages (Figure 13) based on twelve experimental sets that use a variety of different magma and crustal chemistries. Stage 1 of caldera collapse begins with elastic deformation resulting in gently inward-dipping structures that creates broad regions of subsidence on the surface. Stage 2 is attained when subsidence creates a faulted ring that propagates from the magma chamber out to the surface and is characterized by outward-dipping reverse faults. Stage 3 is characterized by flexures that form outside of the reverse faults. These flexures eventually turn into a ring of normal faults that are separate from the smaller ring of reverse faults form in stage 2. Stage 4 is the final stage and is reached when the inward-dipping faults developed in stage 3 reach the surface and eventually begin slipping, resulting in a caldera collapse (Acocella,2006). Siloe Patera has features which are consistent with this model of caldera evolution, with the exception of the southern rim. This region contains only one area of collapse, which could be the result of an incomplete stage four in this area, or spatial overlap of ring faults from stage three and four (Figure 13).

Resurgent calderas form in seven systematic stages associated with volcanic, structural, and sedimentary processes (Smith and Bailey, 1968; Figure 14). These stages

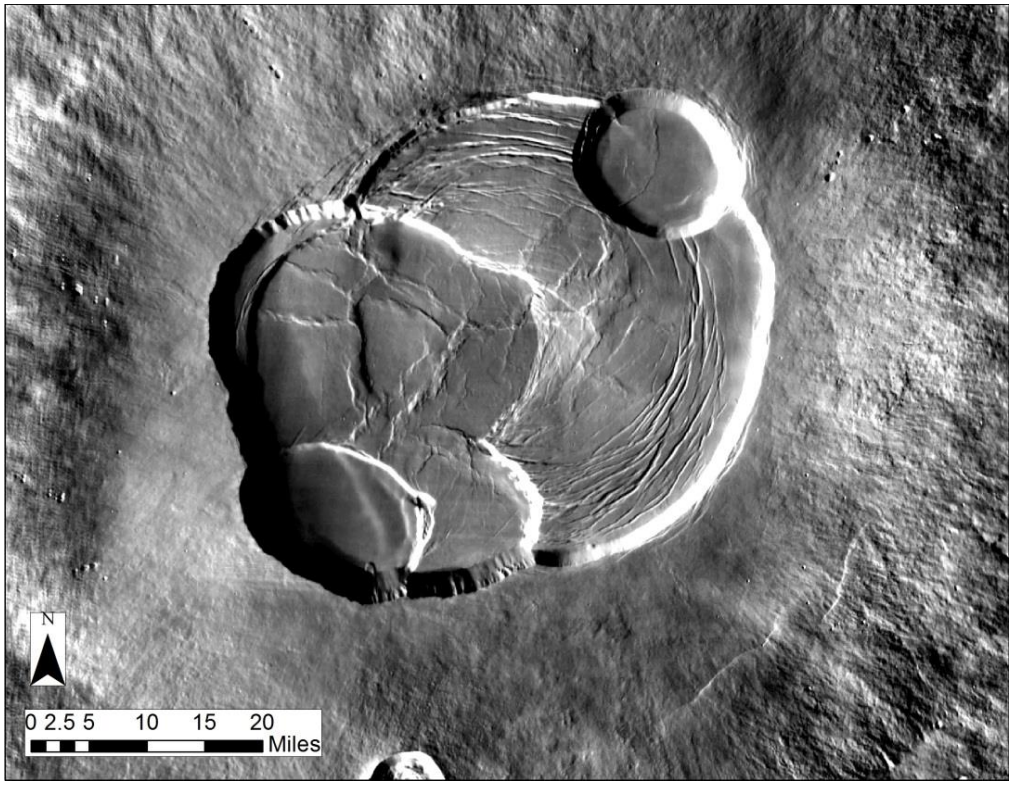

Figure 12A: Olympus-type Martian caldera.

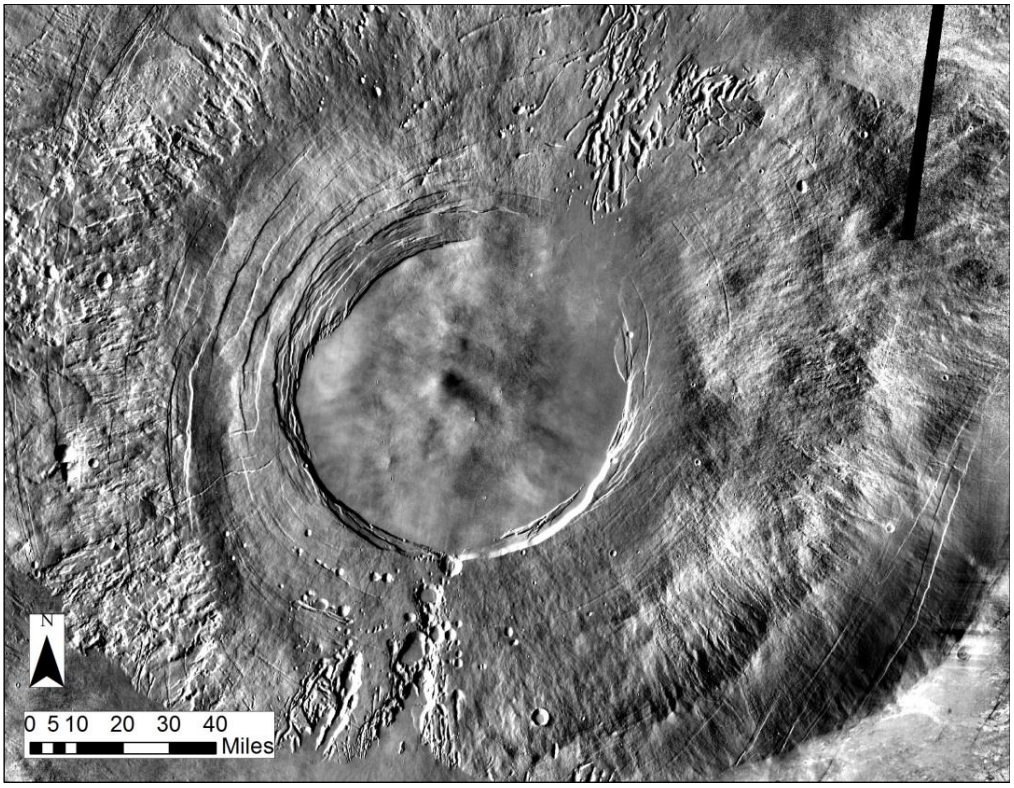

Figure 12B: Arsia-type Martian caldera.

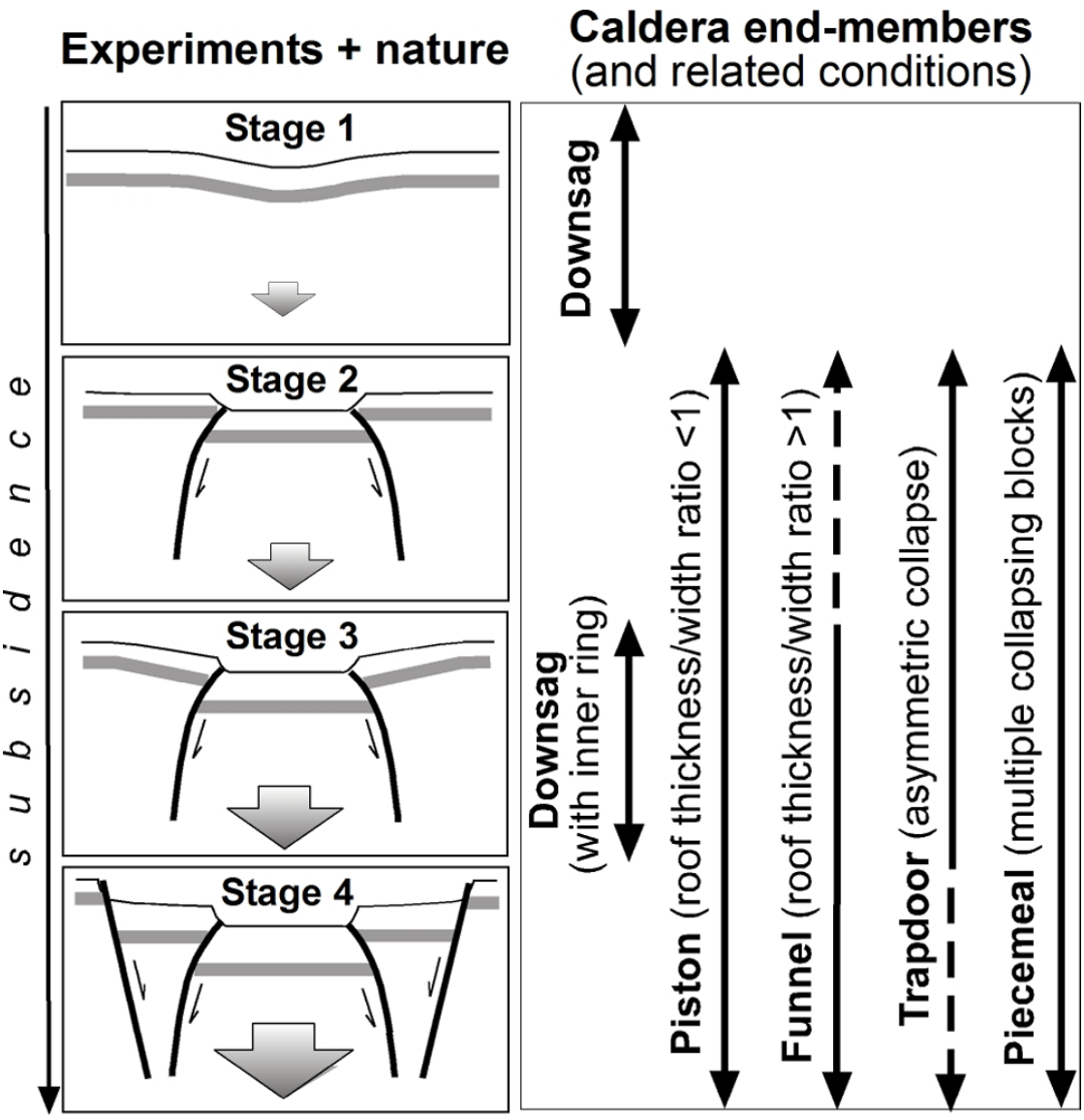

Figure 13: Depiction of caldera collapse stages as described by Acecolla 2006).

are based primarily on work in Valles Caldera, as well as evidence from other calderas. Stage I begins with regional tumescence and ring fault propagation due to magma chamber pressure increasing and magma intrusions. This can result in eruptions along ring and radial fractures. Stage II begins when large volume ash-flows erupt and terminate the regional tumescence of Stage I. Ash-flow cycles generally generate pyroclastic eruptions ranging from 50 to 500 cubic miles in volume. Debate continues as

to the duration of eruptions due to complex ash cycles and makes generalization

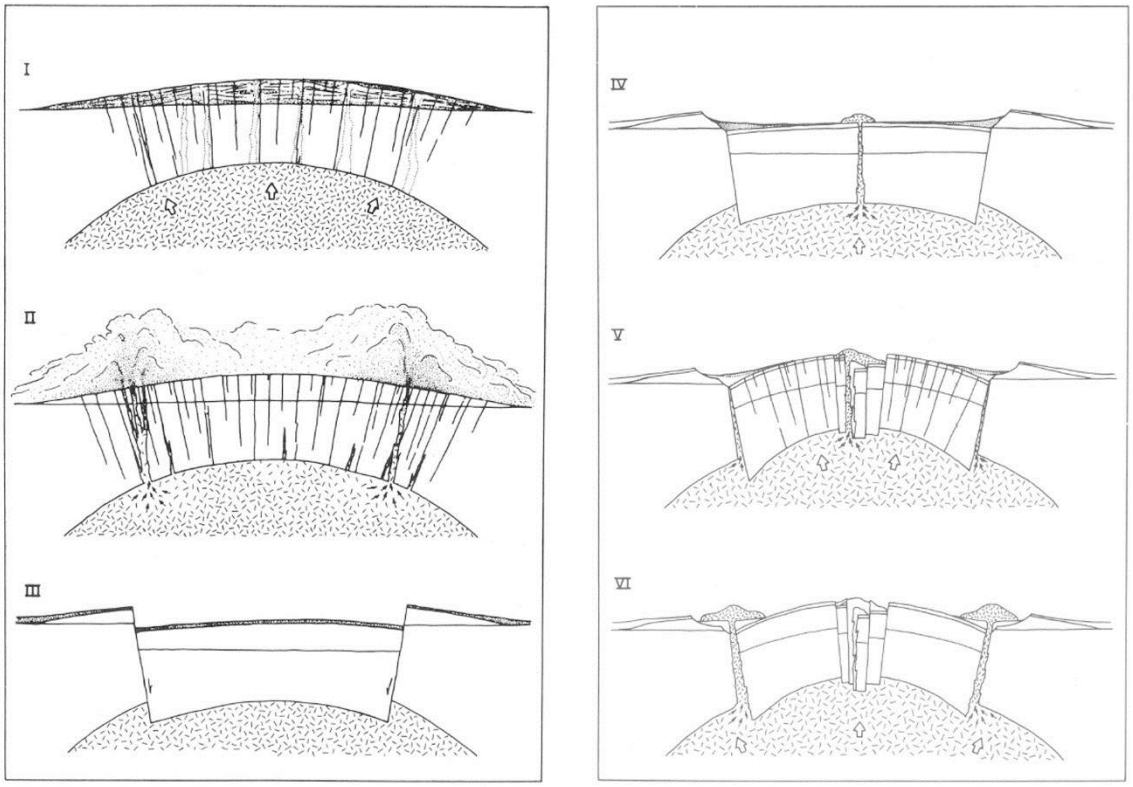

Figure 14: Depiction of the first six stages of resurgent calderas (Smith and Bailey, 1968). Stage I, Regional tumescence and generation of ring fractures. Stage II, Caldera-forming eruptions. Stage III, Caldera collapse. Stave IV, Preresurgence volcanism and sedimentation. Stage V, Resurgent doming. Stage VI, Major ring-fracture volcanism. Stage VII, not shown as volcanic activity is waning (Smith and Bailey, 1986).

difficult. Caldera collapse starts off Stage III. As collapse and subsidence of the caldera is a natural consequence of the removal of large volumes of material from the magma chamber during Stage II. Stage IV is short and accompanied by large amounts of erosion due to caving and avalanching of the newly formed steep caldera walls. During this time of erosion, in-fill, and lake formation on top of the caldera, partial magma pressure is restored. Resurgent doming starts off Stage V. Inital horizontal beds are uplifted to steep dips that can exceed 65° to form the beginnings of a dome. In-fill continues and lakes may overflow and breach the caldera. Ring fractures are reopened and provide

settings for regional tumescence and potential resumption of Stage II eruption cycles. Despite the active volcanism, caldera fill continues at a rate greater than erosion. Following cessation of volcanic activity, fumaroles and hot-springs form, indicating the beginning of the final stage, Stage VII. At this point the caldera reaches a terminal stage due to waning volcanic activity with long-lived hydrothermal activity creating the potential for major ore deposits (Smith and Bailey, 1968).

The region of northern Arabia Terra has been suggested as a new volcanic field consisting of Martian supervolcanoes based on geomorphology; however, this may be the result of explosive basaltic volcanism associated with crustal thinning and high gas pressures. Supervolcanoes have been historically recognized on Earth only and are characterized by subcircular, negative topographic features and a caldera size that correlates with the eruption size (Miller and Wark, 2008). On Earth, these supervolcanoes require high contents of volatiles such as H^2O and CO^2 as well as melts of high enough viscosity to amplify pressure on the magma chamber. The main difference between normal volcanoes and supervolcanoes is amount of the available material that can be erupted from shallow magma chambers. Due to their enormous eruptive size, the frequency of these types of eruptions correlates inversely to the eruption size (Miller and Wark, 2008).

Valles Caldera in New Mexico (Figure15) provides a terrestrial analog for comparison of extraterrestrial supervolcanoes, including Siloe Patera. Valles Caldera is

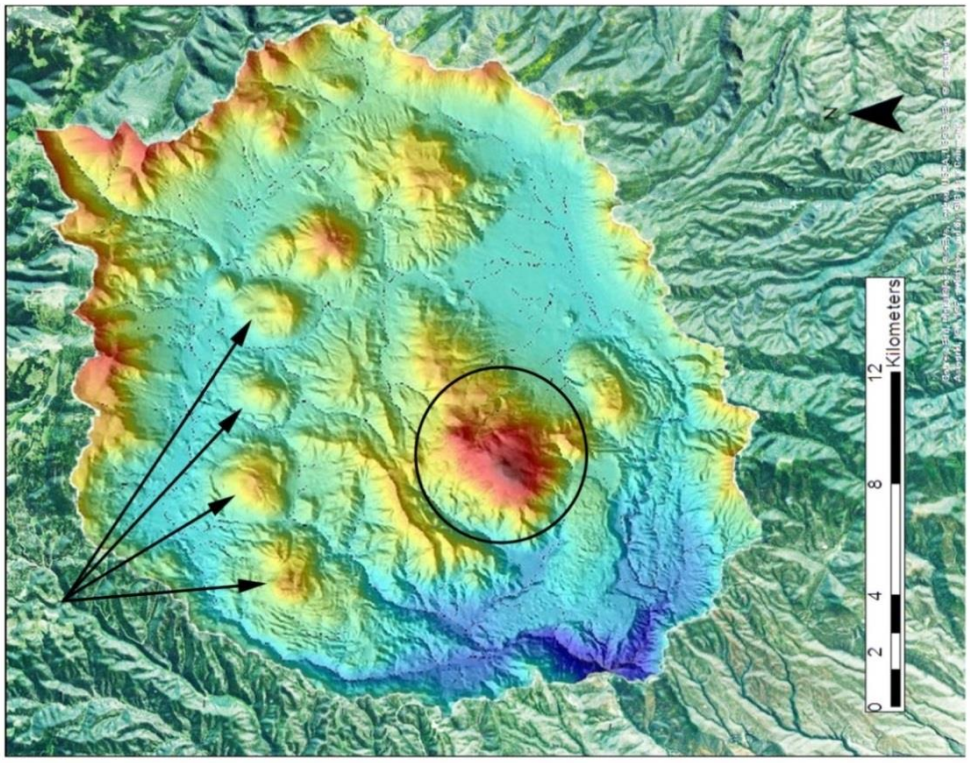
N
0 2 4 8 12
Kilometers

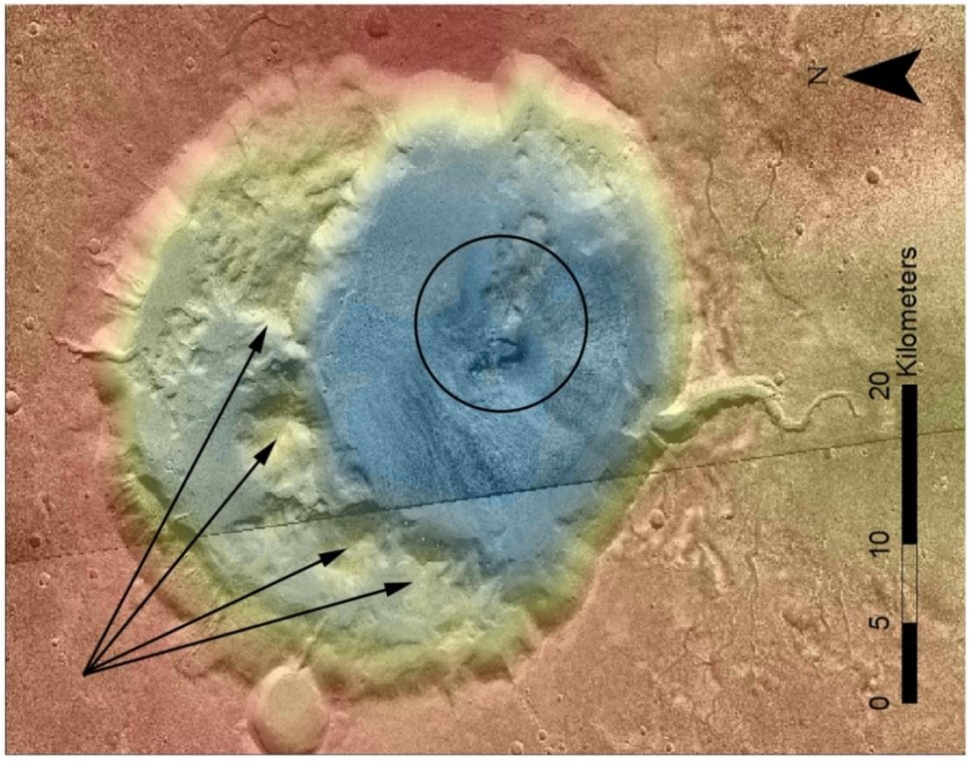
N
0 5 10 20
Kilometers

roughly 20-25 km in diameter and displays scalloped walls that rise hundreds to more than 600 meters above the present floor, very similar to Siloe Patera. Redondo Dome, a resurgent dome, lies in the center of the caldera with diameter of 10-15 km and rises nearly 900 meters. Surrounding Redondo Dome to the north is a discontinuous ring of 10 isolated rhyolitic volcanic domes, with dimensions of 1-3 km at the base and a relief of 150-600 meters (Smith and Bailey, 1968). Two main collapse events form Valles Caldera: the first event created Toledo caldera and the second created Valles caldera as we see it today. Only a small portion of Toledo caldera is preserved due to later eruptions that crated Valles caldera. The formation of Valles caldera began with a large eruption from a ring-fracture system, leading to the subsidence a 10-15 km block at a depth of 600-900 meters (Smith and Bailey, 1968). Both Siloe Patera and Valles caldera include deep depressions, although Siloe Patera has a depth almost double that of Valles caldera. They share a number of commonalities, including evidence for multiple collapse events, a discontinuous ring of volcanic vents/domes and a resurgent caldera or cinder cone/dike similar to Kilauea caldera in Hawai'i (Figure 16a and 16B). The Kilauea caldera is circular with deep, arcuate scarps and two main depressions, indicating multiple collapse events like those proposed for Siloe Patera. These features are difficult to explain with nested impact craters or multiple impact events that overlie each other.

Because of similarities in the surface expressions of caldera and impact sites, impact crater morphology will be compared to Siloe Patera in order to establish a less equivocal interpretation of its origin. Impact craters can be generally divided into simple

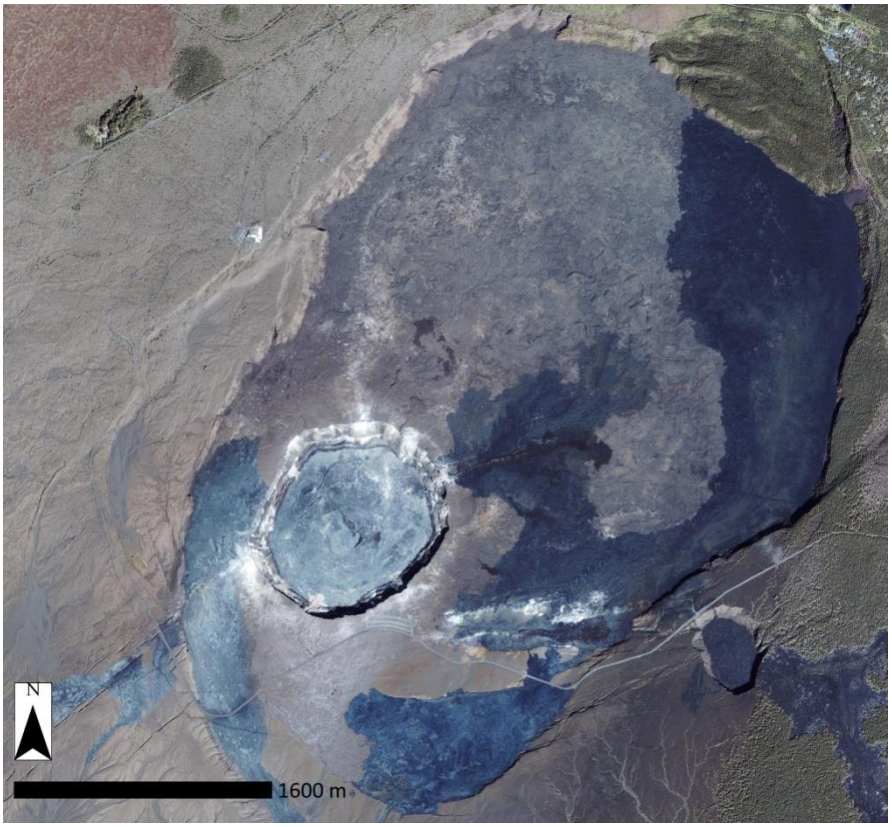

Figure 16A: IKONOS image of Kilauea caldera from NASA's Earth Observatory Image of the Day, December 10, 2005.

Figure 16B: Kilauea Caldera viewed from the west. Image from USGS Hawaiian Volcano Observatory website.

and complex craters (Pike, 1980; Figure 17). Fresh simple impact craters characteristically show overturned strata with overlying ejecta and a bowl-shaped

depression that is partially filled. Complex craters are similar to simple craters except they may also contain interior morphology such as central peaks and walls which develop from listric faulting, producing a chaotic terrane (Osinski and Pierazzo, 2012).

Impact crater ejecta is identified and classified into three categories (Figure 18): (1) “single layer ejecta” (SLE) that contains one ejecta layer; (2) “double layer ejecta” (DLE) which contains two complete layers; and (3) “multiple layer ejecta” (MLE) that has three or more partial or complete ejecta layers (Barlow et al., 2000). SLE craters typically range in size of 3 to 50 km in diameter, DLE craters range between 4 to 26 km and MLE range in between 8 to 59 km (Dohm et al., 2007). Siloe Patera, with a diameter of ~ 30-40 km, falls into the same size category as SLE and MLE craters. SLE and MLE craters also have depths similar to Siloe Patera, ranging from 1-2 km (Dohm et al., 2007). Because of the similarity of dimensions between Siloe Patera and impact craters containing SLE and MLE, we should expect to see either SLE or MLE ejecta if Siloe Patera formed from impact craters. Various flow features that propagate out from Siloe Patera’s rim could be interpreted as portions of SLE or MLE ejecta that have been severely eroded (Figure 43).

Relative ages of impact craters can be determined by the modified nature of the impact crater (Figure 19). Fresh impact craters display deep bowl-shaped depressions with smooth walls and floors and contain very little erosional modification. Slightly

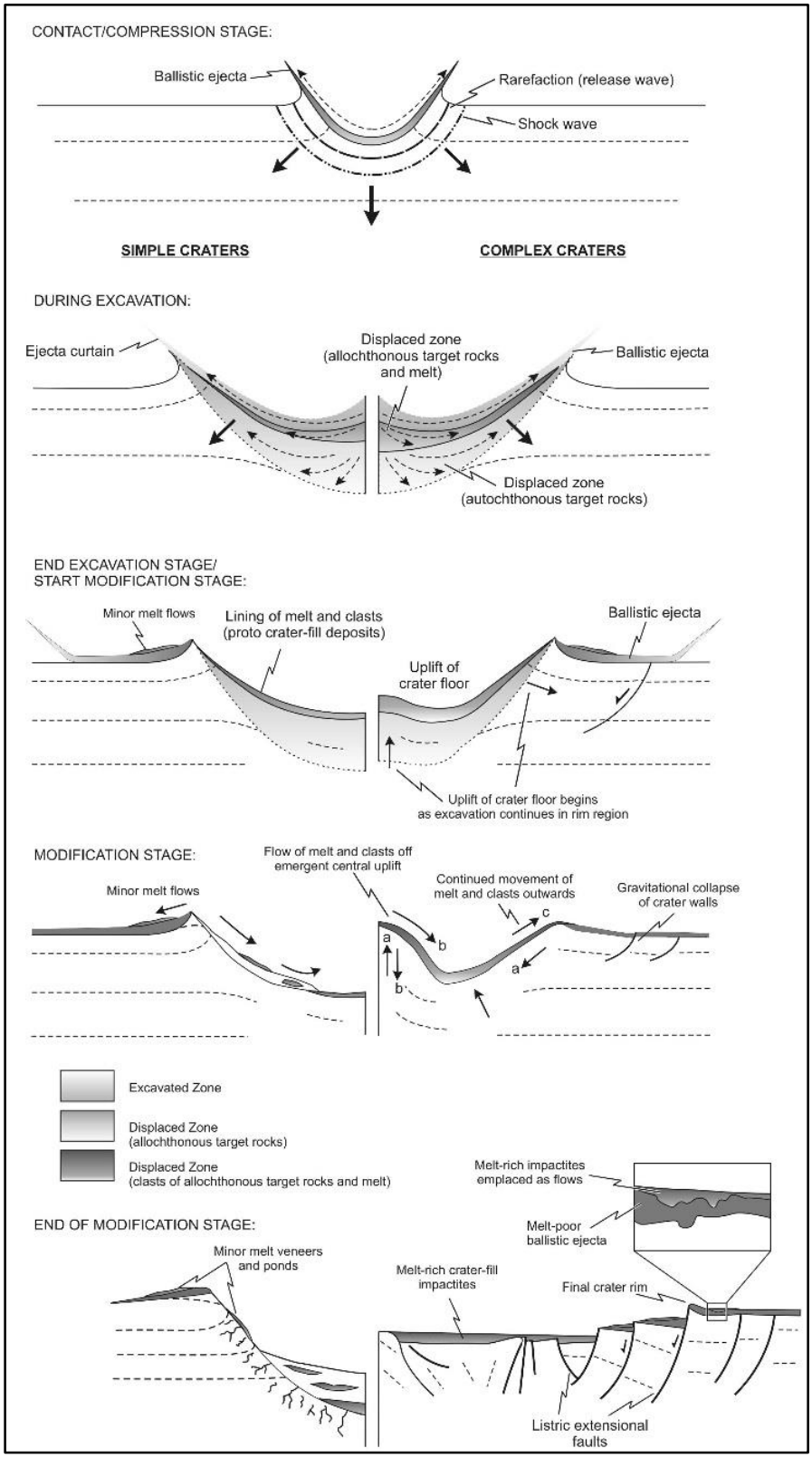

Figure 17: Depiction of simple and complex impact craters, their processes and final results. Simple impact craters on the left and complex on the right (Osinski and Pierazzo, 2012).

modified impact craters appear similar to fresh impact craters, being deep and fresh in appearance, but with a flat floor and modification to walls. Modified impact craters become shallower and are subjected to significant modification due to erosion. When impact craters appear to be erosional remnants with flat floors and significantly shallow, they are considered to be ghost impact craters (Grand and Shultz, 1993; Arvidson, 1974).Due to Siloe Patera's age of Noachian/Hesperian it should be considered a ghost crater having significant time to erode and modify. However, Siloe Patera's depth to diameter ratio plots it in between fresh and modified craters that are discussed later.

Central peaks are common in many impact craters as isolated mounds on the crater floor (Smith, 1976). If Siloe Patera were the result of an impact crater, a single central peak is expected on the floor of Crater B. There are nine classes of interior structures that are associated with complex craters (Barlow, 1990): a) symmetric pit crater; b) asymmetric pit crater; c) summit pit crater; d) central peak; e) peak ring; f) flat floor –pristine; g) flat floor – deposits; h) complex; and i) unclassified (Figure 20). The mound present in the center of Crater B of Siloe Patera (Figure 3B), is not isolated or symmetric and extends out to the rim wall. Due to asymmetric nature of the internal mound, its morphology would be classified as complex. The origin of this feature is more likely a result of mass wasting from the caldera rim or a resurgent dome associated with post-eruptive Stage V caldera processes.

Remote sensing is a very useful tool on Earth as every object reflects or emits characteristic electromagnetic radiation that can be measured from a distance by

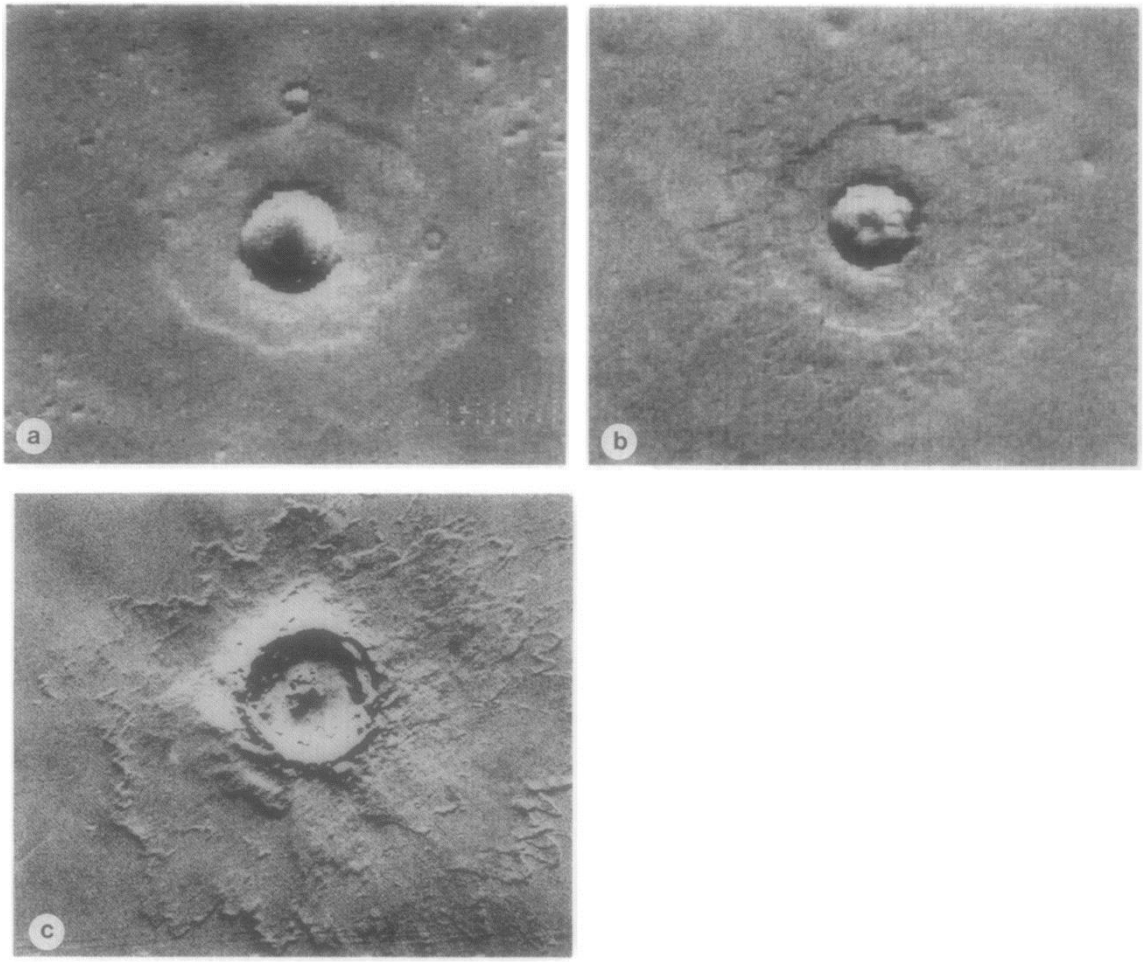

Figure 18: Examples of Single Layer Ejecta (A), Double Layer Ejecta (B), and Multiple Layer Ejecta (C) from Barlow 1990.

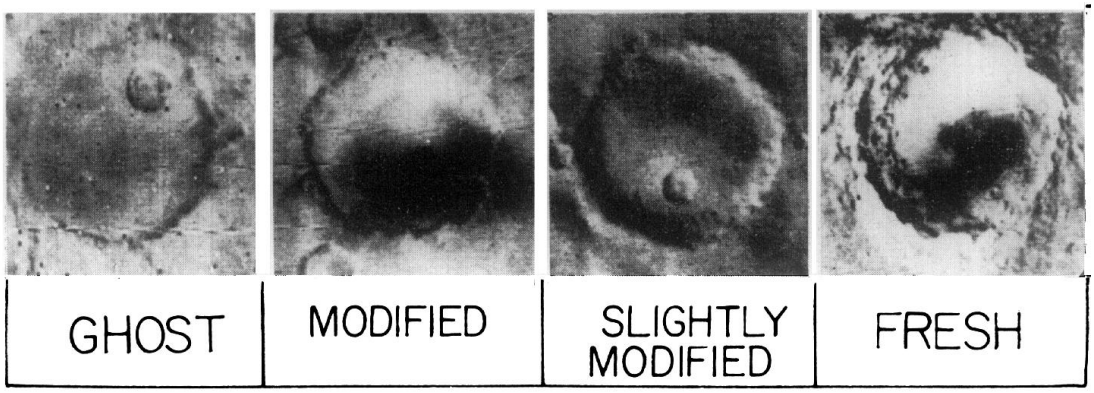

Figure 19: Variation of crater degradation (Arvidson, 1974).

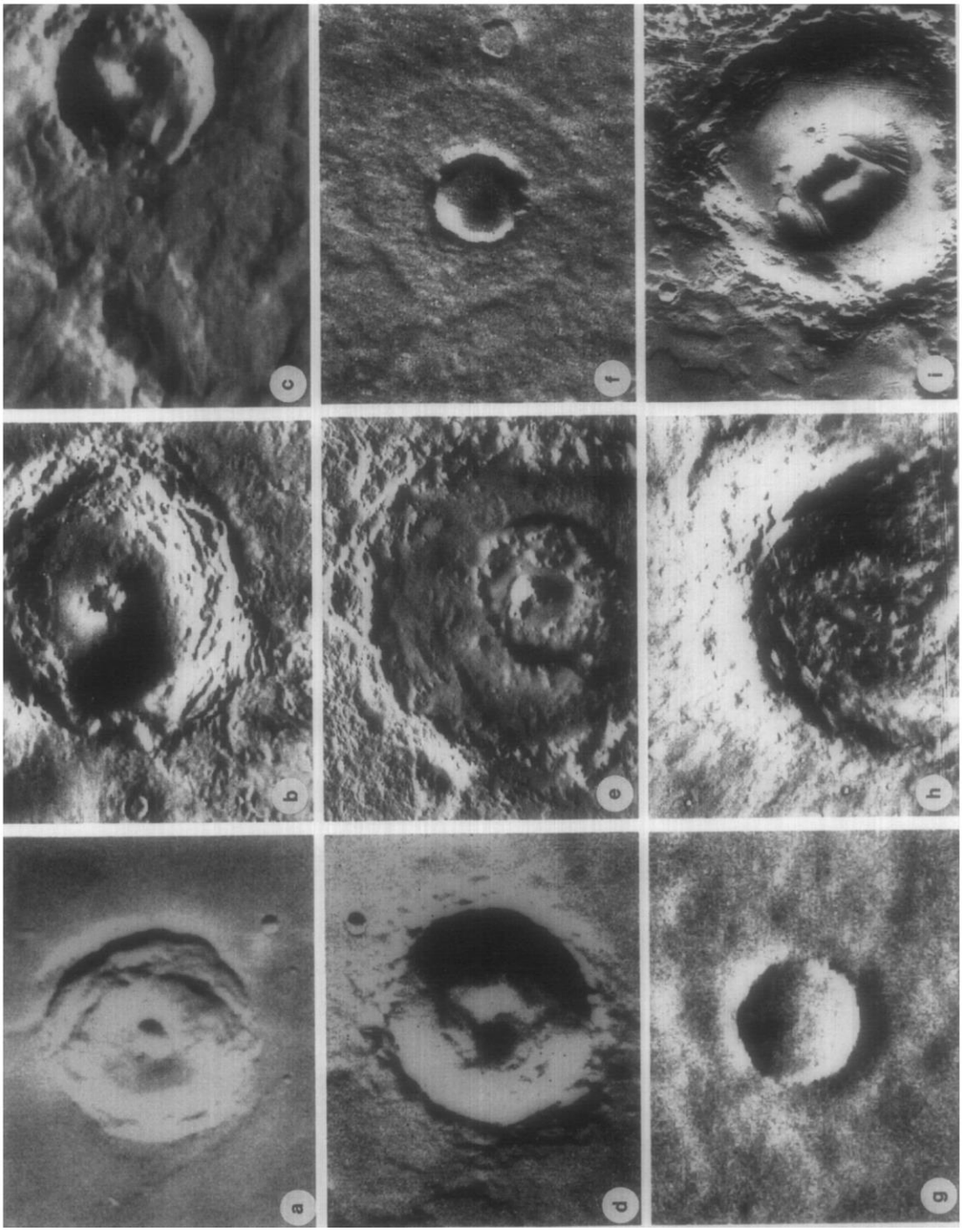

Figure 20: Internal morphology of craters (Barlow, 1990).

sensors designed for the purpose (Vincent, 1997). With the help of remote sensing, many areas can be monitored remotely and used to distinguish different types of land cover. This is done by measuring the wavelengths of certain objects with multi-spectral sensors where each object has a specific spectral signature. The wavelengths typically utilized for this purpose include visible light, (wavelengths of 0.4 – 24.0 μm: blue = 0.4 μm, green = 0.5 μm, and red = 0.6 μm) short wavelength infrared (SWIR: 1.0-3.0 μm), mid wavelength infrared (MWIR: 3.0-5.0 μm), long wavelength infrared (LWIR: 8.0-14.0 μm), and very long wavelength infrared (VLWIR: 14.0 to 24.0 μm). The region from 5.0-8.0 is unnamed because the Earth absorbs almost all of the electromagnetic radiation for this range (Vincent, 1997). Figure 21 shows different spectral signatures for typical land cover found here on Earth.

Although remote sensing is highly effective in differentiating between different types of surface cover on Earth, it presents difficult when attempting to analyze Martian surfaces. The widespread presence of oxidized rock and sediment on Mars presents a uniform color reddish-brown color, so visible light classifications are not useful for differentiate geologic classes on the Martian surface. However, infrared radiation is very useful when dealing with rocky regions as rocks will absorb energy during the day and release that energy at night, appearing brighter than the surrounding area. Infrared maps are generally more successful for producing geologic maps of Mars and other planets (Vincent, 1997).

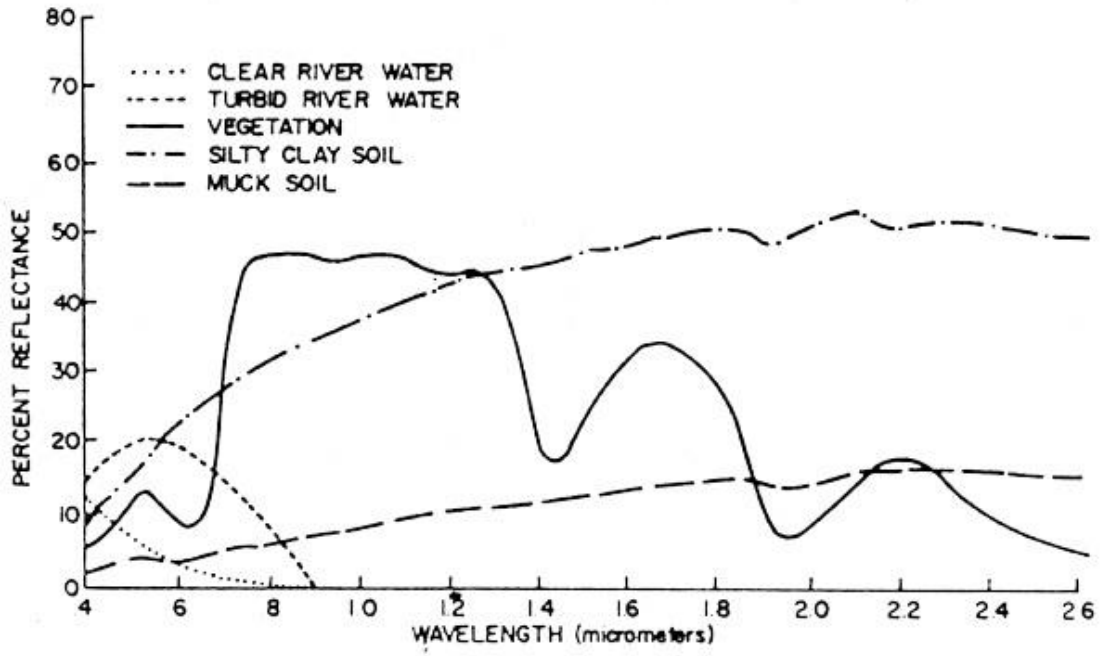

Figure21: Spectral signatures for remote sensing are generally shown as a combination of percent reflected back to the sensor and the wavelength in which it appears. Different materials will present the same spectral signature independent of region, time, and season (Meaden and Kapetsky, 1991).

CHAPTER 3

Multiple data sets were acquired from a variety of sources and used to compare and analyze Siloe Patera. Data sets include Mars Orbital Laser Altimeter (MOLA) , Mars Orbital Camera (MOC), High Resolution Imaging Science Experiment (HiRISE), Context Imager (CTX), and Thermal Emission Imaging System (THEMIS).

The Mars Orbital Laser Altimeter (MOLA) was launched on board the Mars Global Surveyor (MGS) in 1996 from NASA with primary objectives to globally map the topography, to measure atmospheric reflectance (1.064 micrometers near infrared) to better understand the three-dimensional structure of the atmosphere, and to measure surface roughness at 100 meter scale. Elevation points were converted into both

gridded and spherical models to compensate for the topography of Mars, resulting in vertical and horizontal accuracies of ±1 m. MOLA measures the overall time it takes for a laser pulse to reach its intended target, whether it be the Martian surface or atmospheric layers, and return to the spacecraft. MOLA points are collected at an interval of 300 m along their tracks and separated from other tracks by 4 km. The resolution of MOLA reaches its finest detail at 37.5 cm on smooth surfaces but can drastically increase to as much as 10 m on rough slopes (Smith et al., 2001).

A data set was created using MOLA tracks that transect Siloe Patera and its surrounding area (Figure 22), generating ~ 150,000 MOLA points containing elevation, latitude and longitude coordinates as well as orbital information. Points were collected from the MOLA PEDR Query website between33.16 to 36.49 N and 6.23 to 8.9 E. Coordinates were selected on the basis of covering the region of Siloe Patera to gather

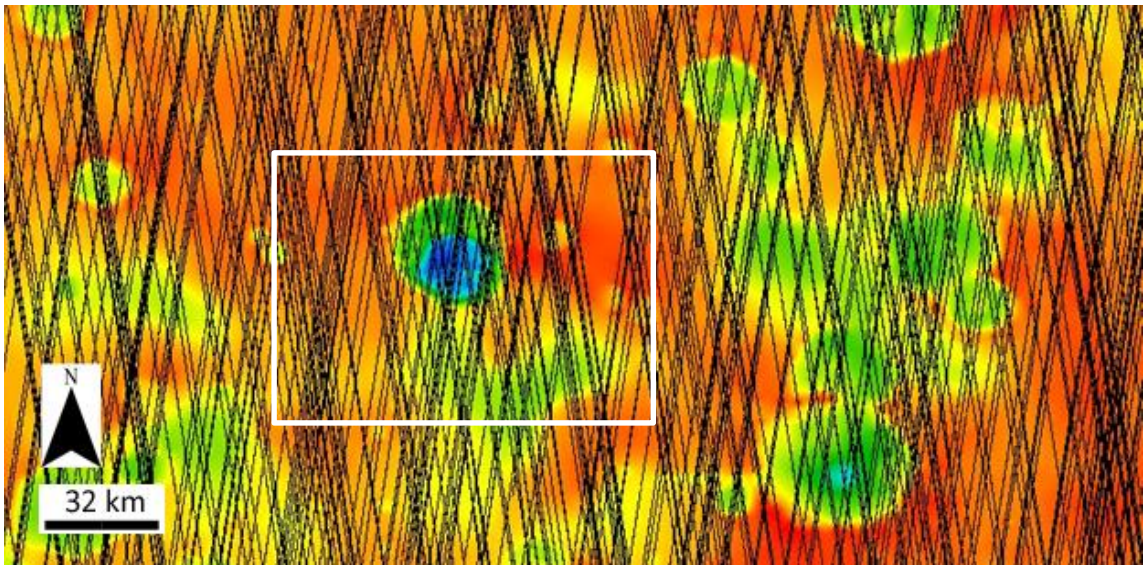

Figure 22: Good coverage of MOLA tracks along Siloe Patera provides sufficient data to analyze topography of the area. Siloe shown in box. Image rendered using ArcGIS, topographic map of Mars, and MOLA tracks downloaded from the USGS Planetary GIS Web Server (PIGWAD).

as much data as possible. MOLA tracks were also collected of Ascraeus Mon's caldera, generating 30,500 MOLA points in the region of 11.9 to 10.26 N and 255.8 to 256.0 W, and a random impact crater, dubbed Crater A, resulting in 78,600 MOLA points covering 24.25 to 24.25 N and 342.2 to 343.13 W. Like that of Siloe Patera, tracks were chosen based on their relevance to the region of interest and providing a sufficient amount of points to analyze. Using MOLA tracks, depth/diameter (d/D) ratios can be derived from typical impact craters and compared to Siloe Patera. Ratios d/D are calculated by the rim crest height and compared to the depth of the impact crater as measured by MOLA.

The High Resolution Imaging Science Experiment (HiRISE) camera has a 0.5 meter diameter primary mirror that can take images as large as 28 Gb (gigabytes) in as little as 6 seconds. Images display a detailed resolution at 0.25 to 1.3 m/pixel and can measure topographic changes to better than 25 cm of vertical displacement. HiRISE orbits at an altitude ranging from 255 - 320 km and has a minimum resolution of less than 30 cm/pixel at a distance of 200 km and a swath width of greater than 3 km from 200 km (McEwen et al., 2007). HiRISE has a ground tracking velocity of 3.2 km/sec which can cause difficulty when trying to take detailed images. In order to adjust for this issue, multiple images were taken, up to 128 times, and averaged to increase the signal-to-noise ratio, resulting in a detailed image. The top priority is to collect ~ 1000 stereo pairs which provide two overlapping images that can be manipulated to generate an elevation map as well as a 3D image (McEwen et al., 2007).The objective of this camera is to photograph ~ 1% of the Martian surface in the first 2 years of its Primary Science Phase (McEwen et al., 2007).

Through the HiRISE website, twelve suggestions were made for future imaging sites in and around Siloe Patera (Figure 23). Currently, only one request has been fulfilled (Figure 25) with an additional image of Siloe Patera not per my request. Requests from another research observing fluvial features, covers the remaining areas of Siloe Patera and was chosen for imaging (Figure 24). Image suggestions are rated by importance which can render many, if not all, suggestions on a low priority which may never be fulfilled. Table 1 shows a list of requested HiRISE image suggestions with image 82618 being the only one returned. Figures 24 and 25 show the HiRISE images taken for this project

The Context Camera (CTX) on board the Mars Reconnaissance Orbiter launched August 2005 and entered Mars's orbit March 2006. CTX has a great ability to obtain image at 30 km wide and 40 km long at a resolution of 5.0-6.5 m/pixel. Although this is a lower resolution than those taken by HiRISE, it has the ability to image the majority of the Martian surface with the most detail to date. This is a drastic improvement to Viking images with a resolution of 8-30 m/pixel (Malin et al., 2007).

As CTX image provided the most detail over the largest area, these images are the best choice for close observation. Nine CTX images were downloaded from Arizona State University's (ASU) Mars Image Explorer (Figures26, 27 and Table 2).

The Mars Orbiter Camera (MOC) was launched November of 1996 on the Mars Global Surveyor (MGS) and reached Martian orbit by September, 1997. One of MOC's greatest discoveries was that Mars has areas that are kilometers deep in layered material, suggesting massive erosion periods. MOC has four types of imaging: 1) global

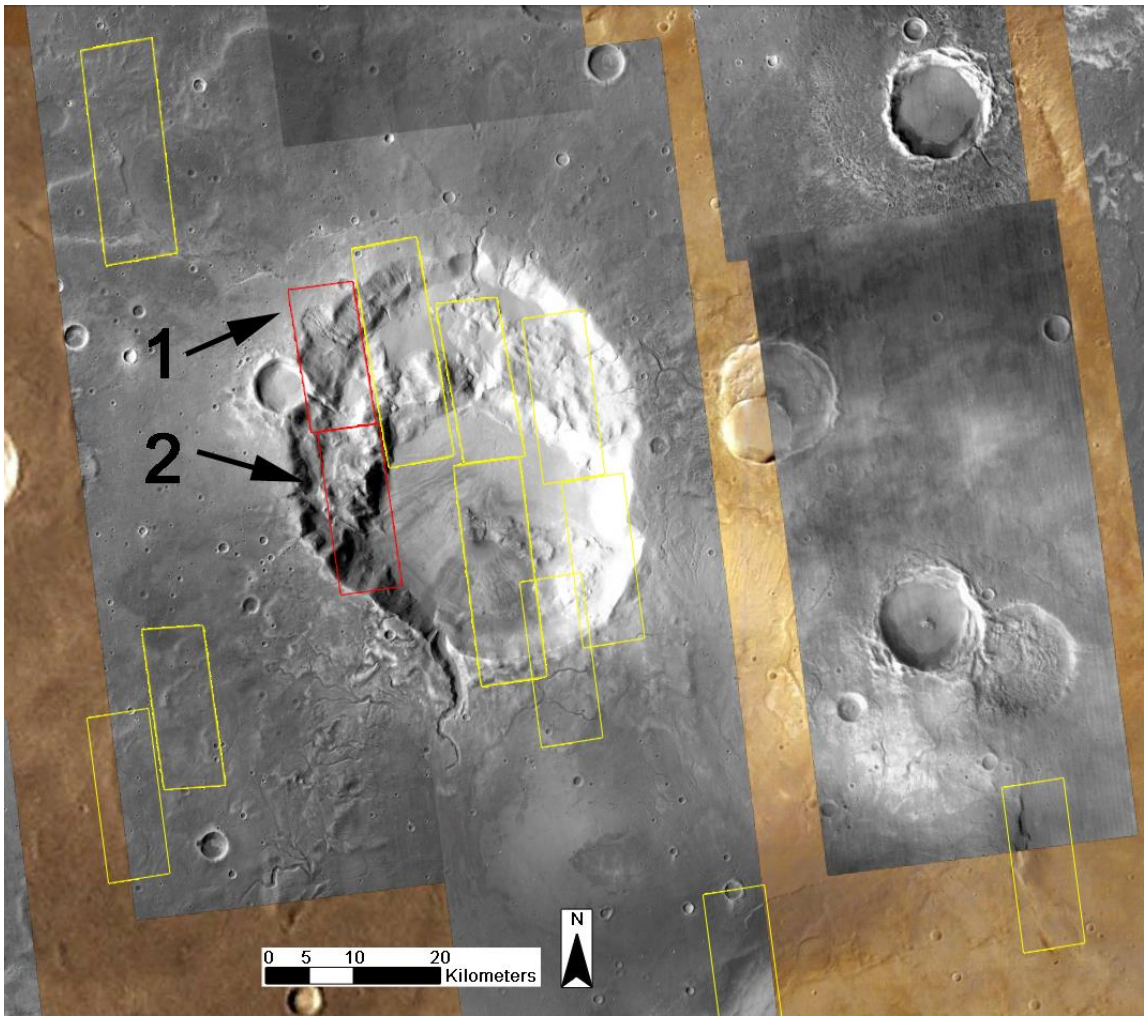

Figure 23: Image showing HiRISE requests. Yellow boxes indicate areas where red indicates the areas that have been photographed. Photographed images are designated as 1 (being the more northern of the two), and 2 (being the southern). The center of Siloe is located at 35° N and 6° E.

ID	Latitude	Longitude		ID	Latitude	Longitude
92040	35.398	6.746		84536	35.785	5.911
92018	34.538	7.674		84534	34.909	5.999
92014	34.785	5.89		82622	35.459	6.418
92012	34.942	6.729		82620	35.404	6.566
84792	34.493	7.092		82618	35.245	6.337
84538	35.109	6.609		82616	35.149	6.817

Table 1: HiRISE image suggestion list

possible thermokarst structures emanating from the wall. The brown strip in the middle is shown in true color.

distances, steep cliffs and a chaotic and eroded terrane. As in HiRISE image 1, the brown strip shows true color.

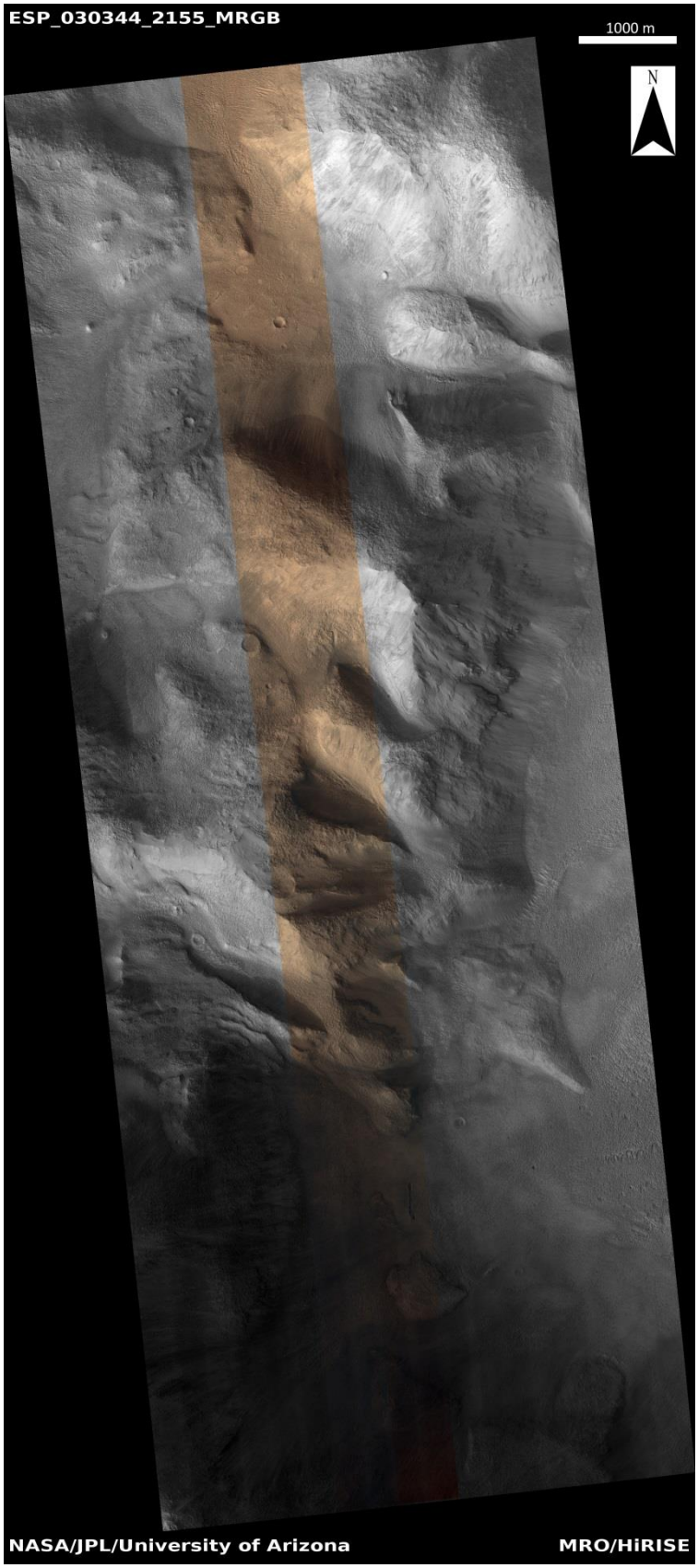

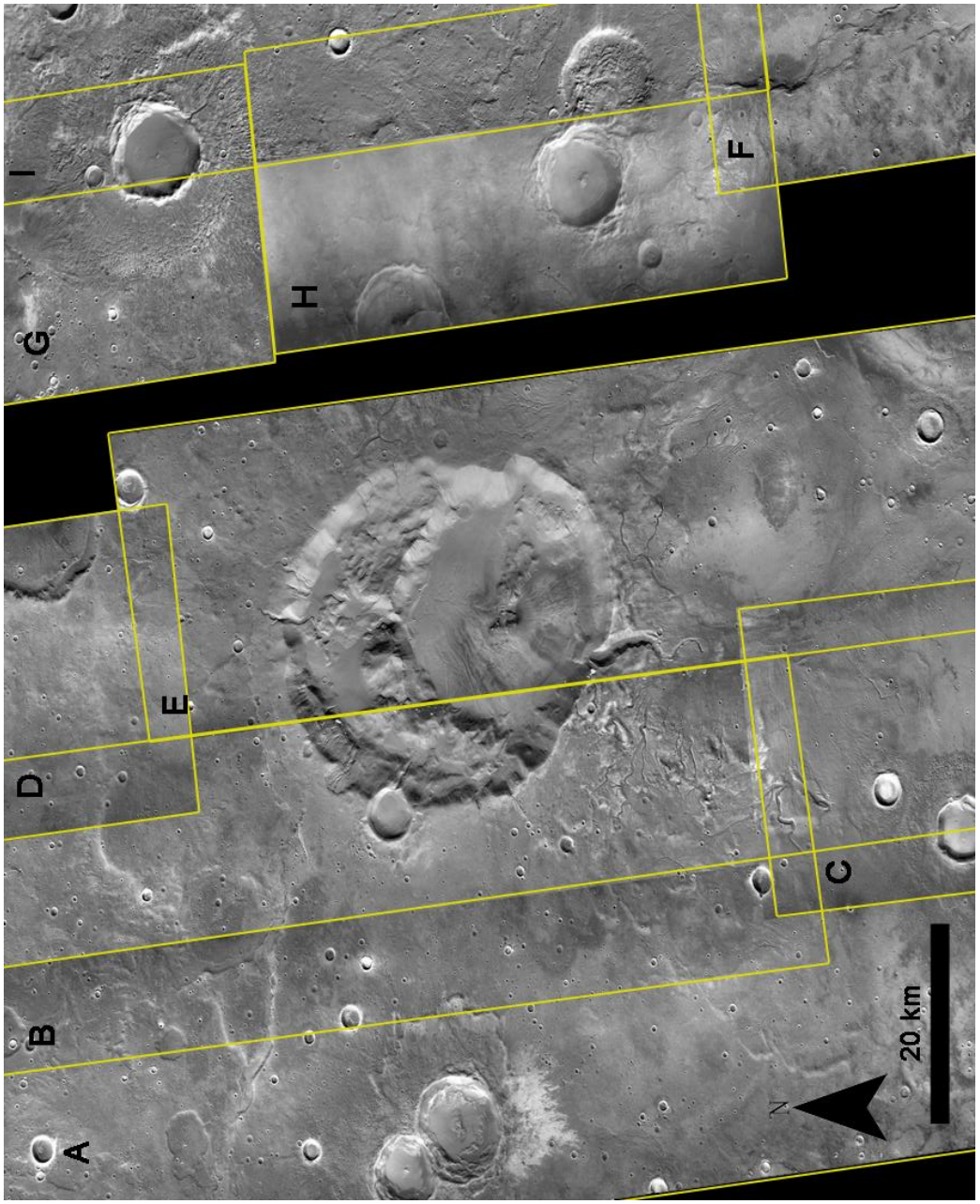

Figure 26: Position and location of CTX, MOC, and HiRISE images covering Siloe Patera. Letters are positioned in the top left corner of the image and some arrows point to the top left corner, followed by the letter as labeled in Table 1.

maps with 7.5 km/pixel resolution and swaths using red and blue wide-angle cameras for weather monitoring; 2) narrow-angle images with 1.5-12 m/pixel resolution to analyze geomorphology and geology; 3) context frames taken at wide-angle with 240 m/pixel, generally in red or blue; 4) wide-angle images ranging from 240-960 m/pixel

centered around monitoring regional areas (Malin and Edgett, 2001).Five MOC images were taken of Siloe Patera (table 1) labeled J – N (Figure 28 and 29).

	CTX Image Number	**Location**
A	B18_016828_2143_XI_34N354W	34.06°N 5.88°E
B	P21_009325_2160_XN_36N354W	35.72°N 6.04°E
C	G21_026388_2133_XN_33N353W	33.08°N 6.48°E
D	B19_017184_2187_XI_38N353W	38.41°N 6.11°E
E	B01_009892_2148_XI_34N353W	34.51°N 6.82°E
F	B19_016973_2136_XN_33N352W	33.39°N 7.91°E
G	P14_006464_2163_XI_36N352W	36.00°N 7.31°E
H	B07_012516_2154_XN_35N352W	35.17°N 7.47°E
I	D05_029355_2163_XN_36N352W	36.06°N 7.63°E
	MOC Image Number	
J	E18/00445	35.06°N 6.51°E
K	M23/01285	35.31°N 6.53°E
L	S14/02434	35.19°N 6.64°E
M	E11/00223	35.31°N 6.73°E
N	S15/02431	35.58°N 6.70°E
	HiRISE Image Number	
O	ESP_033258_2160	35.47°N 6.29°E
P	ESP_030344_2155	35.23°N 6.34°E

Table 2: CTX, MOC, and HiRISE Product Identification and location downloaded from Arizona State University's Mars Image Explorer. Images and locations are displayed in Figure 12. Letters are positioned in the top left corner of all images

Figure 27: Ind… th… …number and loca…
Table 2. Conti… …e pages.

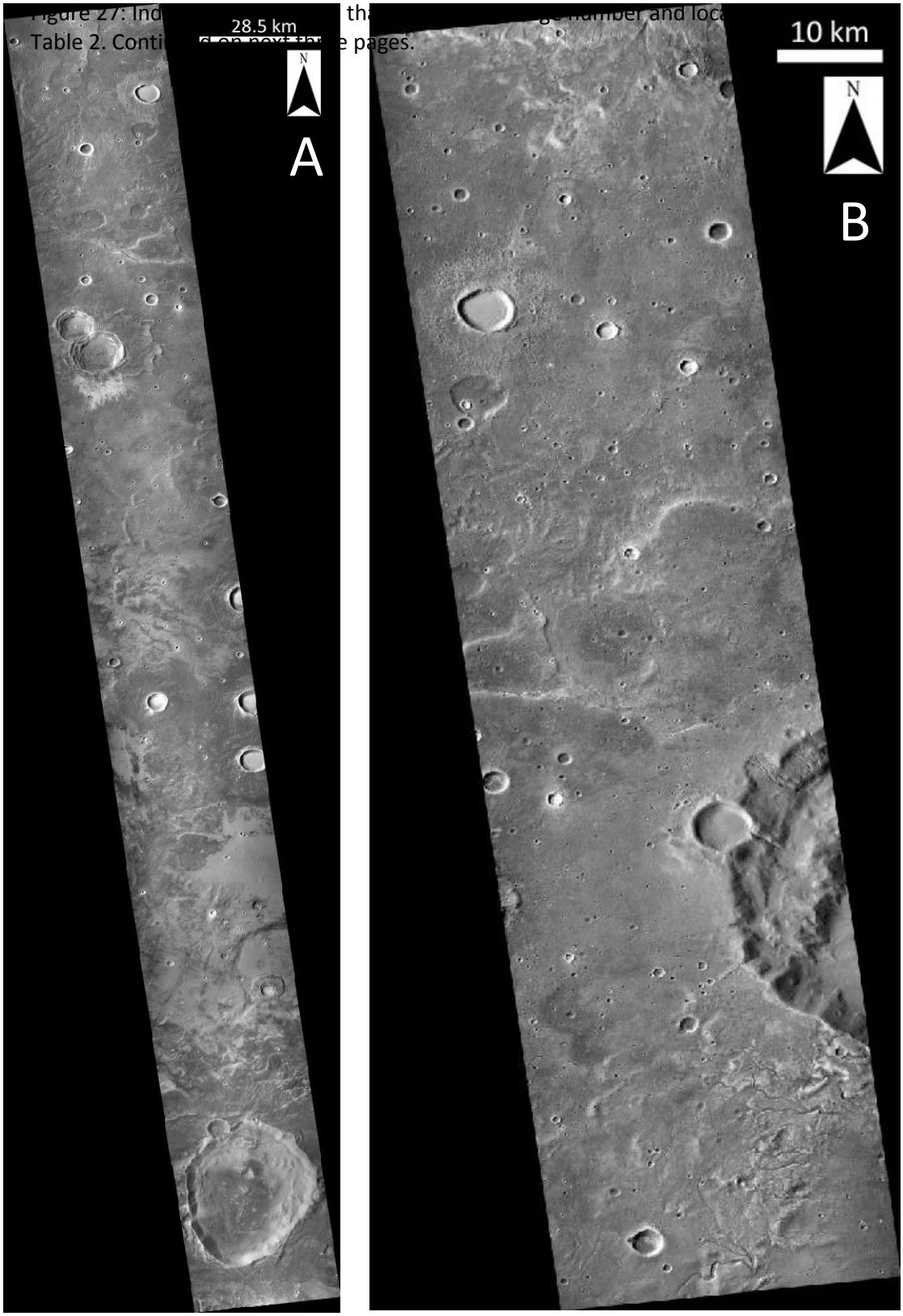

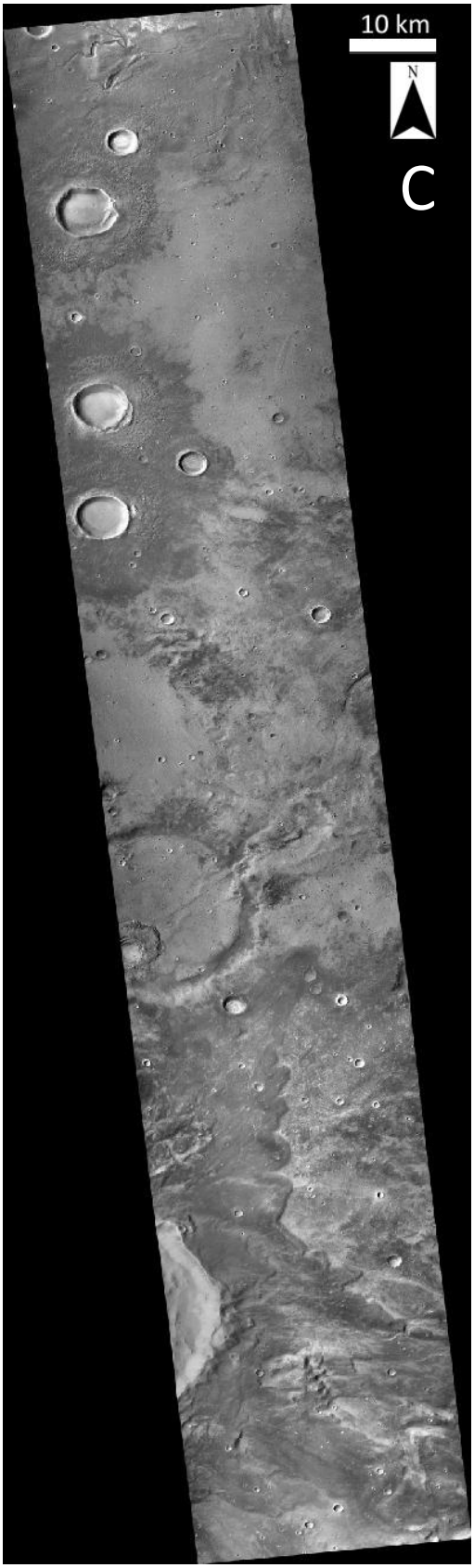
10 km
N
C


30 km
N
D

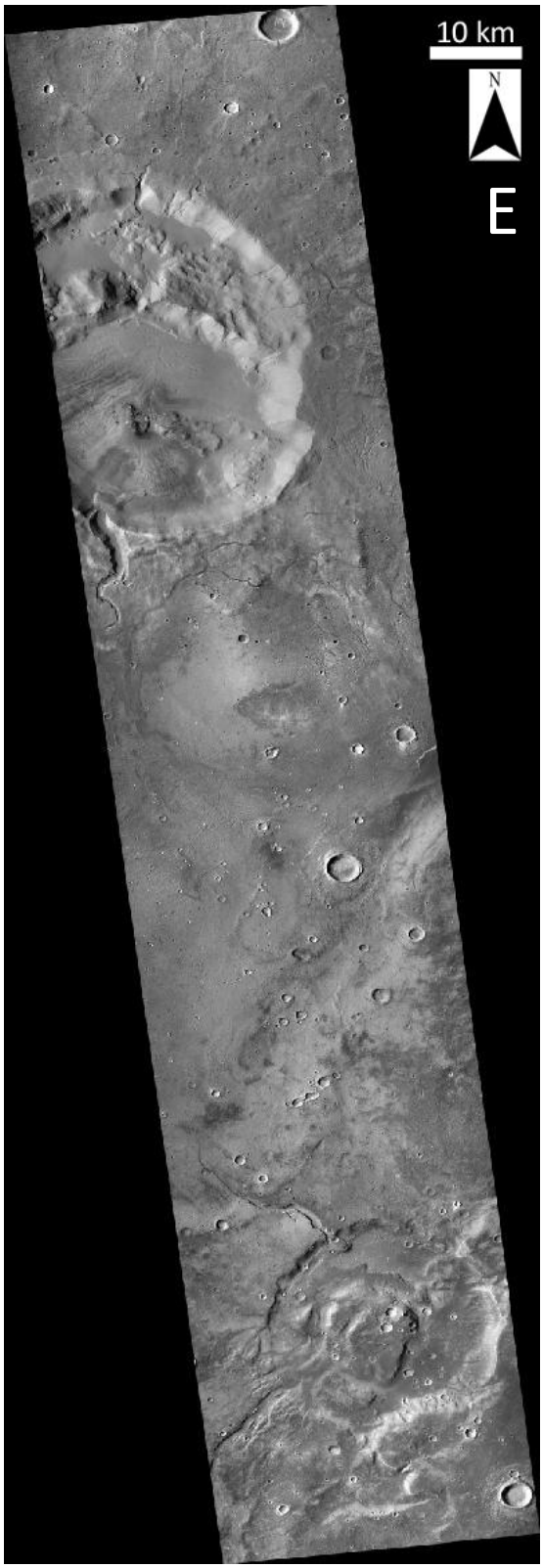
10 km
N
E


10 km
N
F

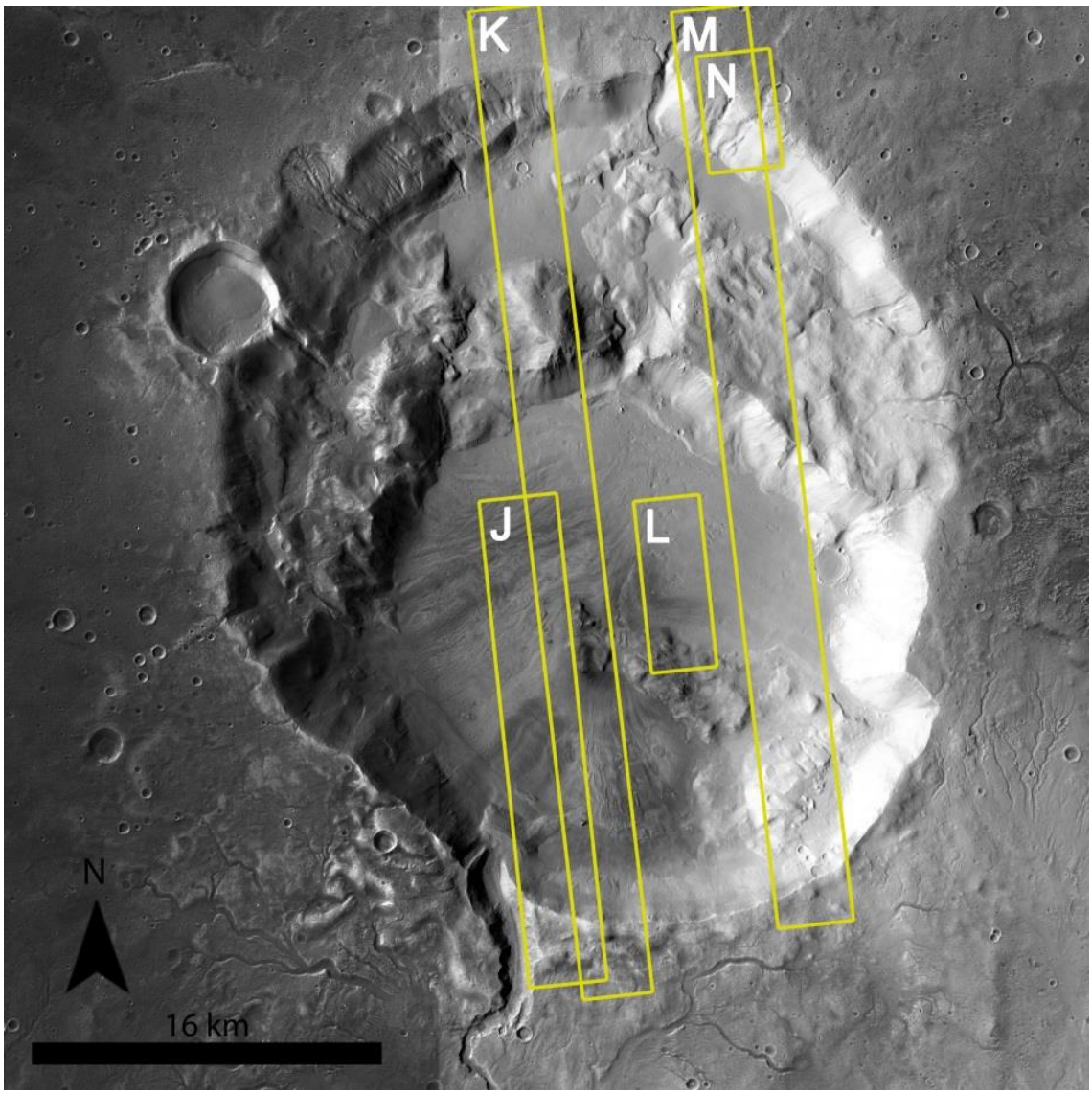

Figure 28: Map of MOC images used. Image number and location can be found in Table 2.

THEMIS is on board the 2001 Mars Odyssey mission with intent to investigate the surface mineralogy using multi-spectral thermal-infrared images. These images contain nine wavelengths with a concentration of 6.8 to 14.0 μm, and five bands in the visible/near infrared centered from 0.42 to 0.86 μm. The goal of THEMIS is to map Mars entirely in both day and night multi-spectral infrared images with a resolution of 100-m

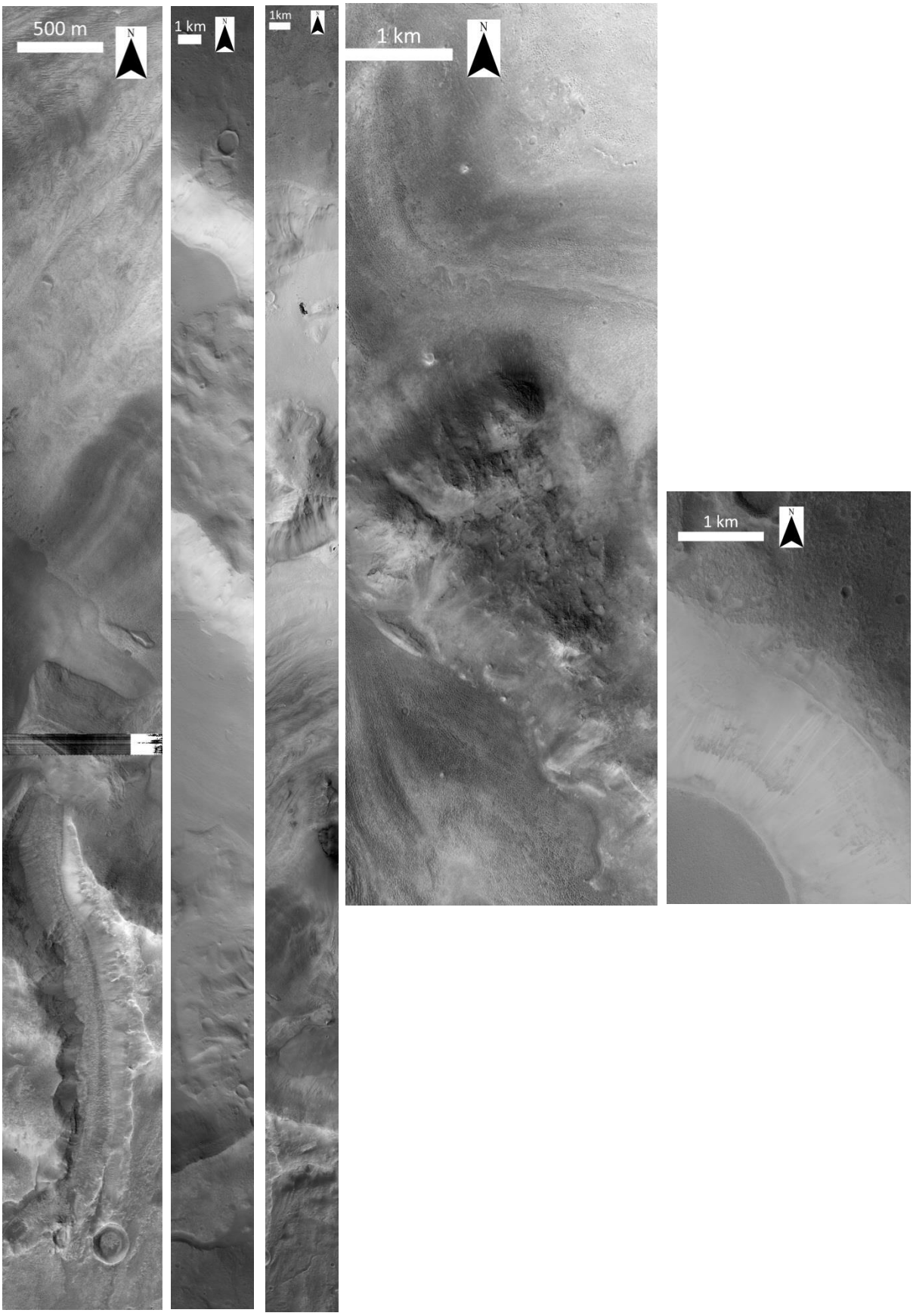
500 m
N
1 km
N
1km
N
1 km
N
1 km
N

per pixel. The two primary objectives of THEMIS are to resolve surface features at scales less than 100 m, and to identify minerals and compositional units at 100 m spatial scales (Christensen et al., 2004). THEMIS Day IR casts shadows and can increase visibility to raised areas such as the flow feature to the southwest of Siloe Patera. However, due to shadows, it can create discrepancies with thermal inertia of various rocks. THEMIS Night IR does not maintain the effects of shadows and will display solid rock as white and dust/sand as black (Figure 30).

In order to generate a rough geologic map of Siloe Patera, Erdas Imagine must be used to classify different land covers. There are two primary methods to classify an image; supervised and unsupervised. In a supervised classification, classes are generated from training samples designated by the user. Unsupervised classifications are generated by the computer and can later be adjusted by the user to determine what land cover each class is. For this paper, unsupervised classification was used with THEMIS Night IR, MOLA, and CTX images. The unsupervised classification used was generated by the ISODATA clustering algorithm. This algorithm assigns an arbitrary initial cluster center where each pixel is classified to a center that is closest. In the next step, different cluster centers are chosen and each pixel is again classified to a cluster center. This process is done until there is little change between the iterations (Omran et al., 2002).

CHAPTER 4

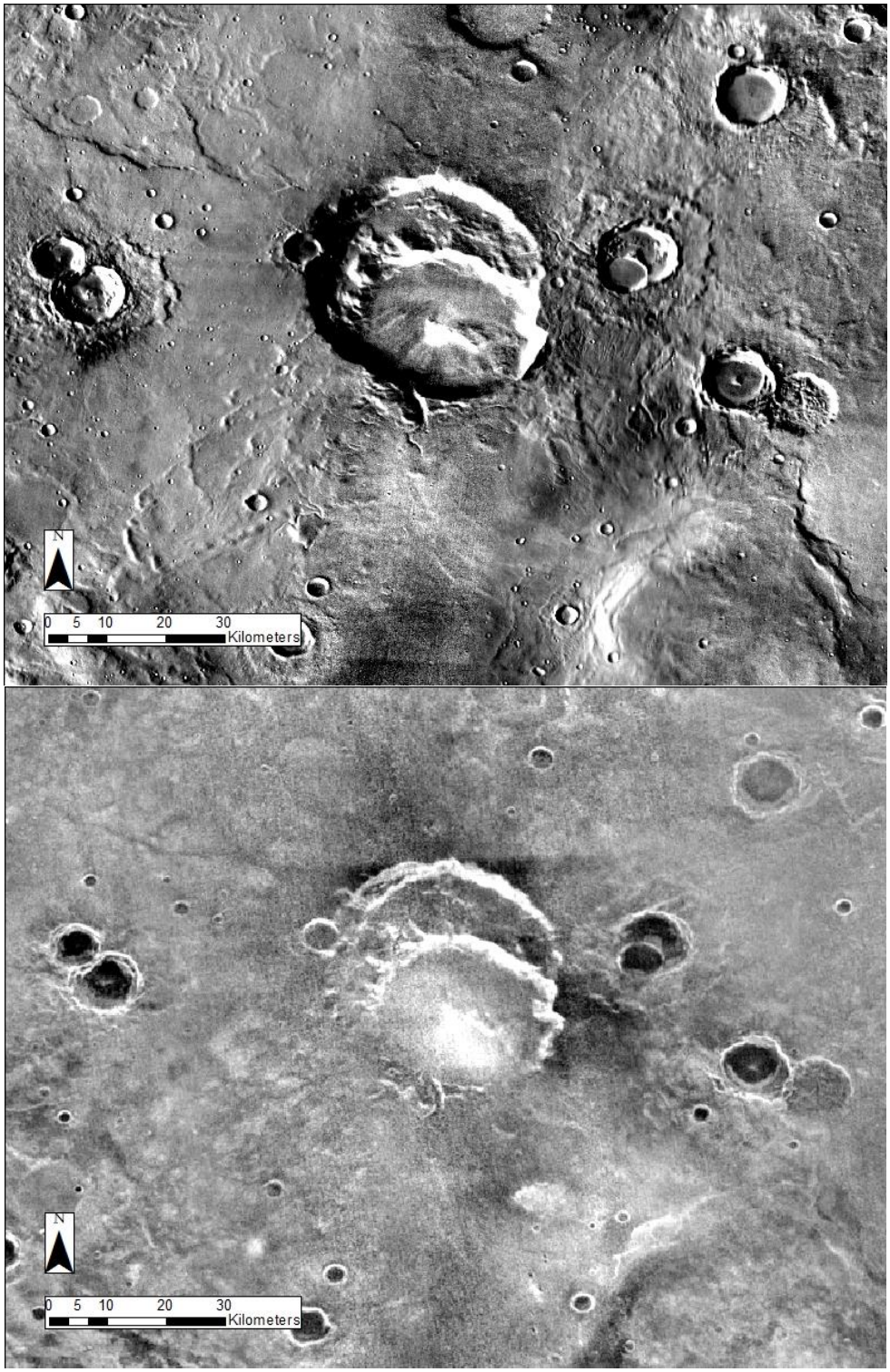

Figure 30: Siloe Patera shown in THEMIS Day IR (top) and THEMIS Night IR (bottom).

A clip of THEMIS Night IR, MOLA map set to 20 classes, and multiple CTX images mosaicked together, were used to generate a geologic map of Siloe Patera in Erdas Imagine. The THEMIS Night IR clip was cut from the global THEMIS Night IR map provided by the U.S.G.S Planetary GIS Web Server (PIGWAD) website. The MOLA map was rendered using MOLA track points that were previously collected and were placed into 20 classes at equal intervals based on elevation. Multiple MOLA maps were created for this project and classes ranged from 20 to 250 but fewer classes helped pull out more features, so 20 classes were used in the final render. Unfortunately, there is no global CTX mosaic image, so each individual CTX image had to be mosaicked by hand. Images were easily georeferenced in ArcGIS, but were not easily mosaicked. Each CTX image is surrounded by a black border that compensates for the image's projection that necessitated removal in Adobe Photoshop before all images could be mosaicked together. Once the CTX images were mosaicked and imported into ArcGIS, they were georeferenced to the THEMIS Night IR and MOLA images.

To minimize file size, the THEMIS Night IR clip, MOLA, and CTX mosaic images were all set to 300 dpi with a width of 3300 pixels and a height of 2500 pixels and exported from ArcGIS. Erdas Imagine 2011 was used to combine these three images into one using the Layer Stack tool. THEMIS Night IR was imported onto band 1, MOLA was imported onto band 2, and CTX mosaic was set to band 3. Once rendered and opened, the image is displayed as a color stretch with green representing rockier regions and red indicating very dusty areas (Figure 31).

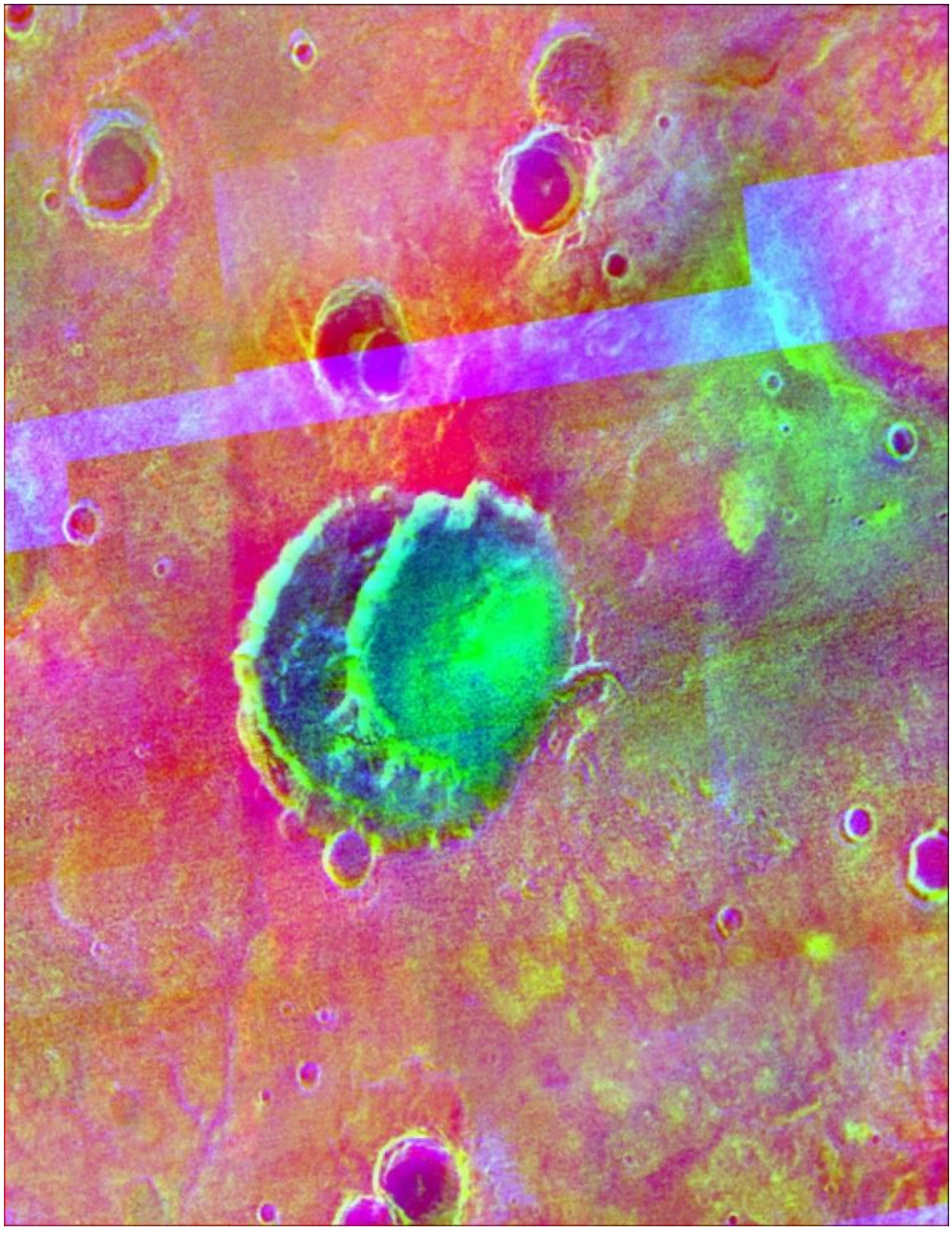

Figure 31: Color stretch of Siloe Patera with THEMIS Night IR, MOLA, and CTX mosaic images combined into one image with each representing an individual band. Red represents less reflective surfaces, suggesting high dust coverage and green shows areas with hard rock ad are more reflective at night due to insolation absorption during the day.

An unsupervised classification of the color stretch image was generated to produce a geologic map. Twenty classes were chosen and each class was analyzed by color to determine into which land class it fell(Figure 32, Table 3). Three land types were used in this classification Table 3): (1). Dust (tan); (2) Rock (brown); (3) Sediment fill-in

(turquoise). These land types were chosen because they are the most important land cover types needed to create a geologic map for this research. Siloe Patera shows hard rock in the scarps and a mainly hard rock floor with areas of sediment fill-in on the floor and bench. It is not characteristic for a flat-floored impact crater to have rock exposed in areas other than the central peak. The brown line across Figure 32 is the result of a gap in between CTX images and should be ignored.

Combining the color stretch image, classified image, CTX, and THEMIS Night IR images, a rough geologic map was rendered (Figure 33), similar to that of Mailam, et al.(2003) and Martinez-Alonso et al, (2005) (Figure 31). This map was categorized into nine different units/features and each was chosen to best represent a region based on all images. Solid rock is exposed in much of Siloe Patera and contains small amounts of dust located on the east side of the bench. Unit 1 fill-in and Unit 2 Fill-in are represented as one unit in the classification map but under further review of CTX images, were divided into two units. Unit 1 fill-in represents areas that appear to be older and have had time to slightly alter or erode. Unit 2 fill-in is found in low lying flat areas that are likely the result of younger runoff deposition according to its stratigraphic position. Post-volcanic doming regions show up as solid rock in in low lying flat areas that are likely the result of runoff deposition and must be younger according to its stratigraphic position. Post-volcanic doming regions show up as solid rock in the classification map as well as in the stretched color map, while the spire shows up as one of the brightest areas in THEMIS Night IR and in the stretched color map.

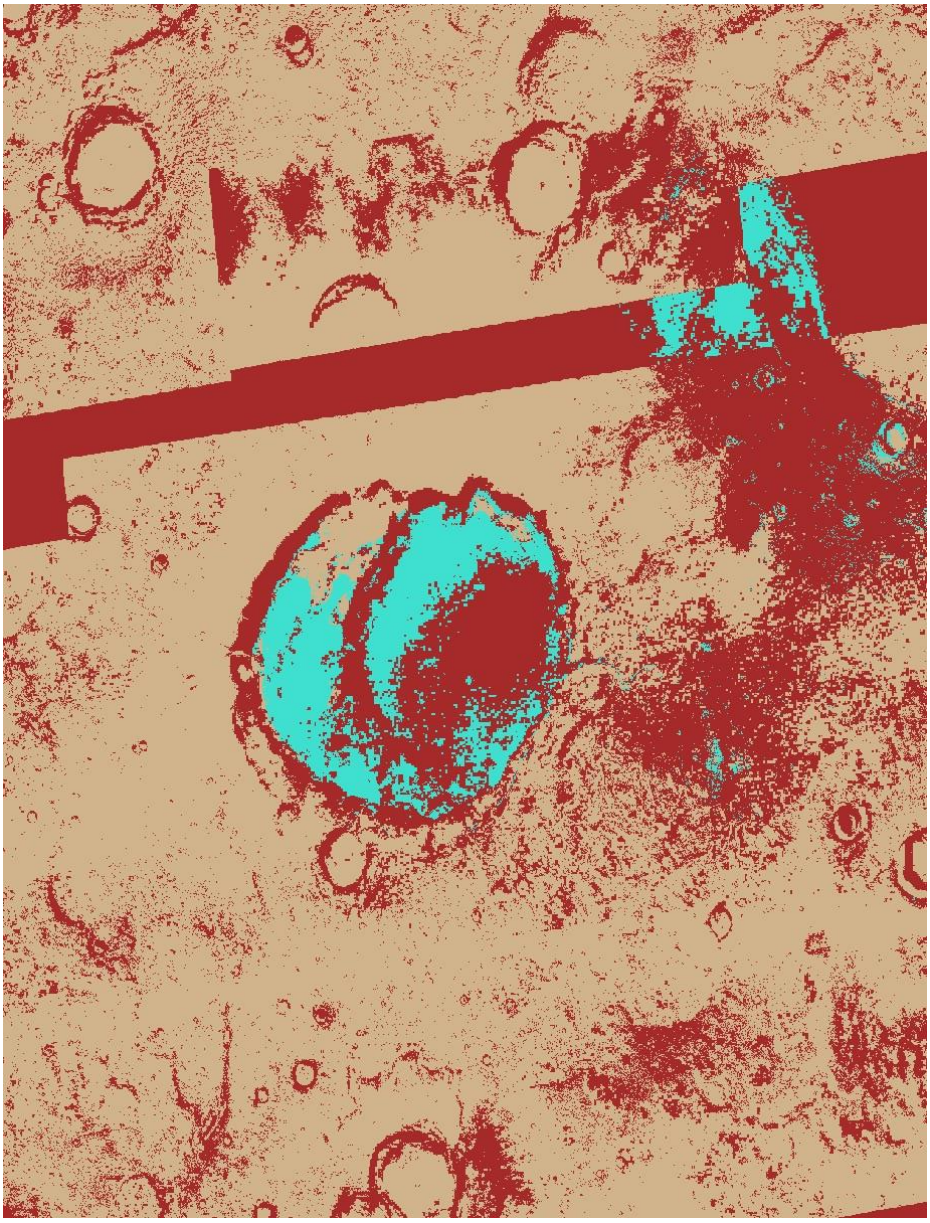

Figure 32: Geologic map of Siloe Patera showing areas of dust (tan), rock (brown), and sediment fill-in (turquoise). Figure was rendered using THEMIS Night IR, MOLA, and CTX mosaic images to produce an unsupervised classification of 20 classes.

Color	Red	Green	Blue	Class	Land Type
Tan	0.823529	0.705882	0.54902	Class 1	Dust
Turquoise	0.25098	0.878431	0.815686	Class 2	Fill-in
Brown	0.647059	0.164706	0.164706	Class 6	Rock

Table 3: List of three classes and land cover types used to produce classification map in Erdas Imagine (Figure 24).

The geographic coordinate system used was the GCS_Mars_2000_Sphere and the projection was Equidistant Cylindrical with map units in kilometers. MOLA data was collected from MOLA PEDR Query website and points ranged from 36.5 – 33.0 N and 4.0 – 9.0 E for Siloe Patera, 10.0 – 11.0 N and 103.0 – 105.0 W for Ascraeus Mons, and 24.0 – 26.0 N and 17.45 – 16.0 W for Crater A. These points were downloaded and imported to Excel where columns were formatted for importing into ArcGIS. Once imported into ArcGIS, XY data was displayed and exported into a shape file in order to be manipulated. Once MOLA points were in shapefile format, they were used to produce interpolated maps that fill in areas with no data. The Inverse Distance Weighted (IDW) function was used to produce elevation map. The IDW method allows points in proximity of the processing cell to have a weighted influence determined by its distance from the processing cell. Therefore, closer points are likely to have similar elevations than those points that are further away. This same process was done for Ascraeus Mons and Crater A, B, C, and F providing detailed elevation maps.

Once IDW maps were produced (Figure 34), contour maps were rendered at intervals of 5 meters. The 5 meter interval and a 100 meter interval were chosen to provide detail of the topography as well as a less detailed map that covers a greater area (Figure 35). Interpolated maps of MOLA points are necessary in order to generate contour values as they cannot be generated from MOLA points alone.

Once Siloe Patera, Ascraeus Mons and Crater A, B, C, and F were completed using IDW and resultant contour maps, Triangular Irregular Network (TIN) maps were

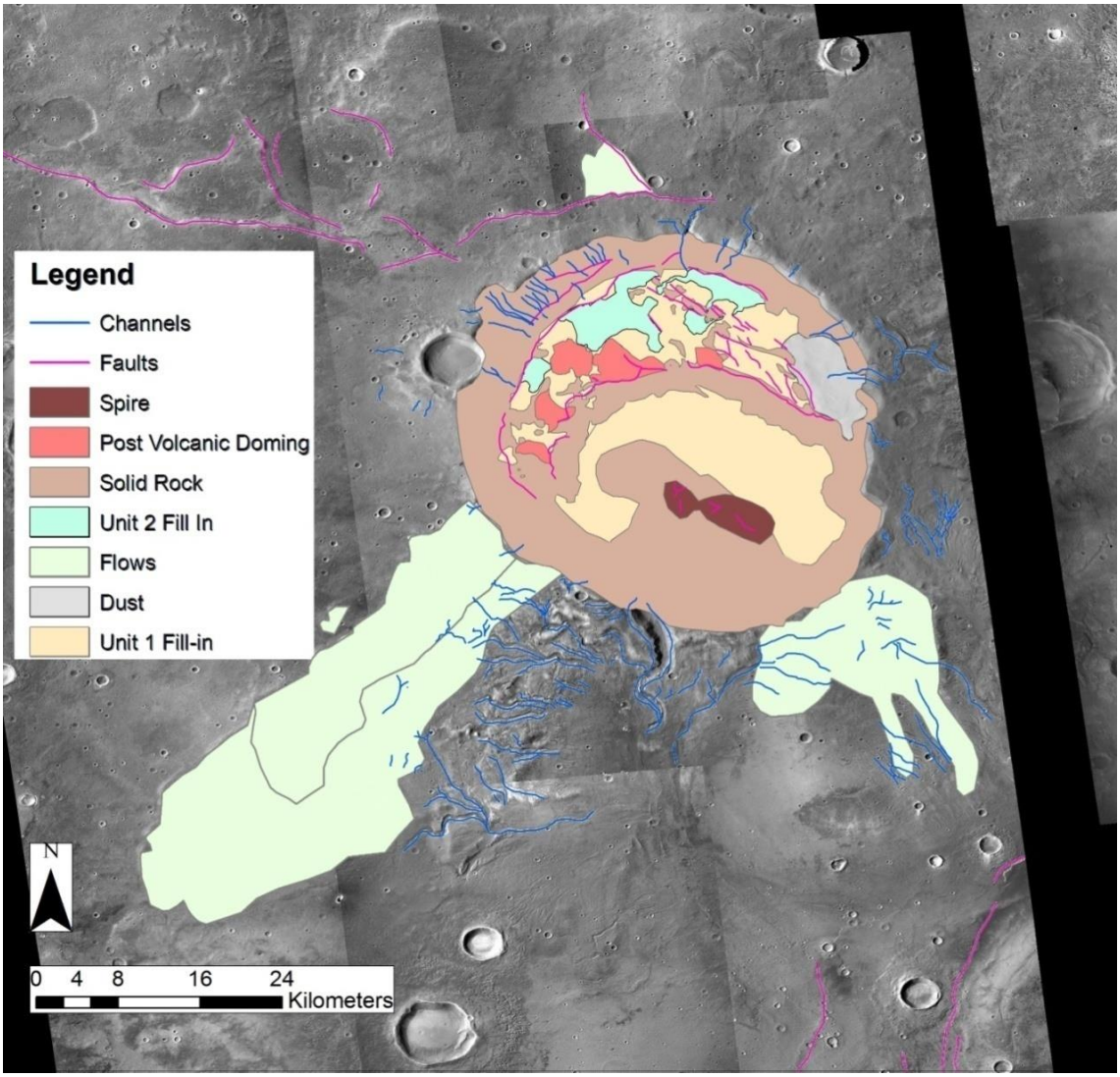

Figure 33: Geologic map of Siloe Patera rendered in ArcGIS and Adobe Photoshop using a color stretch map, classification map, THEMIS Night IR, and CTX images.

generated using the contour maps (Figure 36). TIN maps are essential for ArcGIS to represent the surface morphology of features, unlike the flat surfaces seen in the IDW and contour maps. Vertices are created and connected by a series of edges to produce a network of triangles. Once these TIN maps were produced they were imported into ArcScene to produce a 3D model. This 3D model was set to have a vertical exaggeration of 24x which helps to accentuate features of Siloe Patera that were not previously

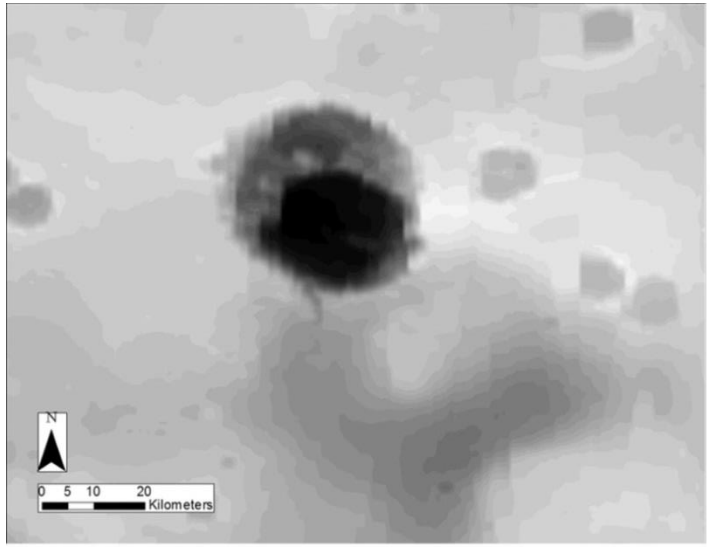

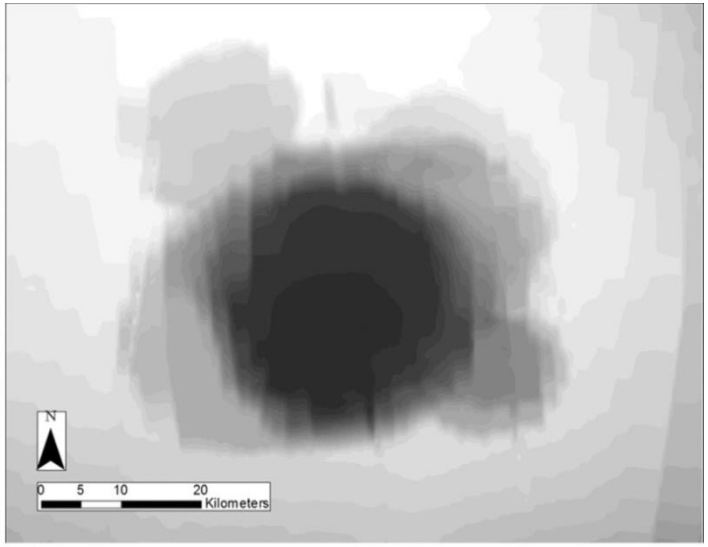

Figure 34: Images are rendered using ArcGIS's interpolation tool. Siloe (top left), Ascraeus Mons (top right), and Crater A (right) were all generated with 30 classes and set to a gray scale. All were generated using IDW from ArcGIS.

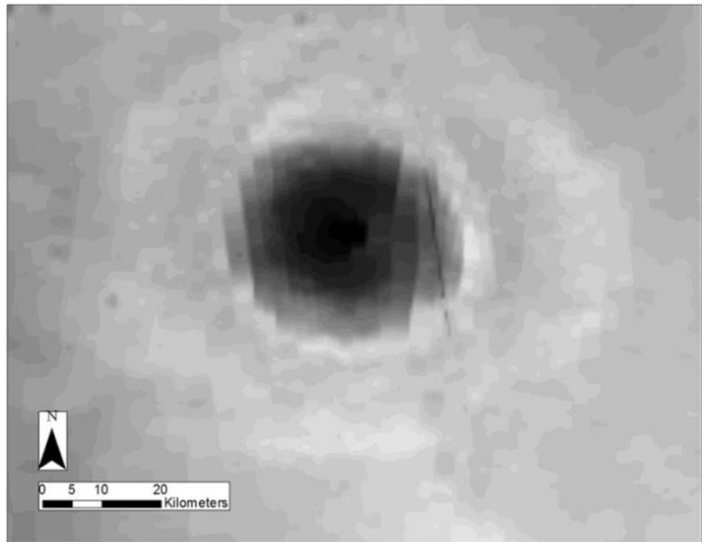

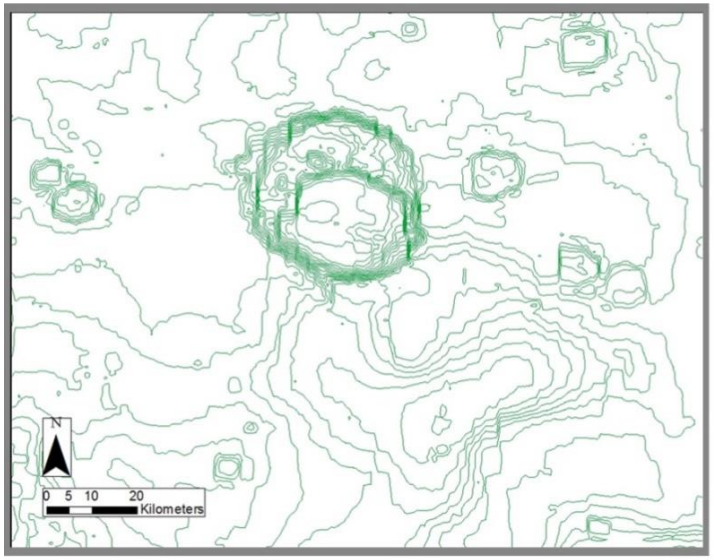

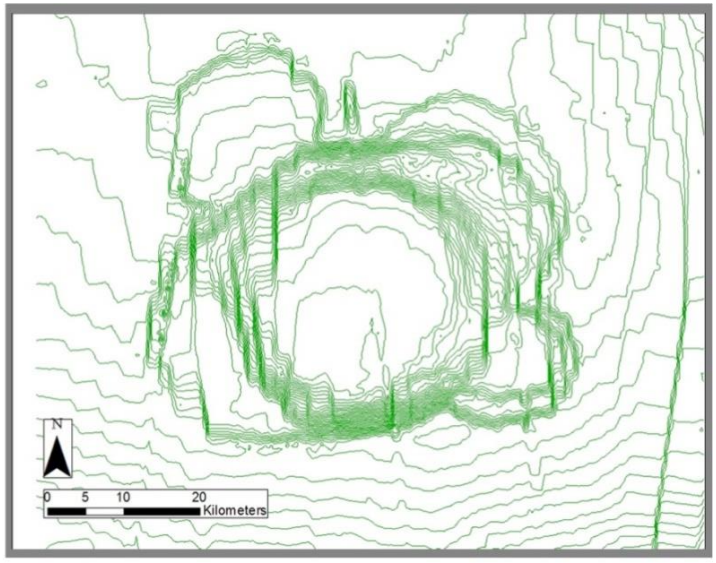

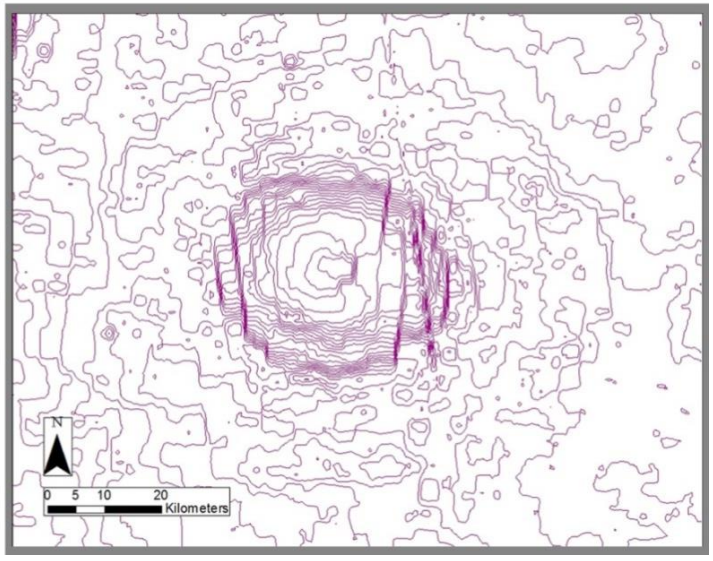

Figure 35: Siloe Patera (top left), Ascraeus Mons (top right), and Crater A (right) are displayed here in contour intervals of 100 meters. This was accomplished by ArcGIS through the use of the spatial analyst tool and imputing the IDW rendered layers and assigning a contour interval.

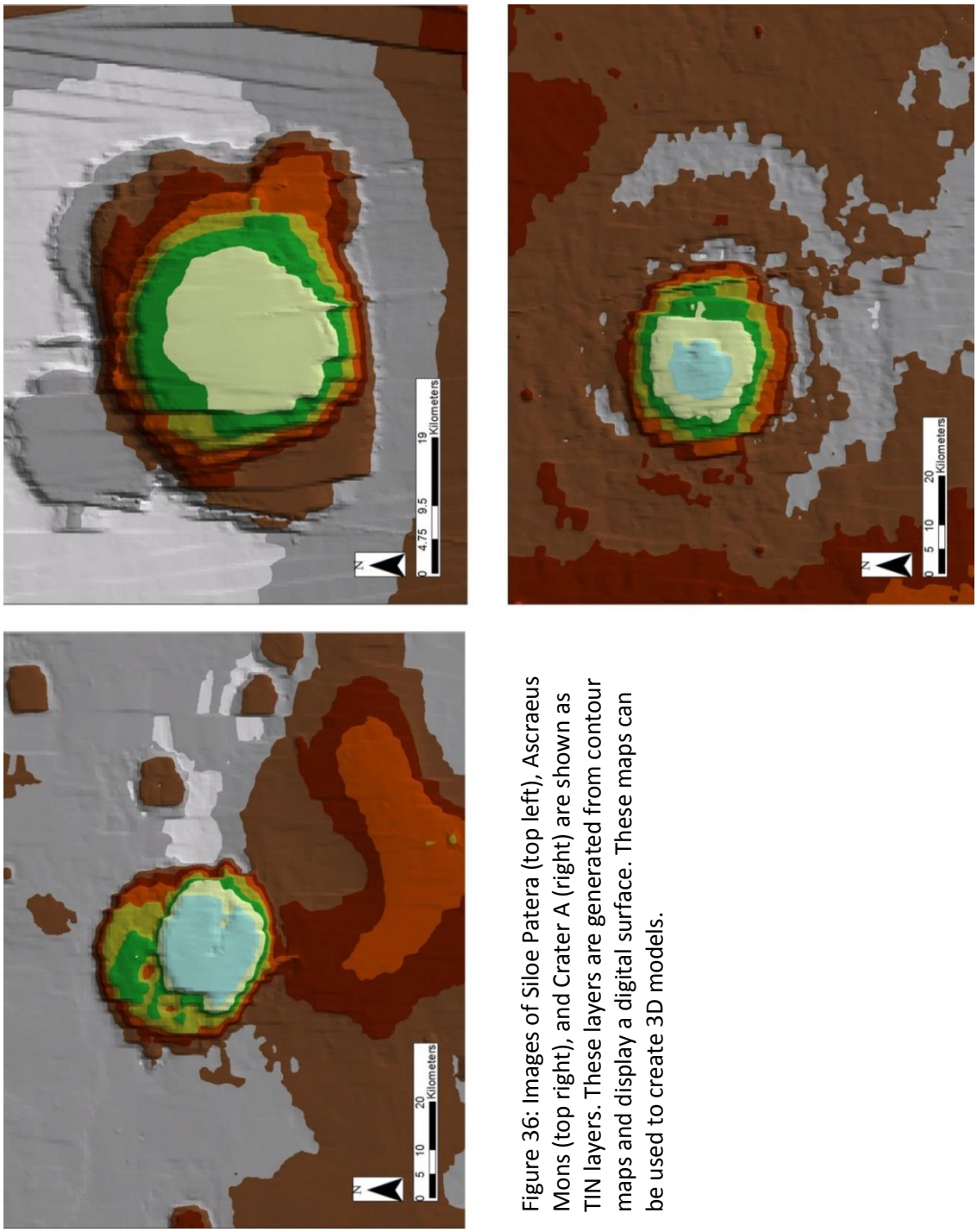

Figure 36: Images of Siloe Patera (top left), Ascraeus Mons (top right), and Crater A (right) are shown as TIN layers. These layers are generated from contour maps and display a digital surface. These maps can be used to create 3D models.

noticed in 2D images. Higher and lower numbers exaggerate the image to the point that it becomes unrecognizable. Once the 3D model was produced, CTX and THEMIS images

were draped on top. This required assigning each image a layer to be draped on which was achieved by viewing the properties, designate the CTX and THEMIS images as a float layer, and then assign the layer it would be draped over.

All CTX, HiRISE, MOC, and THEMIS images were georeferenced to THEMIS day global map downloaded from PIGWAD. For each image, at least 8 reference points were placed with an acceptable root mean square error of less than one. Images were downloaded with a standard black background that can be hidden.

Once TIN maps of Siloe Patera were created, they were imported to ArcScene where a 3D model was generated. This was done by importing a TIN map generated at five meter contour intervals in ArcGIS. Five meter contour intervals produced a detailed view of Siloe Patera without crashing the software due to excessive file size. Once the TIN map is imported, adjustments were made to that Siloe Patera could be accurately depicted. Due to Siloe Patera's vast diameter compared to its depth, vertical exaggeration provides a better view of its features that are not noticeable without vertical exaggeration.

Once the 3D model was generated, THEMIS and CTX images were overlain to help identify features and points of interest. Draping images was completed by selecting its properties, base height, and the layer over which it will be draped, which in our case was the TIN layer. This produces an interactive 3D model that displays north in the direction of the green arrow located in the top left corner (Figures 37 and 38). Scales for

Figure 37: Sloe Patera shown in a basic 3D color map (above) and in CTX (below). Volcanic domes are outlined hexagons, the spire is outlined by a rectangle, and the faulting region is circled by an ellipse.

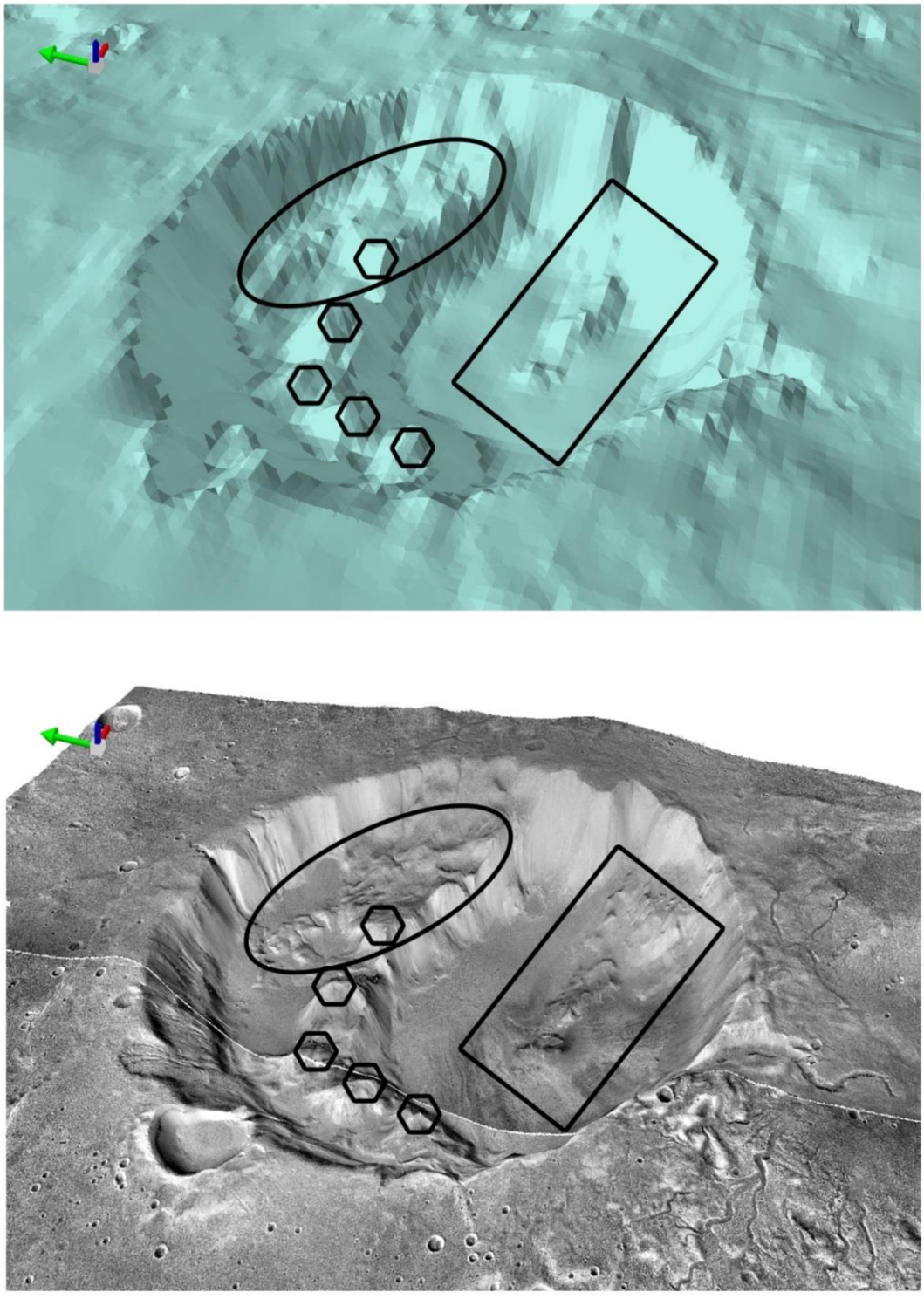

Figure 38: Siloe Patera shown in THEMIS Day IR (above) and in THEMIS Night IR (below). Volcanic domes are outlined by hexagons, the spire is outlined by a rectangle, and the faulting region is circled by an ellipse.

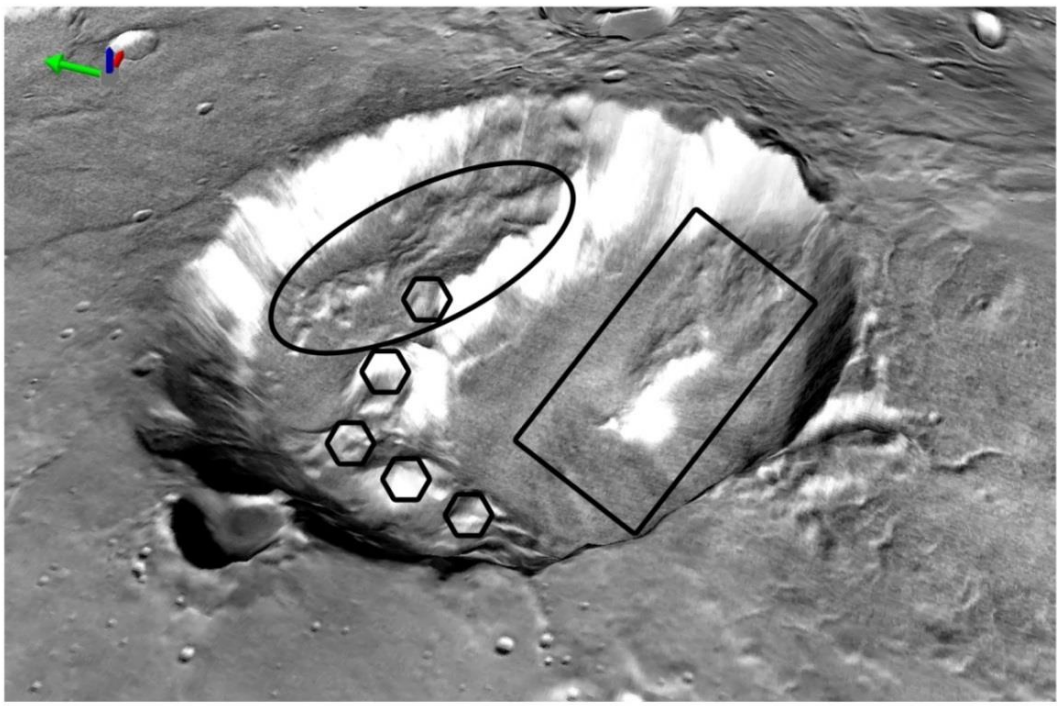

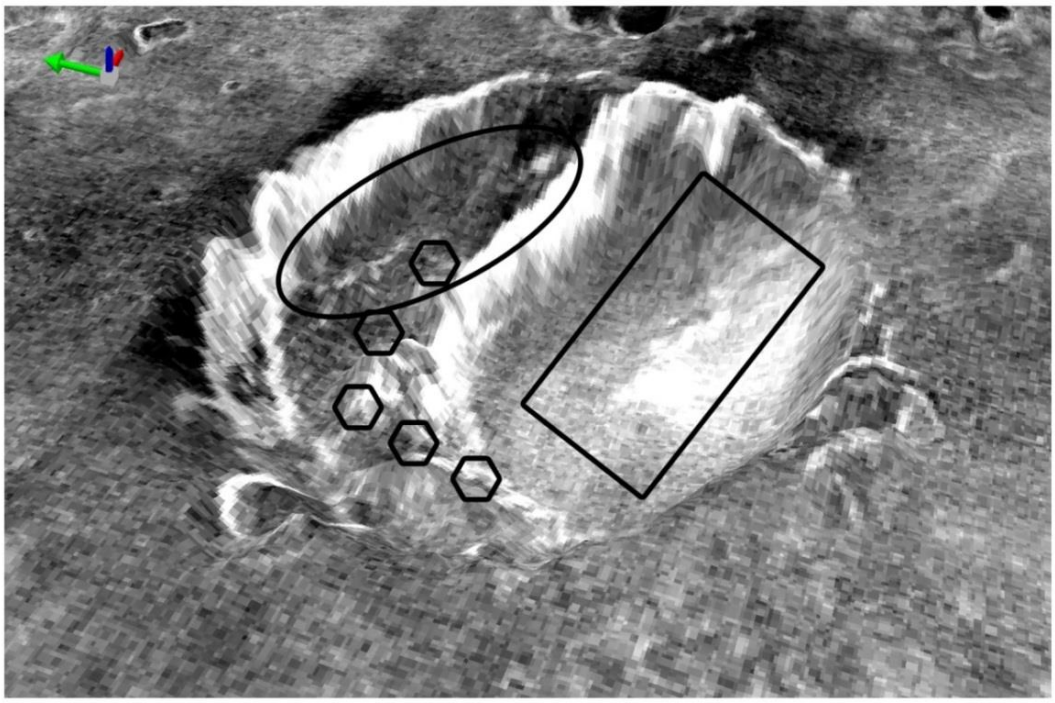

the 3D model images are not displayed because scale is not continuous when viewing Siloe Patera at different angles.

When viewing Siloe Patera in 3D, new features stand out where they did not when viewed as a 2D image. These features include multiple peaks along the scarp inside Siloe Patera, possible ring faulting along the north eastern portion of the bench, and a feature “spire” which emanates from the eastern wall of Siloe Patera and runs to the center of Crater B’s floor (Figure 3B). These features are evident in, CTX, and THEMIS day and night 3D images. Features are outlined in plain and CTX 3D models.

There are multiple regions in Siloe Patera which may provide insights into its origin, including multiple raised mounds along the scarp line of the bench, faulting along the north eastern portion of Crater A’s bench, flow features, a large depression to the south and an elongated mound on the floor of Crater B referred to here as a spire.

The raised mounds along the fault scarp dividing Crater A from Crater B show clear isolated peaks in MOLA data and are divided by channels. These five mounds appear to be solid crystalline rock that was formed by volcanic eruptions and not the result of sediment accumulation. Each one ranges in height and shape and appear bright in the classification map and THEMIS Night IR indicating exposed rock (Figures 31 and 32). These mounds, however, are not as bright as the spire on the floor of Crater B and could be covered by layers of dust or ash.

Along the right side of the bench of Crater A is a series of concentric exposures that appear to be ring faults (Figure 3B). These faults run from the edge of the fault scarp, toward the northern rim of Siloe Patera, slightly curving to the northwest. These

faults are degraded and likely covered by layers of dust or ash, leaving little room for rock exposure. The classification map and THEMIS Night IR, however, suggest minor exposures of rock along some of the faults (Figures 31 and 32).

Three flow features (Figure 43) propagate form the north, southeast, and southwest regions of Siloe Patera. They vary in length with the southwest flow being the longest, southeast flow much shorter and north flow slightly shorter than the southeast (Table 6). Classification maps and THEMIS Night IR show areas of rock and dust throughout the flows but the head of the flows appear brighter than the surrounding area (Figures 23 and 24). The southwestern flow also shows an overlap of lobes indicating at least two flow events created this feature (Figure 43).

To the south of Crater B's southern rim is a large area of subsidence, likely once a lake due to a high number of stream channels that flowed into it. The eastern-most region is the shallowest and shows up with high thermal inertia in THEMIS Night IR and in the classification map (Figures 31 and 32). The high thermal inertia is likely exposed evaporate or mud deposits from the probable lake.

The spire located on the floor of Crater B is broken into two parts with one isolated mound and an elongate mound. They extend and grade up in elevation until they connect to the southeastern wall of Siloe Patera. MOLA data shows that it is higher than the surrounding floor with elevations that rise toward the rim. It appears to be a primary igneous feature, possibly an eroded cone or dike, rather than a clastic sedimentary deposit. The classification map, as well as the THEMIS Night IR map, shows the spire and surrounding area to be one of the brightest regions on the map (Figures 31

and 32). This means the area has high thermal inertia generated from crystalline rock and is not likely to be a loosely consolidated sedimentary rock.

Topographic profiles of Siloe Patera, Ascraeus Mons, and Crater A, B, C, and F (Figure 39) are essential for determining the true elevation of each feature and their internal morphology. These profiles are produced in ArcGIS after TIN maps are created of the areas of interest. Using the 3D analyst interpolate line tool, lines are drawn to intersect Siloe Patera, Ascraeus Mons, and Craters A to provide a topographic profile of each. Lines were drawn at an approximate distance of 60,000 meters to maintain similar profile length for comparison.

To compare topographic profiles, all data are was and imported into Excel with X, Y, and Z coordinates. Elevation and distance are reported in meters, but to simplify distance variables were converted into kilometers. Elevation is displayed in relation to the feature's true elevation on Mars and not normalized to zero. This created difficulty when comparing profiles as they would not plot over one another but instead above or below. To correct this problem, elevation data was normalized such that all features begin at zero distance and zero elevation. All graphs were overlain in order to facilitate comparison (Figure 31 and 32).

Topographic profile comparison of Siloe Patera, Ascraeus Mons, Crater A, B, C and F(Figure 40) shows that Siloe Patera resembles the profile of Ascraeus Mons more than Craters A, B, C and F. This is shown by its arcuate scarped walls and steep slope angle, unlike the more shallowly sloped wall angles and non-arcuate scarps of the impact craters. Siloe Patera also lacks a raised rim and no central morphology, like

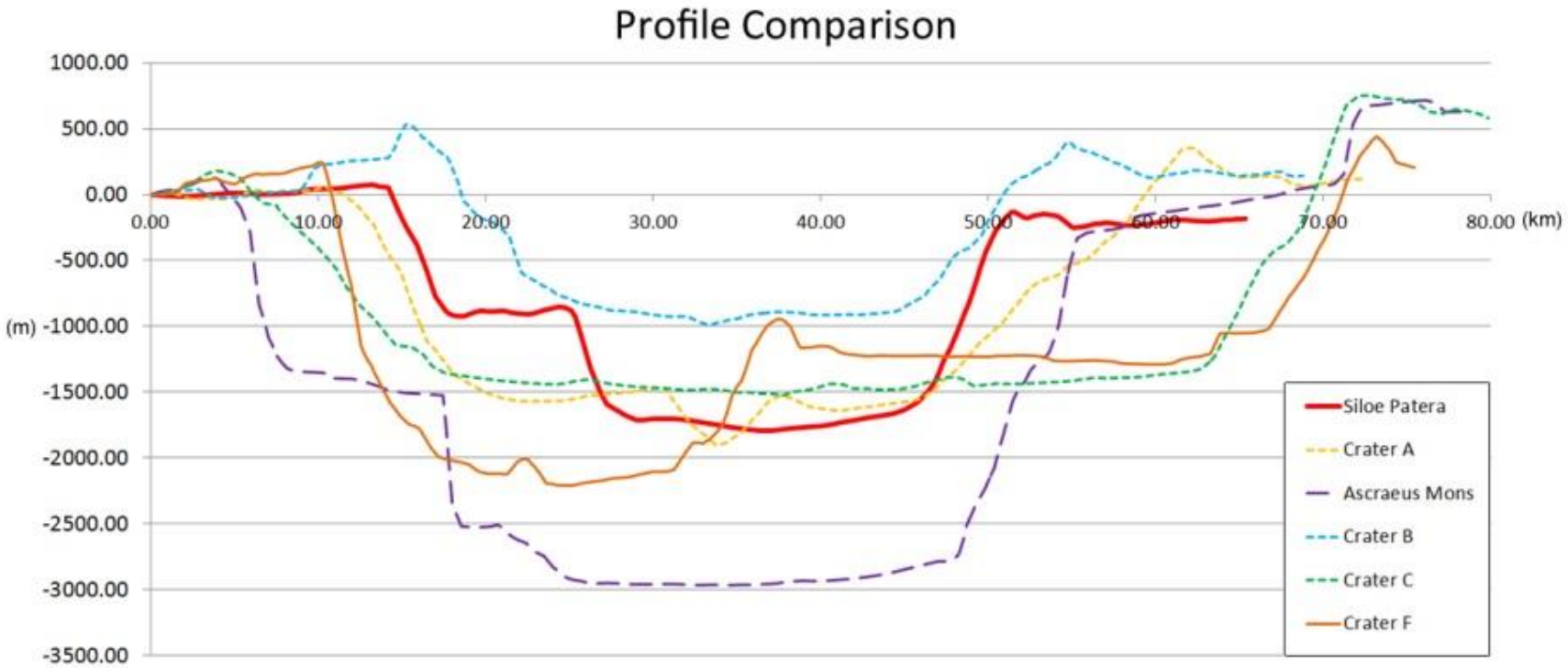

Figure 3
(nested
Excel ar

central peaks or central pit craters, which are common in many impact craters. Crater A

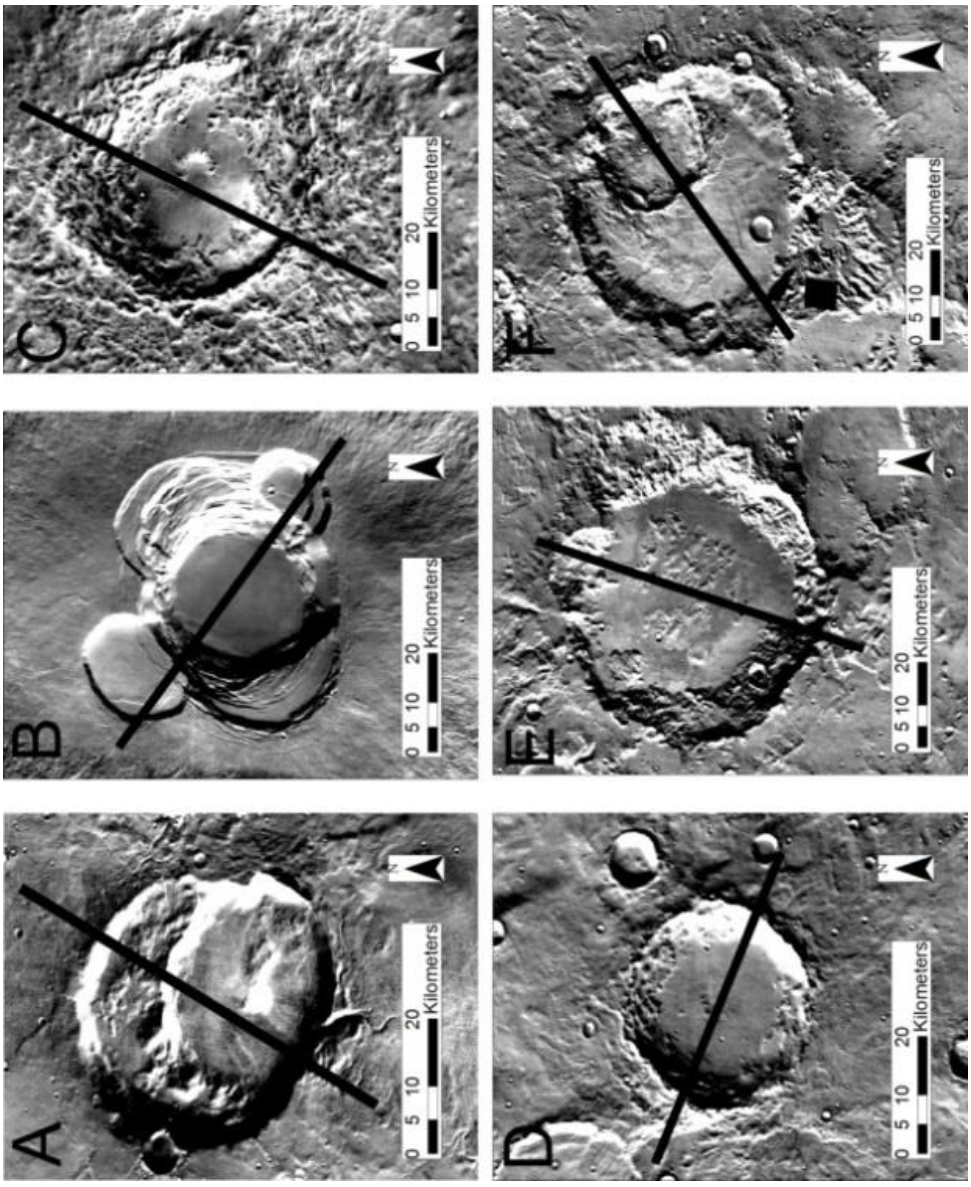

Figure 40: Lines indicate areas the topographic profiles in figure 30 were rendered from. A. Siloe Patera, B. Ascraeus Mons, C. Crater A, D. Crater B, E. Crater C, F. Crater F. Topographic lines were drawn in an effort to best represent each feature.

is located at 25° N and 16° W and is ~ 35 km in diameter. Crater B is at 28° S and 54° E and is roughly 30 km in diameter. Crater C has a diameter of 60 km and is found at 26° S and 172° W. Crater F is found at 27°S and 173°W with a diameter of ~56 km.

Six topographic profiles (Figures 41, 42, and 43) and a contour map of Siloe Patera were created to show its various regions including the spire, volcanic doming and

arcuate slopes. Figure 41 begins with a transect through the bench and across the spire shown trending from the northeast to the southwest. This profile begins with a gentle slope, and not a raised rim associated with impact craters, and moves down to the bench. This portion of the bench is characterized by ring faulting that grade down to an arcuate scarp. The profile transects the most central portion of the spire. Using only this profile, the spire could be mistaken to be a central peak. However, incorporation of all the transects across the spire make interpretation of this structure as an impact-related central peak less likely. The second profile crosses the largest volcanic dome in Siloe Patera, trending form the northwest to the south east. This dome is ~500 m higher than the surrounding elevation of the bench and is approximately 2.5 times higher than a projected impact crater rim from Crater B (Garvin, 2000). Typical impact craters have raised rims that circle the entire crater; however, this is not the case with Siloe Patera as it has isolated raised areas that exceed typical impact crater rim heights and are not continuous as those associated with impact craters. The topographic profile then transects the furthest point of the spire, giving the appearance of a central peak. Similar to profile 1, this transect does not show the full extent of the spire that would disprove a central peak. The third topographic profile shows the transect of the spire trending from the southeast to the northwest. The spire grades down in elevation from the rim toward the center of the floor of Crater B and has multiple raised areas. Viewing the spire from this profile, it is apparent that the spire is not an isolated central peak but

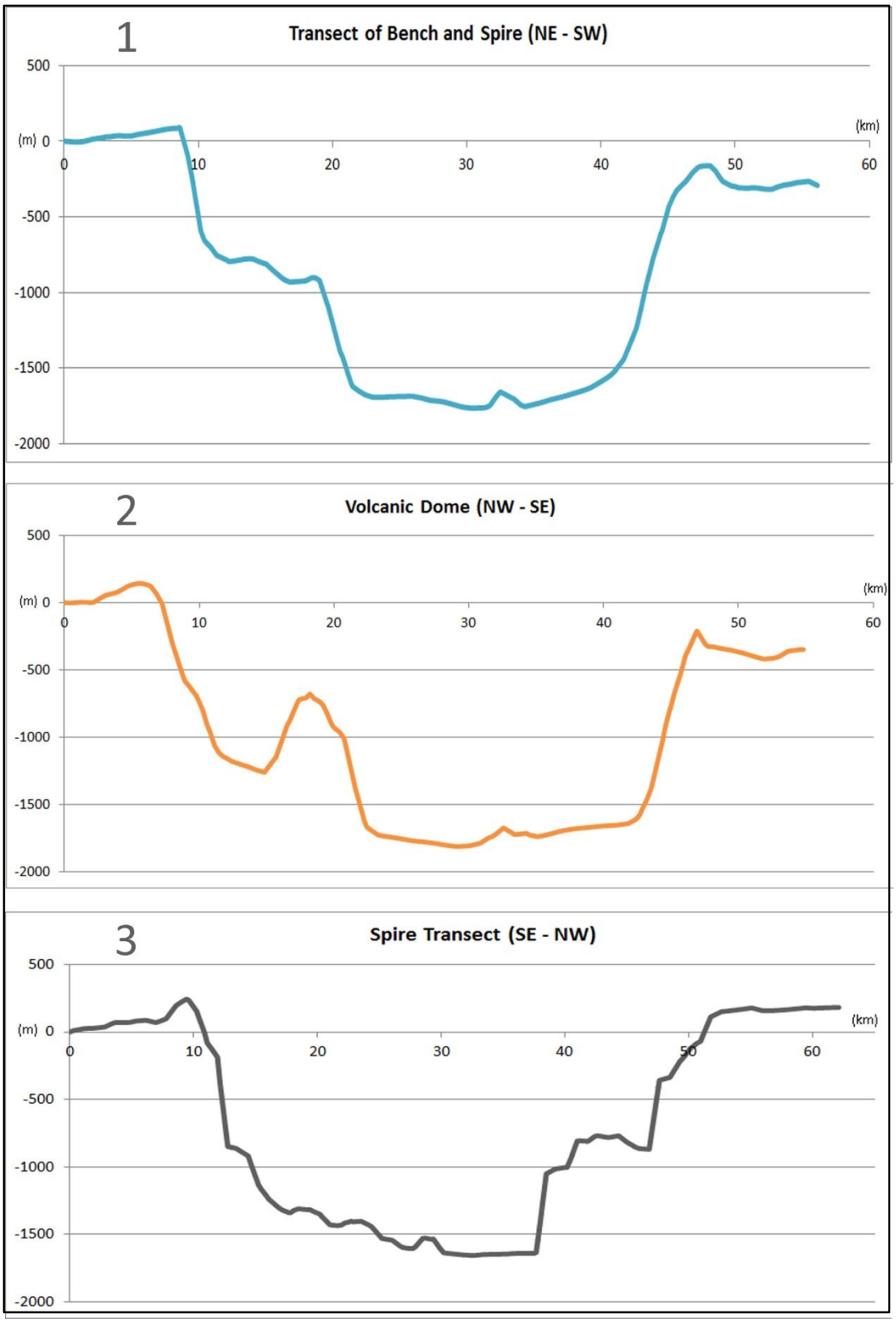

Figure 41: Three topographic profiles of Siloe Patera showing the bench, a volcanic dome, and the spire.

instead is a peninsula shaped formation that extends from the walls of Siloe Patera. As the profile moves toward the northwest, there is an abrupt transition from the floor to the bench and again from the bench to the walls of Crater A. Impact craters are known for their characteristic bowl-shaped depressions; however, Siloe Patera does not display the characteristic bowl-shape with its abrupt transitions seen on the northwestern side of profile 3.

Figure 42 begins with a topographic profile of the whole basin trending from east to west showing the highest elevation to the lowest elevation. There are no raised rims associated with this profile; instead the area outside of Siloe Patera is relatively flat. Due to the location this profile was drawn, it shows a profile similar to profile 3 of the spire with arcuate scarps and abrupt changes from the floor and bench to the walls. The next two profiles transect the lowest and roughly middle elevation of the bench. Profile 5 runs roughly north to south along a channel from the bench to the floor of Crater B that likely had flowing water at one point. This channel is located in between the volcanic dome (profile 2) and the ring faulting (profile 1). It is difficult to interpret the raised areas of the bench to be the raised rim of an impact crater (Crater B) as the channel in profile 5 would need to cut completely through and erode the rim down by ~500 m. The lowest elevation of the bench reaches only ~500 m from the floor of Crater B. Profile 5 steep slopes but appears to have a slight U-shape due to the slope of the channel. The last topographic profile, profile 6, has a broad wedge shape and transects the approximate middle elevation of the bench in between two volcanic domes. This profile

Figure 42: Three topographic profiles of Siloe Patera showing the whole basin, lowest bench elevation, and middle bench elevation.

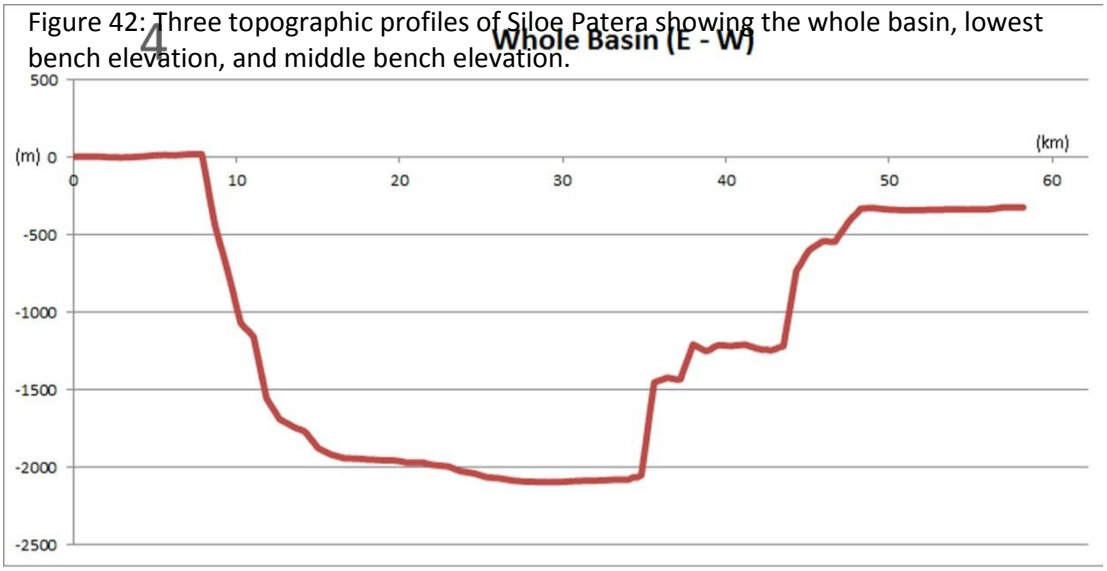

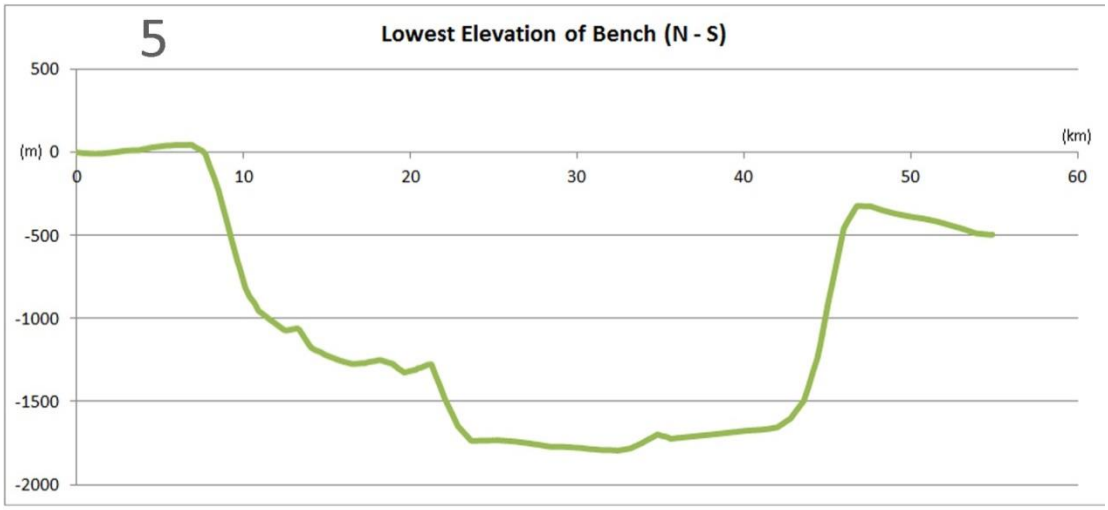

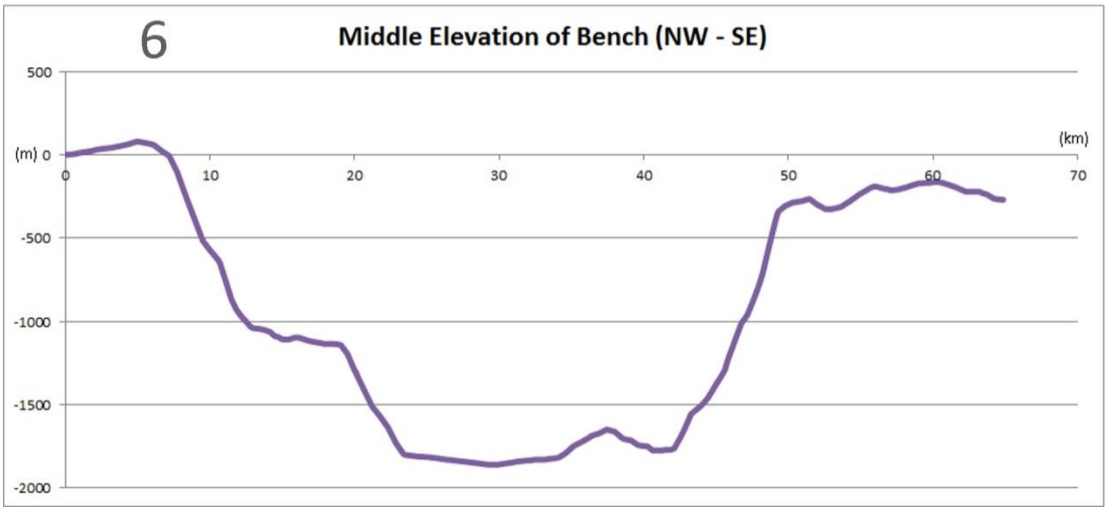

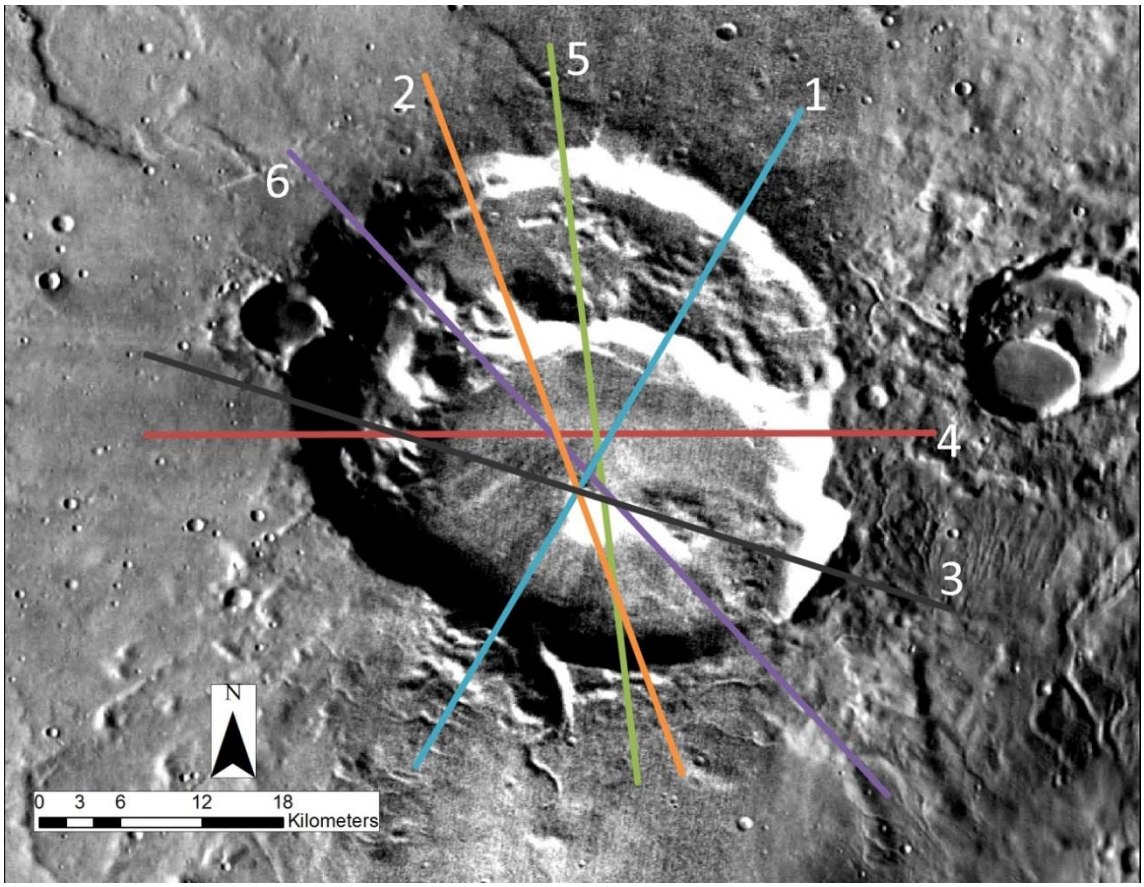

Figure 43: Topographic profiles from Figures 41 and 42.

trends from the northwest to the southeast with another transect of the spire and displays slopes that are not as steep as the other profiles.

If Siloe Patera were the result of two nested impact craters, we would expect to have a central peak that is isolated from the surrounding walls; instead the spire is not isolated and forms a peninsula shape emanating from the southeastern wall of Siloe Patera. A raised rim from Crater B would be expected on the bench and although there are raised areas, they are isolated and are more than double the height of a raised rim typical of impact craters. The majority of slopes shown in Figures X and Y are more steep than would be expect for an impact crater and present a general wedge shape overall.

Siloe Patera does show raised rims around Crater A; however, they are gentle slopes and a characteristic part of the caldera evolution as described by Smith and Bailey (1968). A contour map of Siloe Patera helps to emphasize the steep slopes, spire, volcanic doming and lack of a raised rim (Figure 44).

Slope angles of impact craters, volcanoes, and Siloe Patera can also provide clues as to Siloe Patera's origin. Generally, impact craters are bowl shaped and have smooth and gently sloping walls with low angles. Volcanoes, especially Ascraeus Mons, have much more steeply angled slopes from the arcuate scarps that mark the extent of a past collapse. Siloe Patera is much more similar to Ascraeus Mons than impact craters in this aspect.

In an effort to measure the angles of the slopes, trendlines were inserted on the topographic profiles of each feature (Figure 45). To do this, another graph was generated with only the coordinates of the right slopes of each feature. All graphs were generated and copied and pasted into one graph where a best fit trendline was placed. This graph was then imported into Adobe Photoshop where the angles of the trendlines were measured using the ruler tool. Trendlines of slope angles are as follows: Siloe Patera - 69°, Ascraeus Mons - 67°, Crater A - 42°, Crater B - 49°, Crater C - 60°, Crater F - 64° (Table 4). Siloe Patera, with an angle of 69 degrees, is more like Ascraeus Mons (67 degrees) than the four impact craters of various preservation levels, which range from 42 to 60 degrees. Crater slope angles vary greatly depending on their degradation and the slope measured which produces a wide range of angles; however, Siloe Patera contains a slope angle even higher than Ascraeus Mons.

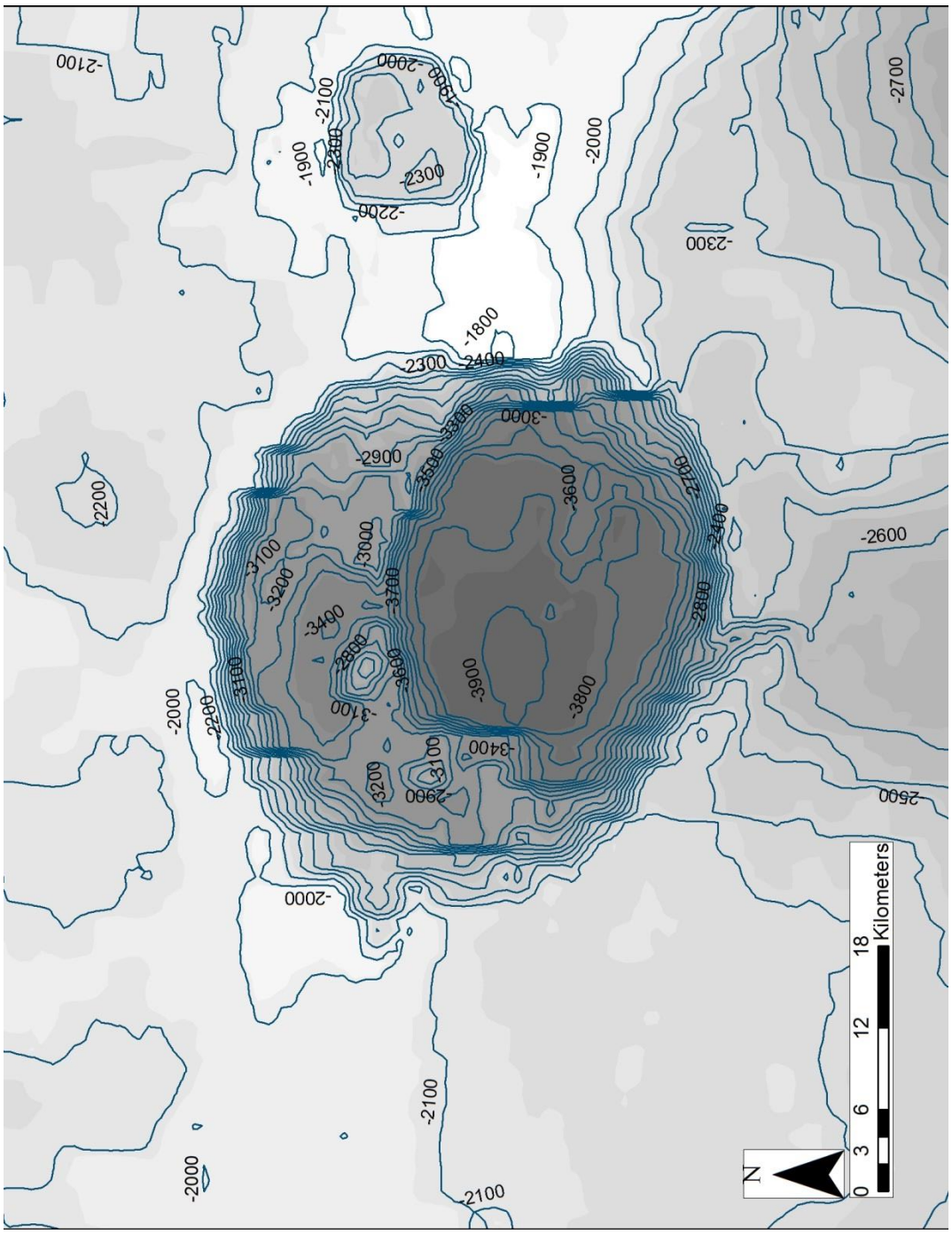

Figure 44: Contour map of Siloe Patera with elevation labels.

Although these slope angles give an idea as to the comparison of Siloe Patera, Ascraeus Mons, and multiple impact craters, they do not speak for the overall slope angle of each. Using ArcGIS, a slope degree map was produced that color codes slope

Table 4: List of slope angles from Figure 41.

Figure 45: Slope angles of Siloe Patera, Ascraeus Mons, Craters A, B, C, and F. Siloe Patera contains the highest slope angle with Ascraeus Mons following.

Siloe Patera	69°
Ascraeus Mons	67°
Crater A	42°
Crater B	49°
Crater C	60°
Crater F	64°

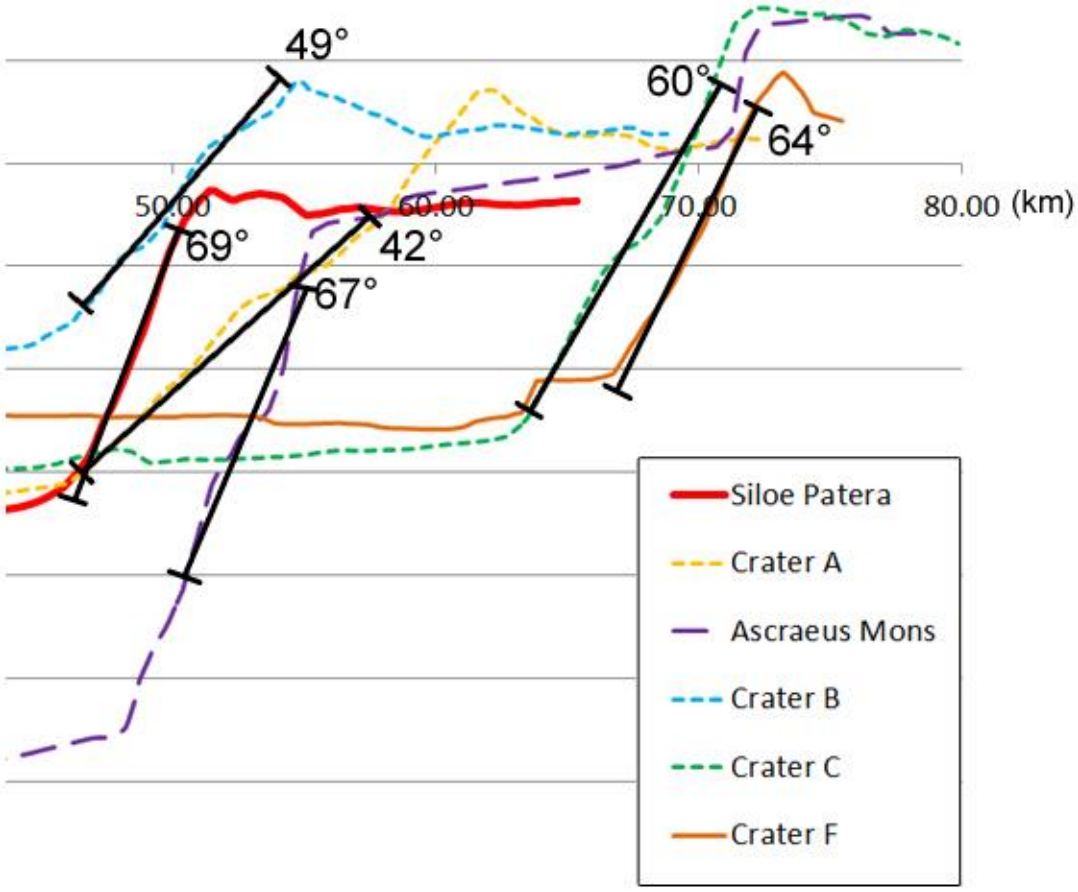

degree ranges. Figure 46 shows red as having the highest slope degree from 64° to 80° and white having a relatively flat slope from 0.004° to 5°. Siloe Patera clearly has very steep slopes on all sides with the volcanic doming showing steep slopes as well.

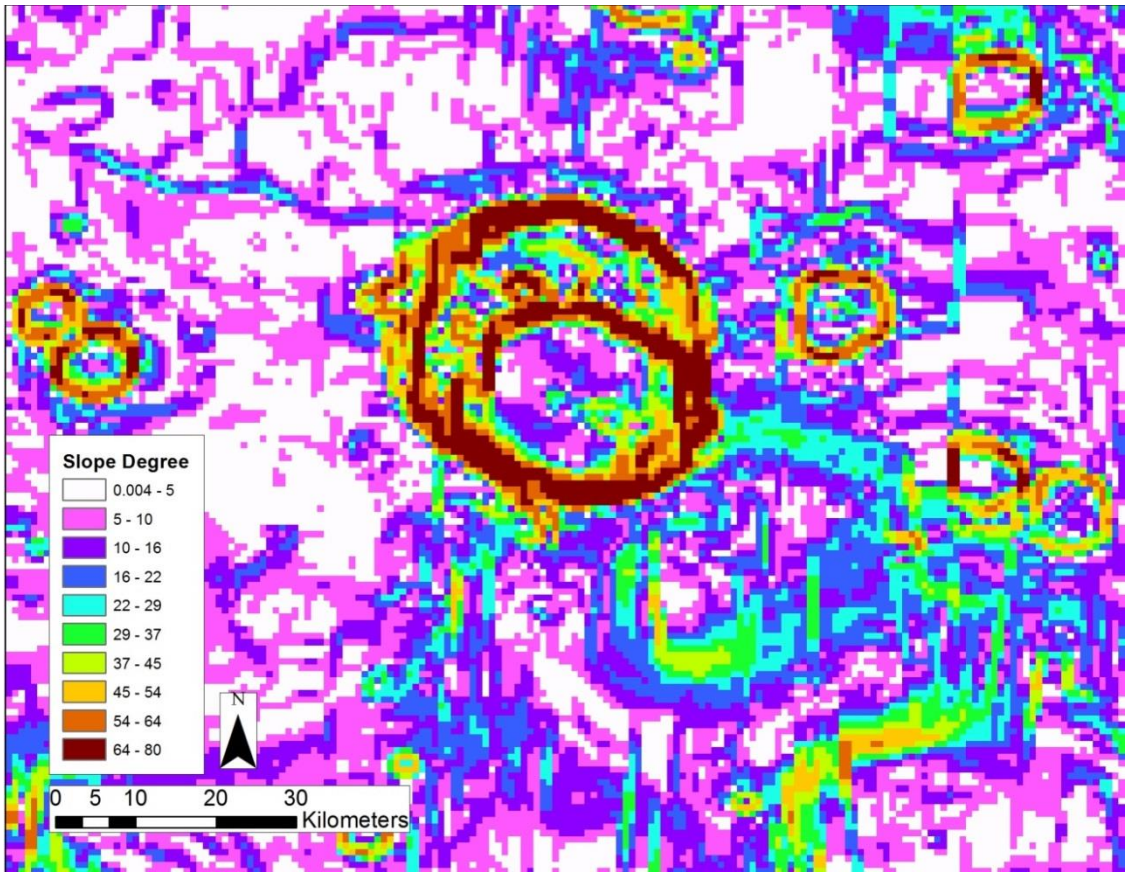

Figure 46: Slope map of Siloe Patera. Red shows steeper slopes and white very shallow slopes.

Other than the spire, Siloe Patera has no apparent internal morphology, raised rim, or definable and uniform ejecta, all of which are indicators and characteristics of impact craters. According to Robbins Crater Database 20120821 (Table 5), Siloe Patera shows impact crater morphology of gullies, ejecta deposits, floor deposits, and slumps. Despite the apparent lack of ejecta, and ejecta and morphology fields labeled null, Siloe Patera has been labeled as an impact crater with the confidence of 4 out of 4. Barlow's Crater Database Version 1(Table 5) states that there is no definable internal morphology or ejecta for Siloe Patera. Barlow only defines one crater for Siloe Patera whereas Robbins defines two different impact craters (Figure 47); however there is little

Robbins Crater Database

OBJECTID	**28414**
CRATER_ID	05-000145
LATITUDE_CIRCLE_IMAGE	35.344
LONGITUDE_CIRCLE_IMAGE	6.529
LATITUDE_ELLIPSE_IMAGE	35.503
LONGITUDE_ELLIPSE_IMAGE	6.532
DIAM_CIRCLE_IMAGE	33.59
DIAM_CIRCLE_SD_IMAGE	0.1
DIAM_ELLIPSE_MAJOR_IMAGE	35.16
DIAM_ELLIPSE_MINOR_IMAGE	33.41
DIAM_ELLIPSE_ECCEN_IMAGE	0.31
DIAM_ELLIPSE_ELLIP_IMAGE	1.05
DIAM_ELLIPSE_ANGLE_IMAGE	20
LATITUDE_CIRCLE_TOPOG	35.377
LONGITUDE_CIRCLE_TOPOG	6.518
DIAM_CIRCLE_TOPOG	36.03
DIAM_CIRCLE_SD_TOPOG	<null>
DEPTH_RIM_TOPOG	-2.09
DEPTH_RIM_SD_TOPOG	0.11
DEPTH_SURFACE_TOPOG	-2.19
DEPTH_SURFACE_SD_TOPOG	0.19
DEPTH_FLOOR_TOPOG	-3.35
DEPTH_FLOOR_SD_TOPOG	0.05
DEPTH_RIMFLOOR_TOPOG	1.26
DEPTH_RIMHEIGHT_TOPOG	0.11
DEPTH_SURFFLOOR_TOPOG	1.16
PTS_USED_RIM_IMAGE	145
PTS_USED_RIM_TOPOG	71
PTS_USED_SURFACE	131
PTS_USED_FLOOR	29
PTS_USED_LAYER_1	<null>
PTS_USED_LAYER_2	<null>
PTS_USED_LAYER_3	<null>
PTS_USED_LAYER_4	<null>
PTS_USED_LAYER_5	<null>
NUMBER_LAYERS	3
MORPHOLOGY_CRATER_1	CpxUnc
MORPHOLOGY_CRATER_2	Gullies

MORPHOLOGY_CRATER_3	Ejecta Deposits / Floor Deposits / Slump Deposits
MORPHOLOGY_EJECTA_1	MLERS
MORPHOLOGY_EJECTA_2	HuBL
MORPHOLOGY_EJECTA_3	<null>
MORPHOLOGY_EJECTA_COMMENTS	<null>
DEGRADATION_STATE	<null>
CONFIDENCE_IMPACT_CRATER	4
LAYER_1_PERIMETER	<null>
LAYER_1_AREA	<null>
LAYER_1_LOBATENESS	<null>
LAYER_1_EJECTARAD_EQUIV	<null>
LAYER_1_EJECTARAD_REL	<null>
LAYER_2_PERIMETER	<null>
LAYER_2_AREA	<null>
LAYER_2_LOBATENESS	<null>
LAYER_2_EJECTARAD_EQUIV	<null>
LAYER_2_EJECTARAD_REL	<null>
LAYER_3_PERIMETER	<null>
LAYER_3_AREA	<null>
LAYER_3_LOBATENESS	<null>
LAYER_3_EJECTARAD_EQUIV	<null>
LAYER_3_EJECTARAD_REL	<null>
LAYER_4_PERIMETER	<null>
LAYER_4_AREA	<null>
LAYER_4_LOBATENESS	<null>
LAYER_4_EJECTARAD_EQUIV	<null>
LAYER_4_EJECTARAD_REL	<null>
LAYER_5_PERIMETER	<null>
LAYER_5_AREA	<null>
LAYER_5_LOBATENESS	<null>
LAYER_5_EJECTARAD_EQUIV	<null>
LAYER_5_EJECTARAD_REL	<null>
CRATER_NAME	<null>
Shape	Point

OBJECTID	**28500**
CRATER_ID	05-000231
LATITUDE_CIRCLE_IMAGE	35.194

LONGITUDE_CIRCLE_IMAGE	6.598
LATITUDE_ELLIPSE_IMAGE	35.197
LONGITUDE_ELLIPSE_IMAGE	6.597
DIAM_CIRCLE_IMAGE	26.27
DIAM_CIRCLE_SD_IMAGE	<null>
DIAM_ELLIPSE_MAJOR_IMAGE	27.96
DIAM_ELLIPSE_MINOR_IMAGE	24.76
DIAM_ELLIPSE_ECCEN_IMAGE	0.47
DIAM_ELLIPSE_ELLIP_IMAGE	1.13
DIAM_ELLIPSE_ANGLE_IMAGE	86
LATITUDE_CIRCLE_TOPOG	35.203
LONGITUDE_CIRCLE_TOPOG	6.602
DIAM_CIRCLE_TOPOG	26.62
DIAM_CIRCLE_SD_TOPOG	10.04
DEPTH_RIM_TOPOG	-2.71
DEPTH_RIM_SD_TOPOG	0.41
DEPTH_SURFACE_TOPOG	-3.04
DEPTH_SURFACE_SD_TOPOG	0.32
DEPTH_FLOOR_TOPOG	-3.89
DEPTH_FLOOR_SD_TOPOG	0.03
DEPTH_RIMFLOOR_TOPOG	1.18
DEPTH_RIMHEIGHT_TOPOG	0.33
DEPTH_SURFFLOOR_TOPOG	0.86
PTS_USED_RIM_IMAGE	186
PTS_USED_RIM_TOPOG	78
PTS_USED_SURFACE	34
PTS_USED_FLOOR	51
PTS_USED_LAYER_1	<null>
PTS_USED_LAYER_2	<null>
PTS_USED_LAYER_3	<null>
PTS_USED_LAYER_4	<null>
PTS_USED_LAYER_5	<null>
NUMBER_LAYERS	<null>
MORPHOLOGY_CRATER_1	CpxCPk
MORPHOLOGY_CRATER_2	Gullies
MORPHOLOGY_CRATER_3	Slump Deposits
MORPHOLOGY_EJECTA_1	Rd
MORPHOLOGY_EJECTA_2	<null>
MORPHOLOGY_EJECTA_3	<null>
MORPHOLOGY_EJECTA_COMMENTS	<null>

DEGRADATION_STATE	<null>
CONFIDENCE_IMPACT_CRATER	4
LAYER_1_PERIMETER	<null>
LAYER_1_AREA	<null>
LAYER_1_LOBATENESS	<null>
LAYER_1_EJECTARAD_EQUIV	<null>
LAYER_1_EJECTARAD_REL	<null>
LAYER_2_PERIMETER	<null>
LAYER_2_AREA	<null>
LAYER_2_LOBATENESS	<null>
LAYER_2_EJECTARAD_EQUIV	<null>
LAYER_2_EJECTARAD_REL	<null>
LAYER_3_PERIMETER	<null>
LAYER_3_AREA	<null>
LAYER_3_LOBATENESS	<null>
LAYER_3_EJECTARAD_EQUIV	<null>
LAYER_3_EJECTARAD_REL	<null>
LAYER_4_PERIMETER	<null>
LAYER_4_AREA	<null>
LAYER_4_LOBATENESS	<null>
LAYER_4_EJECTARAD_EQUIV	<null>
LAYER_4_EJECTARAD_REL	<null>
LAYER_5_PERIMETER	<null>
LAYER_5_AREA	<null>
LAYER_5_LOBATENESS	<null>
LAYER_5_EJECTARAD_EQUIV	<null>
LAYER_5_EJECTARAD_REL	<null>
CRATER_NAME	<null>
Shape	Point

Barlow Crater Database

FID	**4283**
Shape	Point
SUBQUAD	05SW
ID	400
LATITUDE	35.52
LONGITUDE	6.59
DIAMETER	41.2
TERRAIN	HCr

TYPE	#c
EJECTA_MOR	No
INTERIOR_M	No
PIT_DIAMET	0
MIN_DIAMET	0
ANGLE	999
COMMENTS	none

Table 5: Robbins and Barlow Crater Databases information collected on Siloe Patera.

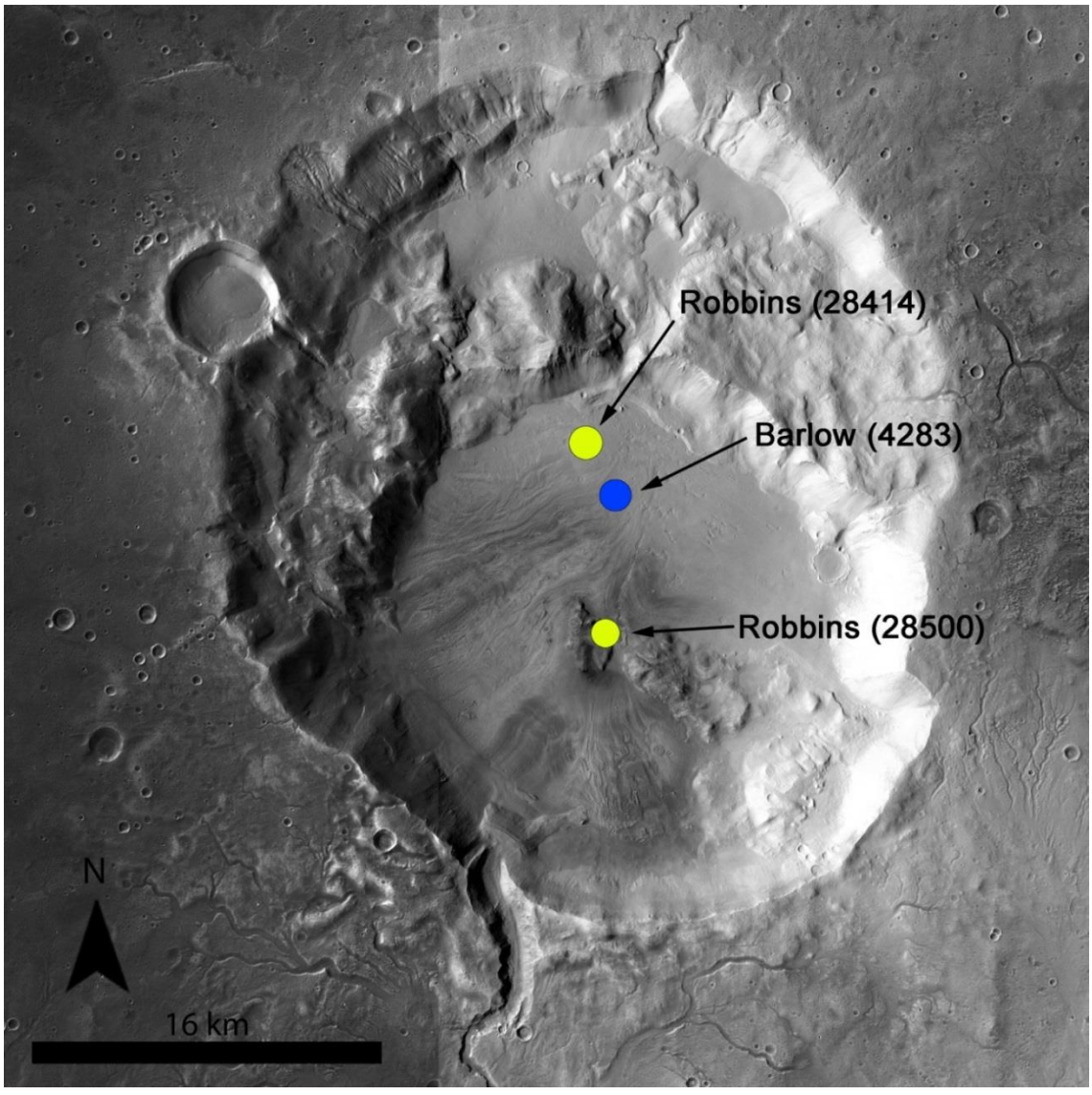

Figure 47: Crater databases used are displayed and each circle shows the area determined to be the center of the crater according to Robbins and Barlow. Robbins shown in yellow and Barlow in blue followed by the object number for each point in their database.

evidence of typical impact crater characteristics present. Information filled out and provided by Robbins and Barlow were downloaded from USGS PIGWAD website and imported into ArcGIS to analyze and display data along a Mars_2000 geographic coordinate system.

Robbins Crater Database was generated using THEMIS Daytime IR on board Mars Odyssey (Robbins and Hynek, 2012). All visible impact craters larger than 1 km in diameter were identified, analyzed and applied to this database. Robbins has many fields that are left null but fields on impact crater and ejecta morphology have been labeled as having impact crater characteristics. For object 28414, equivalent to Crater A of Siloe Patera, Robbins indicates that it is a complex unclassified chaotic (CpxUnc) impact crater where object 28500, Crater B of Siloe Patera, is classified as complex central peaks (CpxCPk), referring to the feature we have dubbed as a spire. Object 28414 (Crater A)is classified as having two ejecta layers: 1. Multiple Layer Ejecta Rampart Sinuous (MLERS), 2. Hummocky broad lobes (HuBL). Object 28500 (Crater B) has one ejecta morphology labeled as radial ejecta. On the other hand, Barlow does not indicate any ejecta or internal morphology from her Version 1 Crater Database although she does indicate the terrain as being heavily cratered uplands (HCr) with no apparent embayment by intercrater plains. Barlow has produced a second, more detailed, version of the Crater Database but this version has not been released yet.

Flow features propagate from Siloe Patera's rim to the north, southeast, and southwest and could be interpreted as ejecta or lava flows (Figure 48). Since there are two collapse/impact events, it is not possible to determine with which event the flow

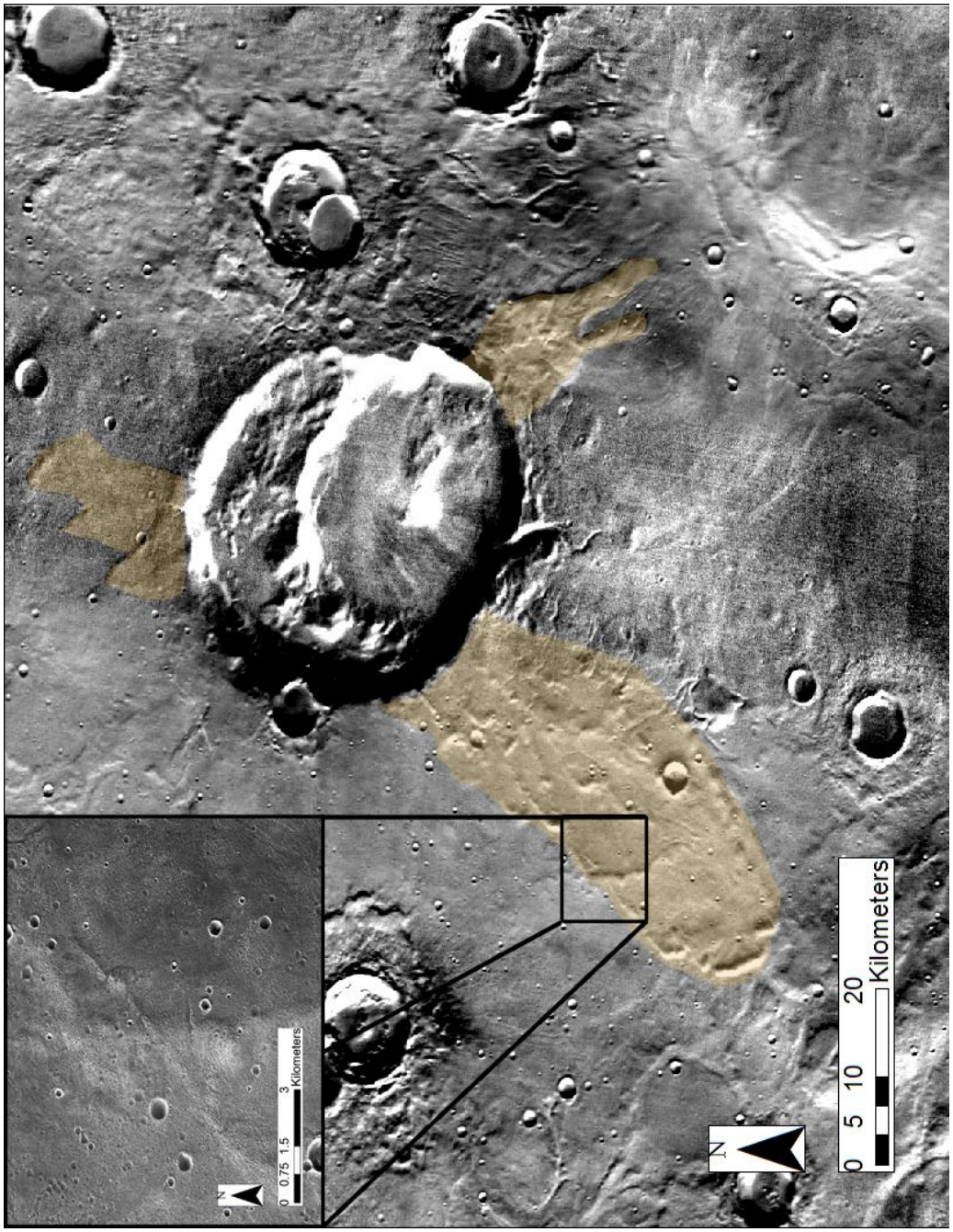

Figure 48: Flow features highlighted in tan and described in Table 2. Each flow has its own characterizes ranging in length, width and general appearance. Box to the top left of the image shows a zoomed in CTX image of an overlap in the southwestern flow.

features are associated. Much can be interpreted by the distance of each flow from the rim as seen in Table 6. The north flow and southeastern flow could easily be interpreted to represent ejecta layers as their distance falls within acceptable ranges from the

impact site. However, the southwestern flow extends almost triple the radius of Crater A and Crater B of Siloe Patera

	N Flow	SE Flow	SW Flow
Crater A	28	38	61
Crater B	36	30	56

Table 6: Distance from Crater A and Crater B center (km) to edge of flow features.

Figure 48 flows are highlighted in tan shown on a THEMIS Day Infrared image. Each flow feature appears to have its own characteristics and does not resemble each other. The southwestern flow is very broad and expands outwards from the rim and spans a great distance from Siloe Patera. This flow does not appear to have high amounts of degradation or weathering and even displays an overlap (Figure 48) indicating multiple flow events. The northern flow is highly degraded and flat and does not extend more than one radius of Siloe Patera (17 km). The southeastern flow extends a little over one radius of Siloe Patera but displays a more elongated and thin appearance unlike the others that are flat and broad.

CHAPTER 5

Because features observed at Siloe Patera could be interpreted as both impact and volcanic in origin, regions of interest are discussed below in the context of both. Siloe Patera contains features interpreted as ring faults that have been partially covered by dust and other debris. These faults exist in a region ~ 18 km long by 8 km wide and are located on the northeast portion of Siloe Patera's bench (Figure 3B). From the south, faults along the bench begin to curve slightly until they tract north – northwest at the

most northern portion of Siloe Patera. This is most easily seenseen in Figure 3B. If interpreted as ring fractures, they would be associated with the beginning stages of subsidence for Crater B before it collapsed. These features are shown to be bright in THMIS Night IR and in the color stretch map which could be interpreted as exposed fault scarps.

Siloe Patera contains features interpreted as ring faults that have been partially covered by dust and other debris. These faults exist in a region ~ 18 km long by 8 km wide and are located on the northeast portion of Siloe Patera's bench (Figure 3B). From the south, faults along the bench begin to curve slightly until they tract north – northwest at the most northern portion of Siloe Patera. This is most easily seen in Figure 3B. If interpreted as ring fractures, they would be associated with the beginning stages of subsidence for Crater B before it collapsed. These features are shown to be bright in THMIS Night IR and in the color stretch map which could be interpreted as exposed fault scarps.

The spire located on the floor of Crater B is an odd structure that could be interpreted in a number of ways. It can be divided into two parts (Figure 49) and appears to have been covered by sediments. The region of the spire located directly in the middle of Crater B is ~ 3 km long by 2 km wide and raises to a height of 80 meters from the floor of Crater B. The remaining portion of the sprire extends from the middle portion of the spire and connects with the wall of Siloe Patera on its southeastern side. It is ~ 11 km long by 5 km wide and thickens as it approaches the wall, with its highest point being 257 m from the Crater B's floor. In the context of an impact origin, the spire

would be interpreted as a central peak due to its isolated location in the middle of the crater floor. However, because the spire extends out from the southeastern wall (Figure 3 and Figure 13), it is more likely that it is the result of a mass wasting event or an extension of the underlying rock defining the spire morphology. This suggests that it is less likely to be the result of a mass wasting event and is more likely part of the spire itself.

When observing the spire in THEMIS Night IR (Figure 22 and 38) and in the stretch color map (Figure 31), we can see that the spire and surrounding area is among the brightest regions on the map. This suggests that the spire and much of the floor of Crater B is solid rock, uncharacteristic of impact craters, which have flat floors created by fill-in of dust and sand. When looking at the THEMIS Night IR image (Figure 30), it is apparent that impact craters floors around Siloe Patera are filled with dust and sand

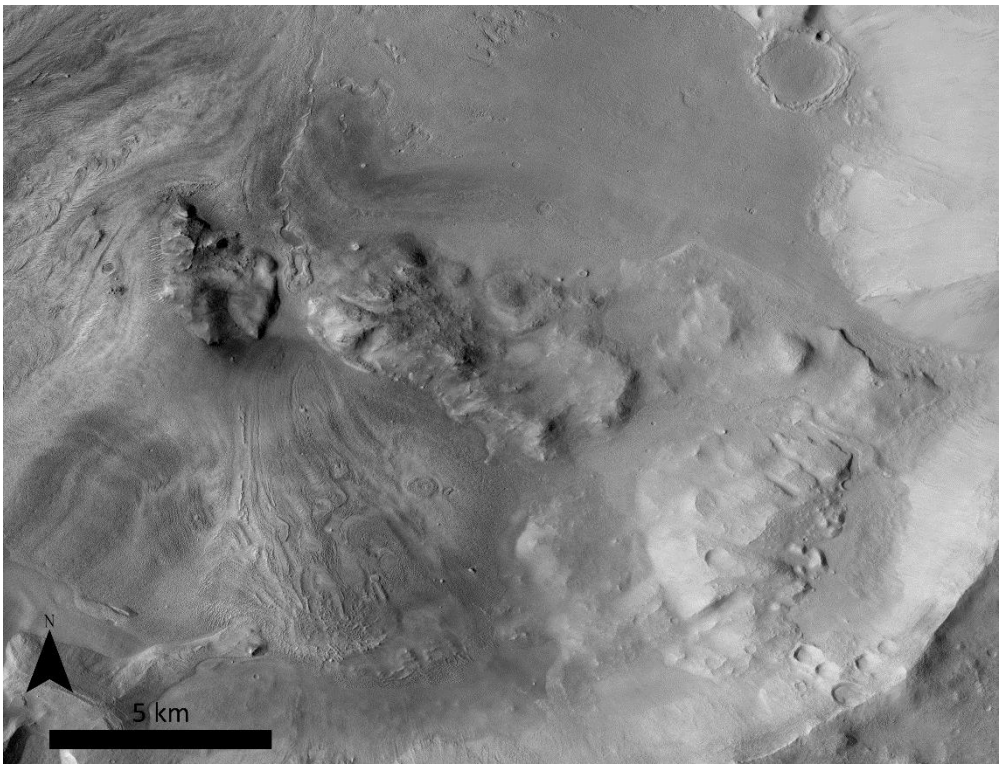

Figure 49: Close up view of the spire located on the floor of Crater B in Siloe Patera.

because they appear dark, suggesting low thermal inertia. In impact craters that have central peaks, those peaks are generally bright in THEMIS Night IR, while the rest of the surrounding crater floor is dark. This can be observed in two sets of conjoined impact craters to the left and right of Siloe Patera (Figure 30).

Therefore, it is more likely that the spire has a volcanic or mass wasting origin than an impact crater origin. In the context of a volcanic origin, the presence of the spire is best explained as resurgent dome. If the spire is a resurgent dome we would expect to see uplift to angles of more than 65° and distension faults. Due to dusty conditions, it is possible that visitation, by human or rover, may be required to fully determine its origin.

Post-volcanic doming is another region of interest that was revealed during 3D modeling of Siloe Patera as part of this research. Five to six potential post-volcanic doming features are labeled in Figures 3B and 33. Elevations of peaks were determined by manipulating classes and colors of an interpolated IDW map that was previously constructed. Forty classes were applied and a range of elevations were given for each class. The highest elevation in each given range was chosen to represent each feature's height, measured from the lowest elevation of Siloe Patera's Crater B floor, at –~3931m below the mart. Dome heights from the floor of Crater B are as follows: (1) 957 m;(2) 1,116 m;(3) 841 m;(4) 1,240 m; and (5) 1,010 m. Dimensions of each dome range in size, but are approximated: (1) 3.3 km x 1.7 km; (2) 4.3 km x 4.1 km ;(3) 2.1 km x 1.2 km;(4) 5.6 km x 4.3 km; and (5) 2.8 km x 1.4 km.

These domes are bright in THEMIS Night IR (Figure 30) and appear green in the color stretch map (Figure 31). They could be explained as resurgent domes built in

Crater A on lake sediments and caldera fill from the first collapse event prior to the younger caldera forming events associated with Crater B. In this case, these domes may have developed along ring fractures associated with the development of Crater B, where magma rising through the ring faults create a semi-circle of volcanic domes (Figure 3B).

Siloe Patera has a number of sporadic flow features around the rim which vary in shape, length, and other characteristics. In the THEMIS Night IR image (Figure 30) and the color stretch map (Figure 31), the head of the flows appear as solid rock with the rest covered in dust. The fact that these flows are not found all around Siloe Patera, but only in specific areas is not supportive of the impact crater origin hypothesis because ejecta from impact craters generally covers the significant regions around impact crater. Definable ejecta accompanies the majority of impact craters and considering that an impact origin for Siloe Patera requires two impact events, ejecta should be abundant in the region surrounding Siloe Patera. These flows of limited spatial extent also vary significantly in distance and appearance, which suggests they were not created by the same process. The southwest flow (Table 6) extends more than double the distance of the southeast and north flows and also maintains a broad, flat appearance. The southeast and north flows extend away from Siloe Patera for distances typical of impact craters and have a more fluid and finger-like appearance. It is possible that the flows are ejecta deposits, with the southeast and north flows formed during a single impact (Crater A) event, with the southwest flow formed during a subsequent impact event (Crater B). This however, does not explain the notable lack of an extensive ejecta

blanket,. The lack of a clear and definable, extensive ejecta blanket make an impact crater origin for Siloe Patera a less than satisfactory model of formation.

Evidence of subsidence to the south of Crater B is a unique feature not typical of impact craters, but may be suggestive of volcanism. This region of subsidence (Figure 50) has a shallow, irregular V-shape with an area of ~2,015 $km^2$and dimensions of ~36 x 18 km. Its lowest point is ~ -2015 m below Martian sea level which is ~ 1030 meters above Siloe Patera's lowest point and 700 meters below the average surrounding surface. Most of this sag feature is suggestive of a material with high thermal inertia on THEMIS Night IR and on the color stretch map, typical of solid rock. This subsidence feature could represent the very beginning stages of caldera collapse, prior to the development of ring fractures which have propagated to the surface, associated with a magma chamber at depth which has migrated away from the area, or which cooled. Figure 45 models one possible scenario for the succession and history of Siloe Patera's subsidence feature.

The depth to diameter ratio (d/D) of an impact crater is fairly standard and most impact craters fall within the 0.03 to 0.17 interval. Due to degradation, modification, and size, impact crater d/D ratios can vary greatly enough to encompass known volcanic calderas like Ascraeus Mons. Although Siloe Patera and Ascraeus Mons fall within the crater d/D ratio range, Siloe Patera and Ascraeus Mons fall very close to the edge of the

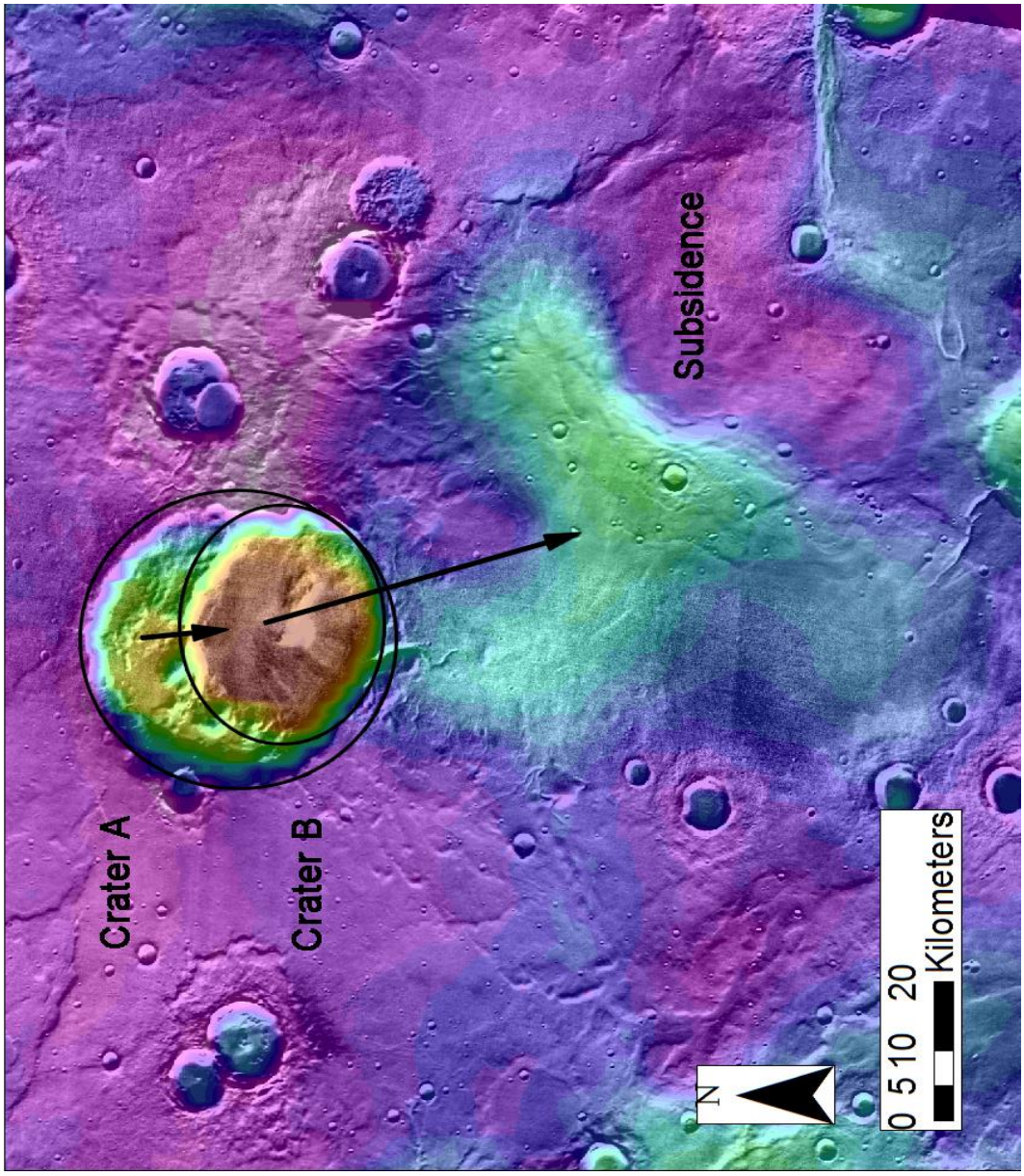

Figure 50: Possible movement history of a magma chamber below Siloe Patera.

range at 0.03 (Gravin and Frawley, 1998). Siloe Patera has a d/D of 0.049, which is almost identical to Ascraeus Mons at a d/D of 0.048. According to a graph of rim-floor depth vs. impact crater diameter in a recent paper (Michalski and Bleacher, 2013), Siloe Patera's Crater A and Crater B contain a higher depth to diameter ratio than should be expected due to its Noachian/Hesperian age (Figure 51). The degradation of impact

craters is divided into 4 classes with class 1 being highly degraded and class 4 pristine. Crater A falls along the class 2 trendline, suggesting it is older and has had time to undergo erosion in an impact crater model of formation. Crater B is suggestive of pristine and fresh impact craters. However, if Siloe Patera is considered a Hesperian impact crater, it should plot as a Class 1. However, both Crater A and Crater B have d/D ratios similar to young impact craters and should, therefore, have degradation features typical of class, 2, 3, and 3 impacts. This conflict between the apparent age of the crater based on d/D ratios and that based on degradation features suggests an impact origin for Siloe Patera is problematic.

Garvin (2000) developed a relation between impact crater depth values and crater diameter values for non-polar complex impact craters. The impact craters that were examined for non-polar impact craters were best represented by a power law of the form $d = 0.19D^{0.55}$, where d and D are measured in kilometers. Impact craters that have a diameter of 20 km should generate a depth of ~1km, a 40 km diameter crater should produce a depth of 1.6 km and an 80 km diameter crater should create a depth up to 2.5 km. If Siloe Patera is an impact crater, we would expect to see a depth of ~1.3 km as a fresh impact crater. Siloe Patera exceeds this calculation by ~0.5, but has had significant time to fill in resulting in a flat floor. An impact origin for Siloe Patera would suggest it is a relatively pristine crater.

If Craters A and B were relatively recent impacts, they would look similar to an unnamed impact crater, roughly the size of Crater B, located to the northeast (Figure 52) of Siloe Patera. This impact crater has not had significant amounts of degradation and

has a uniform ejecta blanket that completely surrounds it. We would expect to see the

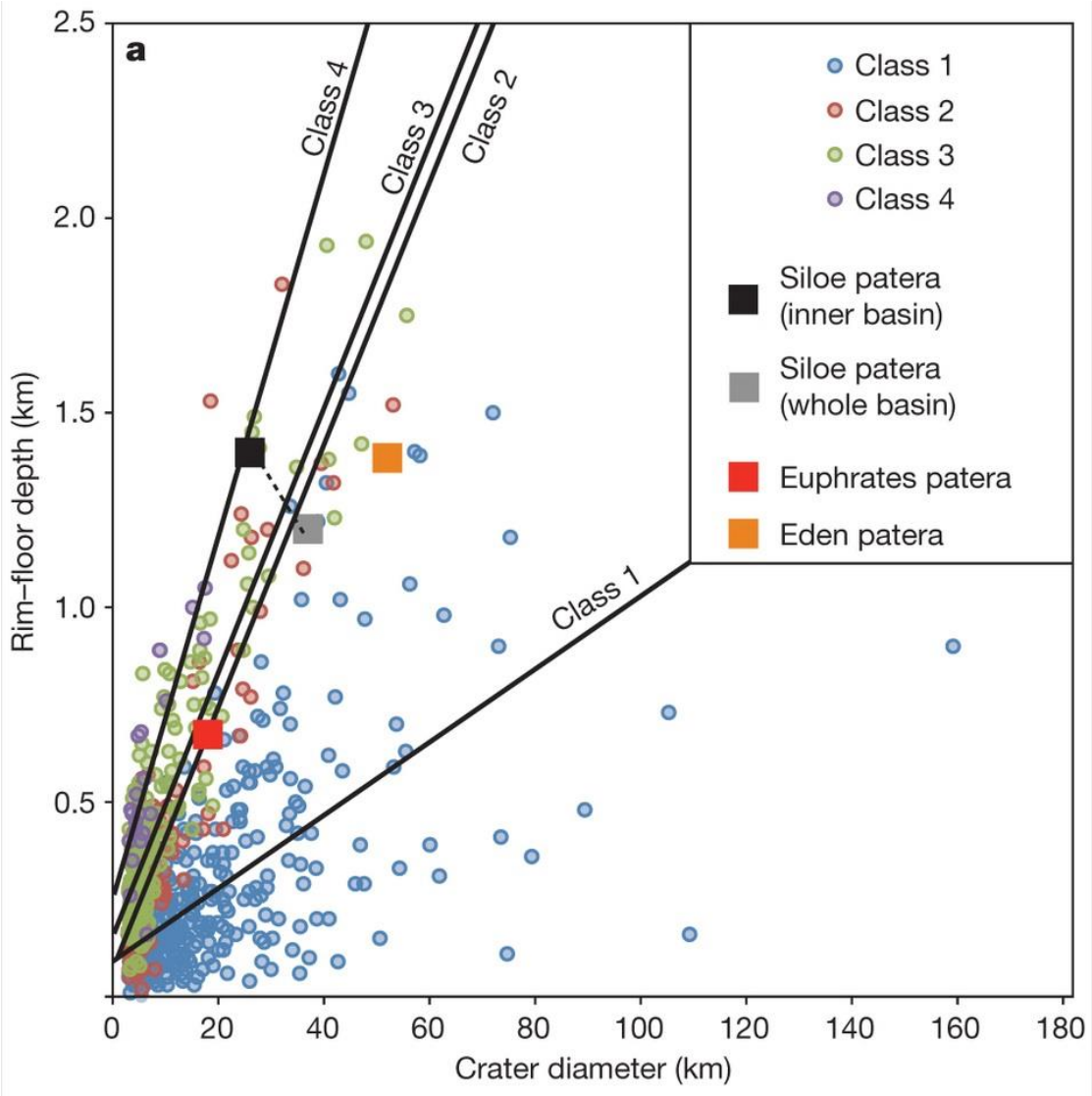

Figure 51: Siloe Patera Crater A falls within the more degraded impact craters and Crater B is considered to be new (Michalski and Bleacher, 2013).

same impact characteristics in Siloe Patera as this crater if it were the result of a relatively young impact event as suggested by the d/D ratio. There is, however no evidence for an extensive ejecta blanket, a central peak isolated from the crater rim and the depth of Siloe Patera far surpasses the depth of the unnamed crater.

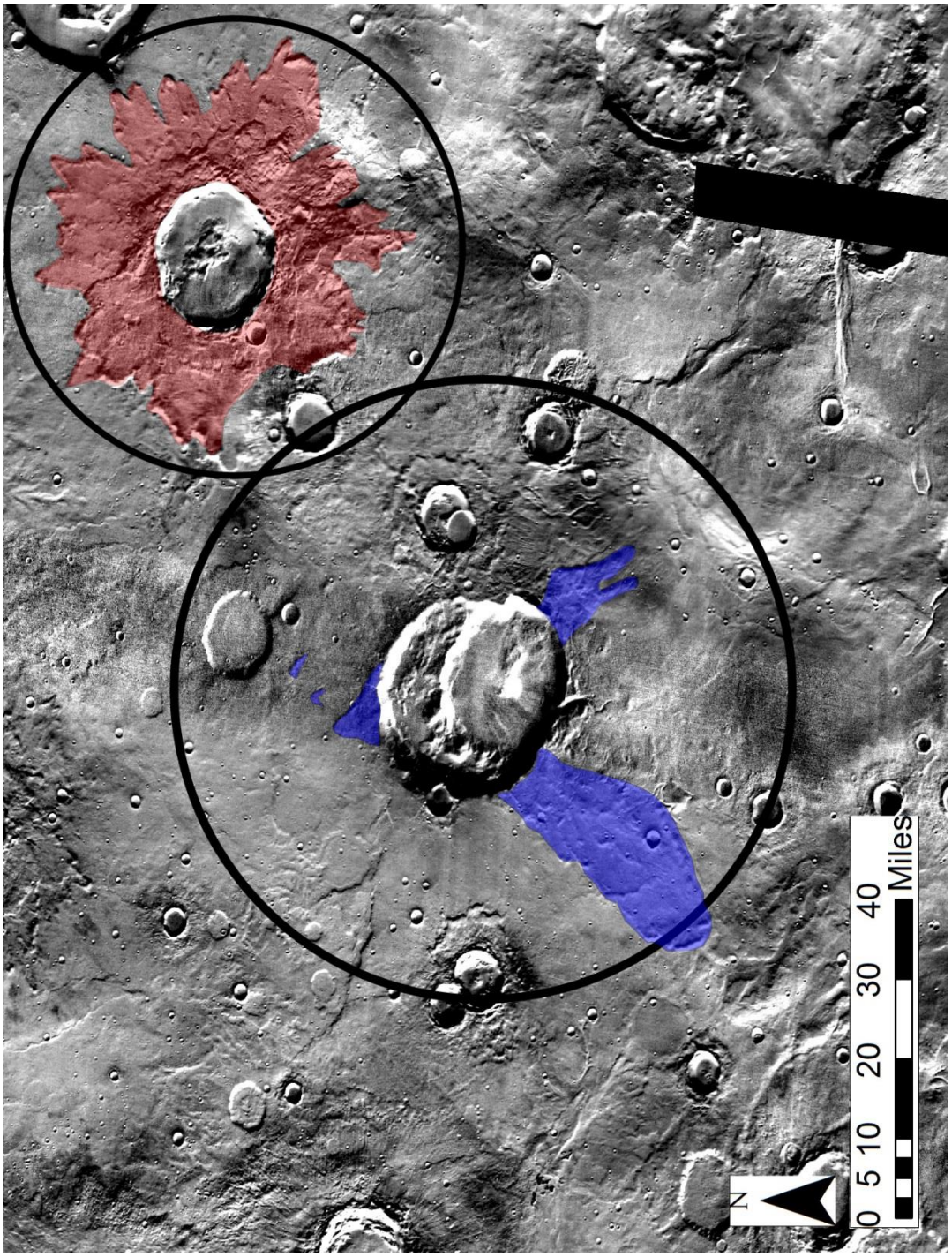

Figure 52: A comparison of Siloe Patera to a similar sized crater to the north east.

Streams and channels can also aid in distinguishing between an impact crater and volcanic origin for Siloe Patera. Due to the raised rims around an impact crater; water will flow down the rim, into the ejecta blanket and create a path. This path begins

at the top of the rim and will flow downhill toward the ejecta blanket (Figure 40). Siloe Patera's stream channels to the south, flow into the large area of subsidence, while others flow into Crater B through a large channel on the southern flank of Siloe Patera (Figure 50).Channels also flow from the bench of Crater A to the floor of Crater B, reinforcing the lack of a raised rim around Crater B. Figure 3A highlights the channels around Siloe Patera and shows their flow direction. For comparison, the small impact crater along the western rim of Siloe Patera has a few channels that flow downhill from the rim, typical of an impact crater's raised rim.

Comparison of Crater F to Siloe Patera was chosen due to the fact that it contains a secondary crater completely encompassed in a larger impact crater with one wall being shared by both (Figure 53). Like Crater A and B of Siloe Patera, the shared wall has arcuate scarps. However, the arcuate scarp was only present in a small area before the hummocky and chaotic terrane of an impact crater took over. The fill of the secondary impact crater is rough, modified and filled with slump blocks mass wasting from the rim. These mass wasting events stay along the walls of the impact crater and do not reach the center of the crater floor. A central peak is easily defined in the center of the secondary impact crater. Moving from the secondary impact crater to the primary impact crater, a uniform and prominent raised rim rests along the boundary between both impact craters. Siloe Patera's Crater B does not have a raised rim that rest on top of Crater A, unlike the unnamed Crater F. The floor of the primary crater is relatively flat with no features other than possible minor ejecta and a smaller impact crater. The rim of the primary impact crater is similar to the rim of the secondary impact crater with

Figure 53: Comparison of Siloe Patera (above) to Crater F (below). Many differences can be seen here as described in text.

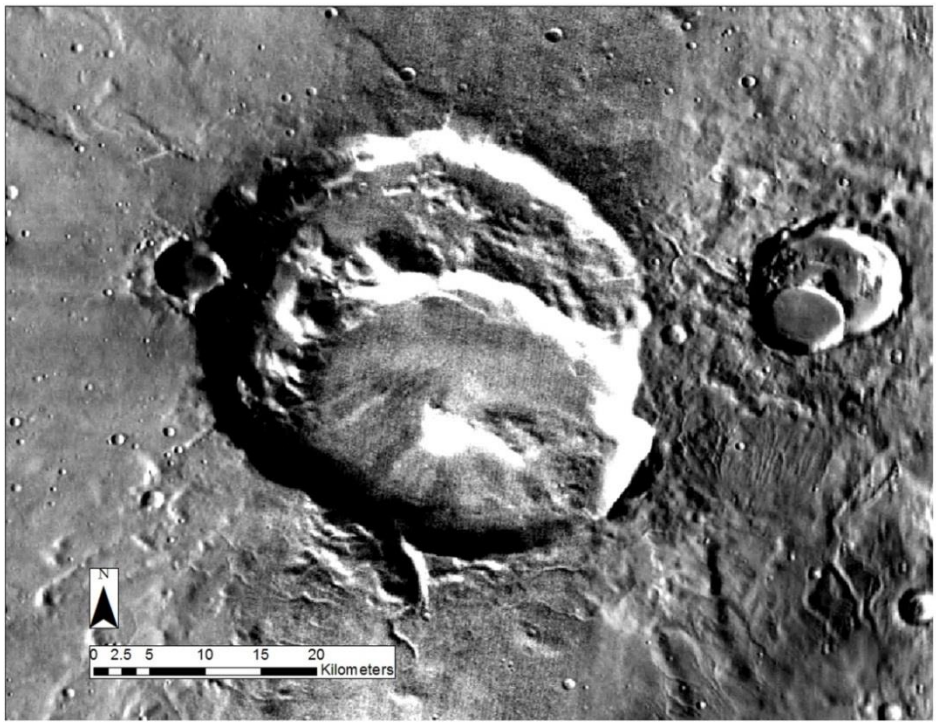

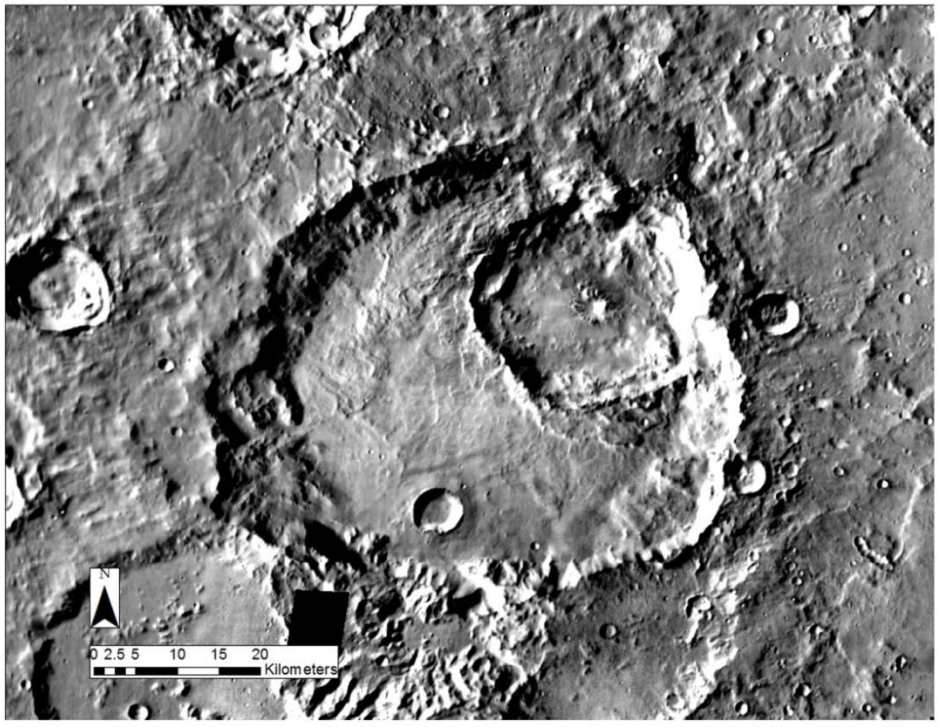

chaotic terrain, blocks separating from the rim, and very uneven walls. It appears that the only characteristics Siloe Patera and Crater F share are a secondary crater fully contained within a primary crater.

The classification map and stretched color map were used to generate a geologic map from their results. The classification map was divided into three types of materials: (1) dust; (2) rock; (3) fill-in. The walls of Crater A and Crater B and the spire unsurprisingly showed up as rock in the classification map, stretched color map, and THEMIS Night IR. The majority of the floor of Crater B indicated an abundance of rock uncharacteristic of impact craters, which typically have floors covered in sediment fill. The majority of the surrounding area of Siloe Patera was classified as dust and only a small portion inside Crater A and Carter B was identified as fill-in. Using the classification and stretched color maps, a geologic map was rendered in ArcGIS based on nine different features. The walls of Crater A, Crater B, parts of the bench and much of the floor of Crater B were defined as solid rock with the spire in the middle of Crater B identified as a possible volcanic feature. Five domes, labeled as post-volcanic domes, rest on the bench of Crater A as well as a region of dust to the far right of the bench. Two units of sediment fill-in were identified and divided by what appeared to be two major episodes of deposition. The yellow unit likely formed during an early period of deposition that allowed it to consolidate where the green unit appears to have been the last depositional event of Siloe Patera's history as it fills in low areas. Flows are displayed as light green and appear to have formed during different periods due to degradation, appearance and the length of each flow.

If Siloe Patera is a volcano, its features should be explained by volcanic processes and stages of caldera development. Smith and Bailey (1968), and Acecolla (2006), provide a framework for to describing the different features of Siloe Patera according to their stages of a Resurgent-Caldron Cycle and Caldera Collapse (Figures 13 and 14) with stages of the former model reported using Roman numerals (e.g. “Stage III”) while stages of the latter are reported using Arabic numerals (e.g. ”Stage 3”).

First, doming and sagging in the area would form due to rising magma that would also induce the production of ring fractures (Stage I; Stage 1). Ash flows and lava flows would then cover the area and the potential to erase signs of ring fractures (Stage II). Figures 10A and 10B show the varying length and appearance of lava flows in the Kilauea caldera. The flow features seen to the north, southeast, and southwest of Siloe Patera could be the result of similar lava flows. Collapse of Crater A would then be followed by another stage of ring faulting from resurgence of the magma chamber (Stage III, IV, and V; Stage 2, 3, and 4). The possible ring faults highlighted in Figures 29 and 30 could be the result of resurgence on the floor of Crater A, prior to formation of Crater B. Resurgence would continue and fractures would become more prominent, magma could rise from the cracks of the ring faults and may have resulted in development of the proposed volcanic domes, along the bench in Siloe Patera (Stage V and VI). Shortly after these domes formed, ring faults would form and became the edge of Crater B in its future collapsed (Stage III; Stage 2). The cycle would then started over with Crater B and the spire on the floor of Crater B could be resurgence from the magma chamber (Stage IV). It appears that this was the last stage for Crater B before

the magma chamber moved to the south where the sag feature is located. The history of Siloe Patera proposed here is based on our current understanding of the geology of the region and will be adjusted as more data becomes available.

CHAPTER 6

By utilizing 1.) topographic profile comparisons to known calderas and impact craters; 2.) 3D analyses of regions of interest circum Siloe Patera and the surrounding terrain; 3.) d/D comparisons to fresh and eroded Martian impact sites; and 4.) classification of thermal, visual, and topographic data that aid in the generation of a photogeologic map, suggest that a volcanic origin for Siloe Patera is more plausible than impact origin interpretations

Striking similarities between Siloe Patera and the caldera of Ascraeus Mons points toward a volcanic-based origin. Topographic profiles of Siloe Patera and Ascraeus Mons are almost identical and are much more complex than their impact crater counterparts. Topographic profiles of Siloe Patera show a very inconsistent terrain that is difficult to explain using the double impact crater hypothesis; but is very consistent with a volcanic origin hypothesis. Siloe Patera exceeds the d/D slope angle of Ascraeus Mons by 2 degrees with Crater A, B, C, and F d/D slope angles much lower. Ring faulting on the bench of Crater A is identified as rock with dust cover and not a sedimentary feature, while 3D and high resolution analyses revealed a possible spire of volcanic material with high thermal inertia, as well as steep, arcuate scarps with an angle of 69°. These walls resemble Ascraeus Mons (67°) and not impact craters, which have shallower slope angles (64° - 42°). Volcanic-doming along the boundary of Crater A and Crater B

show up as rock with probable dust or ash deposited around the area. A broad region of subsidence to the south of Siloe Patera could have been the last volcanic event to develop along a southeastward migrating magma chamber. Flow features around Siloe Patera are more likely to be lava flows, than ejecta, due to the isolation and appearance variation of each flow. These flows appear to be dust covered in many areas except at the head of the flow, which shows high thermal inertia. Channels around Siloe Patera do not flow in the typical direction observed in impact crater ejecta blankets, instead flowing into the area of subsidence to the south. Ring faulting, the spire, volcanic-doming, subsidence, and flow features show areas of high thermal inertia in THEMIS Night IR, with the stretch color map and the classification map suggesting hard rock and not sedimentary deposits. Also, the lack of obvious impact crater characteristics; such as ejecta, a central peak, and a raised rim, implies a non-impact origin. These features can easily be explained by volcanic processes; but are more difficult to explain through impact processes.

It is difficult to make an unequivocal conclusion based on the currently available data set. Dust cover presents a challenge with this research and makes mineralogic analysis via spectroscopy virtually impossible. Evidence presented here is based primarily on geomorphic features associated with Siloe Patera as compared to those of Martian impact craters and volcanic calderas. Although the origin of Siloe Pater could be explained by multiple impact craters, multiple caldera collapse events, or a combination of the two, current evidence strongly suggests a volcanic origin and should be considered a Martian supervolcano.

References

Acocella, V., Caldera types: How end-members relate to evolutionary stages of collapse, *Geophysical research letters 33*, no. 18 (2006).

Aline, G., N. Mangol , J. Bibring, Y. Langevin, B. Gondet, F. Poulet, and G. Bonello, Sulfates in Martian layered terrains: the OMEGA/Mars Express view,*Science* 307, no. 5715: 1587-1591, 2005.

Arvidson, R. E. Morphologic classification of Martian craters and some implications,*Icarus* 22, no. 3: 264-271,1974.

Barlow, N. G., J. M.Boyce,F. M. Costard,R. A. Craddock, J. B. Garvin,S. E.Sakimoto,R. O. Kuzmin,D. J.Roddy, and L. A. Soderblom, Standardizing the nomenclature of Martian impact crater ejecta morphologies,*Journal of Geophysical Research*: Planets (1991–2012) 105, no. E11: 26733-26738, 2000.

Bibring, Jean-Pierre, et al. "Global mineralogical and aqueous Mars history derived from OMEGA/Mars Express data." *Science* 312.5772 (2006): 400-404.

Blaschke, T., Object based image analysis for remote sensing,*ISPRS Journal of Photogrammetry and Remote Sensing 65*, no. 1: 2-16, 2010.

Carr, M. H., Mars Global Surveyor observations of Martian fretted terrain,*Journal of Geophysical Research*: Planets (1991–2012) 106, no. E10: 23571-23593, 2001.

Cattermole, P., Planetary Volcanism: A study of volcanic activity in the Solar System,*West* Sussex, England. Ellis Horwood Limited, 1989.

Christensen, P. R., B. M. Jakosky,H. H. Kieffer,M. C. Malin, H. Y. McSween,K. Jr.Nealson, , and G. L. Mehall, The thermal emission imaging system (THEMIS) for the Mars 2001 Odyssey mission,*Space Science Reviews* 110, no. 1-2: 85-130, 2004.

Cole, J. W., D. M. Milner, and K. D. Spinks, Calderas and caldera structures: a review,*Earth-Science Reviews* 69, no. 1: 1-26, 2005.

Crumpler, L. S., J. W.Head, and J. C. Aubele, Calderas on Mars: Characteristics, structure, and associated flank deformation,*Geological Society*, London, Special Publications 110, no. 1: 307-348, 1996.

Dohm, J. M., N. G. Barlow,R. C.Anderson, J.Williams, H. Miyamoto,J. C.Ferris, and R. G.Strom, Possible ancient giant basin and related water enrichment in the Arabia Terra province, Mars,*Icarus* 190, no. 1: 74-92, 2007.

Drăguţ, L., E.Clemens, and S. Thomas, Local variance for multi-scale analysis in geomorphometry, *Geomorphology* 130, no. 3: 162-172, 2011.

Fergason, R. L., and P. R. Christensen, Formation and erosion of layered materials: Geologic and dust cycle history of eastern Arabia Terra, Mars,*Journal of Geophysical Research*: Planets (1991–2012) 113, no. E12, 2008.

Frankel, C., Volcanoes of the Solar System, New York, NY. Cambridge University Press,

Gangale T. Geologic Time Scales of the Earth, Moon, and Mars.<http://pweb.jps.net/~tgangale/mars/mst/GeologicTimeScales.htm> (Accessed 30 September 3013), 2007.

Garvin, J. B., and J. J.Frawley.,Geometric properties of Martian impact craters: Preliminary results from the Mars Orbiter Laser Altimeter,*Geophysical Research Letters* 25, no. 24: 4405-4408, 1998.

Grant, J. A., and P. H. Schultz, Degradation of selected terrestrial and Martian impact craters, *Journal of Geophysical Research*: Planets (1991–2012) 98, no. E6: 11025-11042, 1993.

Greeley, R., Planetary Landscapes, Second edition. New York, NY. Chapman & Hall, 1994

Greeley, R., and P. D. Spudis, Volcanism on Mar,*Reviews of Geophysics* 19, no. 1: 13-41, 1981.

Halevy, I., M.T. Zuber, and D. P. Schrag. A sulfur dioxide climate feedback on early Mars,*Science* 318, no. 5858: 1903-1907, 2007.

Hynek, B. M., R. J. Phillips, and R. E. Arvidson, Explosive volcanism in the Tharsis region: Global evidence in the Martian geologic record,*Journal of Geophysical Research*: Planets (1991–2012) 108.E9, 2003.

Irwin, R. P., T. R. Watters,A. D. Howard, and J. R.Zimbelman, Sedimentary resurfacing and fretted terrain development along the crustal dichotomy boundary, Aeolis Mensae, Mars,*Journal of Geophysical Research*: Planets (1991–2012) 109.E9, 2004.

Kerber, L., J. W. Head,J.Madeleine,F.Forget, and L.Wilson, The dispersal of pyroclasts from ancient explosive volcanoes on Mars: Implications for the friable layered deposits,*Icarus* 219, no. 1: 358-381, 2012.

Malin, M. C., and K. S. Edgett, Mars global surveyor Mars orbiter camera: Interplanetary cruise through primary mission,*Journal of Geophysical Research*: Planets (1991–2012) 106, no. E10: 23429-23570, 2001.

Martínez-Alonso, S., B. M. Jakosky,M. T.Mellon, and N. E. Putzig, A volcanic interpretation of Gusev Crater surface materials from thermophysical, spectral, and morphological evidence,*Journal of Geophysical Research*: Planets (1991–2012) 110, no. E1, 2005.

Meaden, G. J., andJ. M. Kapetsky, Geographical information systems and remote sensing in inland fisheries and aquaculture,*FAO Fisheries Technical Paper*. No. 318. Rome, FAO. 262p, 1991.

McEwen, A. S., E. M. Eliason, J.W.Bergstrom, N. T. Bridges,C. J. Hansen,A. W.Delamere, and J. A. Grant, Mars reconnaissance orbiter's high resolution imaging science experiment (HiRISE),*Journal of Geophysical Research*: Planets (1991–2012) 112, no. E5, 2007.

McGill, G. E., Crustal history of north central Arabia Terra, Mars,*Journal of Geophysical Research*: Planets (1991–2012) 105, no. E3: 6945-6959, 2000.

Milam, K. A., K. R. Stockstill,J. E. Moersch,H. Y. McSween,L. L.Tornabene,A. Ghosh,M. B. Wyatt, and P. R. Christensen, THEMIS characterization of the MER Gusev crater landing site,*Journal of Geophysical Research*: Planets (1991–2012) 108, no. E12,2003.

Miller, C. F., and D. A. Wark, Supervolcanoes and their explosive supereruptions,Elements 4, no. 1: 11-15, 2008.

Omran, M., A. Salman, and A. P. Engelbrecht, Image classification using particle swarm optimization,*Proceedings of the 4th Asia-Pacific conference on simulated evolution and learning*. Vol. 2002, 2002.

Osinski, G. R. and E.Pierazzo, Impact Cratering: Processes and Products, in Impact Cratering: Processes and Products, (eds G. R. Osinski and E. Pierazzo), John Wiley & Sons, Ltd, Chichester, UK. doi: 10.1002/9781118447307.ch1, 2012.

Pike, Richard J. Formation of complex impact craters: Evidence from Mars and other planets,*Icarus* 43.1: 1-19, 1980.

Robbins, S. J., and B. M.Hynek, A new global database of Mars impact craters≥ 1 km: 1. Database creation, properties, and parameters,*Journal of Geophysical Research*: Planets (1991–2012) 117, no. E5, 2012.

Robock, A., and J.Mao, Winter warming from large volcanic eruptions,*Geophysical Research Letters* 19, no. 24: 2405-2408, 1992.

Scott, D. H., and M. H. Carr, Geologic map of Mars, Map 1-1083, *US Geological Survey*, Reston, Va., 1978.

Scott, D. H., and K. L. Tanaka, Geologic map of the western equatorial region of Mars,*Geological Survey* (US), 1986.

Smith, D. E., M. T.Zuber, H. V.Frey, J. B. Garvin,J. W. Head, D. O. Muhleman, and G. H.Pettengill, Mars Orbiter Laser Altimeter: Experiment summary after the first year of global mapping of Mars,*Journal of Geophysical Research*: Planets (1991–2012) 106, no. E10: 23689-23722, 2001.

Smith, E. I., Comparison of the crater morphology-size relationship for Mars, Moon, and Mercury,*Icarus* 28, no. 4: 543-550, 1976.

Smith, Robert L., and R. A. Bailey.Resurgentcauldrons, *Geological Society of America* Memoirs 116: 613-662, 1968.

Tanaka, K. L. The stratigraphy of Mars,*Journal of Geophysical Research*: Solid Earth (1978–2012) 91, no. B13: E139-E158, 1986.

Tian, F., M. W. Claire, J. D. Haqq-Misra,M.Smith, D. C. Crisp,D.Catling, K. Zahnle, and J. F.Kasting, Photochemical and climate consequences of sulfur outgassing on early Mars,*Earth and Planetary Science Letters* 295, no. 3: 412-418, 2010.

Vincent, R. K., Fundamentals of Geological and Environmental Remote Sensing, Upper Saddle River, NJ. Prentice Hall, 1997.